Advances in MRI to Probe the Functional and Structural Network of the Macaque Brain

by

Mark Haig Khachaturian

B.S.E. Nuclear Engineering & Engineering Physics (2001)
University of Michigan, Ann Arbor, MI

S.M. Nuclear Engineering (2003)
Massachusetts Institute of Technology, Cambridge, MA

Submitted to the Department of Nuclear Science and Engineering in partial fulfillment of the requirements for the degree of

DOCTOR OF PHILOSOPHY IN NUCLEAR SCIENCE AND ENGINEERING
AT THE
MASSACHUSETTS INSTITUTE OF TECHNOLOGY

September 2007

Signature of Author: _____
Department of Nuclear Science and Engineering
July 30th, 2007

Certified by: _____
Bruce Rosen
Professor of Radiology, Harvard
Thesis Committee Chairman

Certified by: _____
Wim Vanduffel, Thesis Supervisor
Assistant Professor in Radiology, Harvard

Certified by: _____
David Tuch, Thesis Supervisor
Head of Medical Physics, Novartis Pharma AG

Certified by: _____
Alan Jasanoff, Thesis Reader
Professor of Nuclear Science and Engineering, MIT

Certified by: _____
David Cory, Thesis Reader
Professor of Nuclear Science and Engineering, MIT

Accepted by: _____
Jeffery Coderre, Thesis Reader
Chairman of the Department of the Committee of Graduate Students

Advances in MRI to Probe the Functional and Structural Network of the Macaque Brain

by
Mark Haig Khachaturian

Submitted to the Department of Nuclear Science and Engineering on July 30th, 2007
in partial fulfillment of the requirements for the degree of
Doctor of Philosophy in Nuclear Science and Engineering
at the
Massachusetts Institute of Technology

Abstract

Diffusion MRI and fMRI have provided neuroscientists with non-invasive tools to probe the functional and structural network of the brain. Diffusion MRI is a neuroimaging technique capable of measuring the diffusion of water in neural tissue. It can reveal histological architecture irresolvable by conventional magnetic resonance imaging methods and has emerged as a powerful tool to investigate a wide range of neuropathologies. fMRI is a neuroimaging technique sensitive to hemodynamics which is indirectly linked to neural activity. Despite the applications of diffusion MRI and fMRI in basic and clinical neuroscience, the underlying biophysical mechanisms of cerebral diffusion and the hemodynamic response remain largely unknown. Also, these neurotechnqiues suffer from low SNR compared to conventional MRI. The challenges associated with the acquisition and interpretation of diffusion MRI and fMRI limit the application of these powerful non-invasive neuroimaging tools to study the functional and structural network of the brain.

The purpose of this thesis is three fold; (1) improve the acquisition and reconstruction of the diffusion MRI and fMRI signals and (2) develop an MR-compatible cortical cooling system to reversibly deactivate cerebral glucose metabolism, and (3) apply the cortical cooling system to investigate the effect of cerebral glucose metabolism on cerebral diffusion and the hemodynamic response. First, I describe a novel phased array monkey coil capable of improving the resolution of diffusion MRI (4 fold increase) and fMRI (2 fold increase) in monkeys. Secondly, I present a novel reconstruction method to resolve complex white matter architecture which boosts the sampling efficiency of the diffusion MRI acquisition by 274-377%. Thirdly, I present a MR-compatible cortical cooling system capable of reversibly deactivating cerebral metabolism in monkeys. The cortical cooling system has been applied to study the effect of cerebral glucose metabolism on the cerebral diffusion of water. I use MR temperature maps to quantify the region and degree of deactivation (accuracy of ±1 °C *in vivo*). Then, I show that reversible deactivation of cerebral glucose metabolism affects the magnitude of cerebral diffusion (12-20%) but not the anisotropy. Finally, I apply the cortical cooling system to study the effect of reversibly deactivating cerebral glucose metabolism in V1 and its effect on the hemodynamic response in the visual system. Reversible deactivation of V1 decreased the hemodynamic response in visually driven regions upstream and downstream from V1. Compensatory effects were observed in V1 in both hemispheres and ipsilateral TEO with in 2 minutes of deactivation. Here I have described the tools to probe the functional and structural network of the macaque brain.

Thesis Supervisor: Wim Vanduffel
Title: Assistant Professor of Radiology, Harvard

Thesis Supervisor: David Tuch
Title: Head of Medical Physics, Novartis Pharma AG

Acknowledgements & Support

First and foremost, I would like to thank Professor Wim Vanduffel and Dr. David Tuch for funding my research. I deeply appreciate the five years they spent training me in neuroimaging and neuroscience. I would also like to thank Professor Bruce Rosen for providing me with the opportunity to work at the Athinoula A. Martinos Center and Professors Alan Jasanoff, David Cory, and Jeffery Coderre for providing me with valuable input on my research. Furthermore, I would like to thank Professors Sidney Yip and Sow-Hsin Chen for their advice on topics ranging from particle physics to career planning. My nights in the laboratory would have been less productive without Helen Deng, John Arsenault, and Leeland Ekstrom. In addition, I received invaluable support from Larry Wald, Andreas Potthast, Ken Kwong, Thomas Benner, Leonardo Angelone, David Salat, Kevin Teich, Simon Sigalovsky, Nathanael Hevelone, Timothy Reese, and Josh Synder. I could not have completed this thesis without the love and emotional support of my father, Arek Khachaturian, my mother, JoAnn Diane Khachaturian, my sister, Lee Khachaturian and my girlfriend, Bettina Romberg.

My PhD has been one of the most exciting and enjoyable times in my life. It is in no small part due to the brothers of the ΛΦ chapter of AΔΦ. The six years I spent living in the chapter has provided me with memories which I will treasure for the rest of my life. I would like to extend special thanks to Brothers Warren Ruder, Manish Gaudi, Patrick Hereford, David Van Aken, Nelson Sanz, Adan Gutierrez, Stan Bileshi, Matthew Wallace, Mike Szulczewski, and Brothers Eric Sparks and Martin Lee of the Penninsular Chapter of AΔΦ.

I would like to thank the following grants and institutions for supporting my research: IUAP 5/04, EF/05/014, FWO G151.04, HFSPO RGY0014/2002-C, GSKE, NINDS NS46532, NINDS MH67529, NCRR RR14075, NIBIB EB005149, NCI CA09502, NCI 5T32CA09502, the Athinoula A. Martinos Foundation, the MIND Institute, the National Alliance for Medical Image Computing (U54 EB05149) which is funded by the NIH Roadmap for Medical Research, the Human Frontiers Science Program (RGY 14/2002), and Deutsche Forschungsgemeinschaft (GRK320 and KO 1560/6-2).

Table of Contents

List of Figures

List of Tables

§1 Introduction

1.1 Introduction

One of the goals of neuroimaging research is to measure the various aspects of neural function and quantify how they depend on external stimuli and how they change during neurodegenerative diseases. To this end, diffusion MRI and fMRI have provided neuroscientists with non-invasive tools to probe the functional and structural network of the brain.

Diffusion MRI is a neuroimaging technique capable of measuring the diffusion of water in neural tissue. Diffusion MRI is sensitive to the diffusion of water on length scales ranging from 10 nm to 100 μm, and over time scales ranging from 1 ms to 1 s. Given that the average size of neurons in the brain is about 10 μm, diffusion MRI provides a sensitive probe of tissue microstructure. It can reveal aspects of histological architecture irresolvable by conventional magnetic resonance imaging methods.

Diffusion MRI has emerged as a powerful tool to investigate neuropathologies such as stroke, Parkinson's disease, HIV dementia, schizophrenia, cocaine addiction, normal aging, Alzheimer's disease, chronic alcoholism, multiple sclerosis, epilepsy, and ALS. More recently, diffusion MRI has also been proposed as a promising technique to identify anatomical white-matter fiber tracts *in vivo* and measure neural activity. Despite the applications of diffusion MRI in basic and clinical neuroscience, the underlying biophysical mechanisms that affect cerebral diffusion contrast remain largely unknown.

Since its development in the early nineties, functional magnetic resonance imaging (fMRI) has been very useful in helping neuroscientists map the brain (i.e. localizing brain regions involved in the processing of particular functions). fMRI is sensitive to hemodynamics which is correlated to some degree with neural activity. fMRI studies have explored the hemodynamics associated with sensory processing, motor, and cognitive skills and have focused mainly on 'mapping' questions. Combining fMRI with other techniques (reversible deactivation, electrophysiology, etc.) could provide more information on the underlying mechanisms of the hemodynamic response and could be used to measure the interactions between functional regions.

Also, owing to the low SNR of the diffusion MRI and fMRI signals, it is difficult to acquire images in a time efficient manner. The challenges associated with the acquisition and

interpretation of diffusion MRI and fMRI limit the application of these powerful non-invasive neuroimaging tools to study the functional and structure network of the brain.

1.2 Purpose

The goal of this thesis is to develop tools to further the application of diffusion MRI and fMRI to study the functional and structural network in the macaque brain. I accomplish this goal by (1) improving the acquisition and reconstruction of the diffusion MRI and fMRI signals and (2) developing an MR-compatible cortical cooling system to reversibly deactivate cerebral glucose metabolism, and (3) applying the cortical cooling system to investigate the effect of cerebral glucose metabolism on cerebral diffusion and the hemodynamic response. The following five Specific Aims were proposed:

Specific Aim 1: Develop a 4-channel 3T phased array monkey coil

PURPOSE: To develop a 4-channel 3T phased array coil for diffusion MRI and fMRI studies in awake and anesthetized monkeys.

HYPOTHESIS: Test the hypothesis that the 4 channel 3T phased array coil will have higher SNR and less EPI distortions across the brain compared to a single channel transmit/receive coil.

RESULTS: The SNR of the 4-channel 3T coil was always greater than or equal to the SNR of a single transmit/receive coil. The phased array coil improved the resolution of fMRI and studies by a factor of 2 and the resolution of diffusion MRI studies by a factor of 4.

ORIGINAL CONTRIBUTIONS: I describe a novel phased array monkey coil capable of improving the resolution of fMRI and diffusion MRI while accommodating variations in monkey head size.

FUTURE APPLICATIONS: To apply the general methodology to develop phased array coils with more than four coil elements and at higher magnetic fields.

Specific Aim 2: Develop and optimize the multi-wavevector fusion of DTI and QBI data to resolve white matter architecture

PURPOSE: To develop a general framework to improve the sensitivity and angular contrast of the orientation distribution function (ODF) calculated from high angular resolution diffusion imaging (HARDI) methods, specifically Q-ball imaging (QBI).

HYPOTHESIS: Test the hypothesis that the multi-wavevector fusion (MWF) of DTI and QBI improves the stability and angular contrast of the ODF reconstruction using numerical simulation and human results.

RESULTS: The MWF of DTI and QBI resulted in a sampling efficiency boost of 274-377% while resolving more white matter architecture than QBI alone.

ORIGINAL CONTRIBUTIONS: I present a novel reconstruction method to resolve white matter architecture which boosts the sampling efficiency of current diffusion MRI reconstruction methods.

FUTURE APPLICATIONS: To apply the MWF of DTI and QBI to study the changes in white matter architecture in neurodegenerative diseases.

Specific Aim 3: Develop and validate cortical cooling system using MR temperature maps

PURPOSE: To develop a MR-compatible cortical cooling system to reduce the cerebral temperature below the metabolic cut-off temperature (20 °C). To acquire MR temperature maps using proton resonance frequency shift thermometry (PRFST) and measure the accuracy and precision of the temperature maps against fiber optic thermocouples in *ex vivo* tissue.

HYPOTHESIS: Test the hypothesis that the cortical cooling system can deactivate cortical tissue and that PRFST is accurate to within ± 1 °C of the fiber optic thermocouples.

RESULTS: An MR-compatible cooling probe was developed. Cortical tissue can be deactivated (T < 20 °C) in one minute. PRFST was accurate to within ± 0.6 °C of the fiber optic thermocouples. The precision of the *in vivo* PRFST measurements is ± 1 °C at 2.0 mm isotropic resolution.

ORIGINAL CONTRIBUTIONS: I present a MR-compatible cortical cooling system capable of reversibly deactivating cerebral glucose metabolism in monkeys. In addition, I use MR temperature maps, with an accuracy of ±1 °C *in vivo*, to quantify the region and degree of deactivation. Quantification of the deactivation region has not been possible with any other reversible deactivation method.

FUTURE APPLICATIONS: To apply the MR-compatible cortical cooling system to the study of the effect of cerebral glucose metabolism on perfusion MRI, MRI spectroscopy, and other imaging modalities (i.e. FDG-PET).

Specific Aim 4: Measure cerebral diffusion properties during the reversible deactivation of cerebral glucose metabolism

PURPOSE: To apply the MR-compatible cooling system to quantify the effect of cerebral glucose metabolism on the apparent diffusion coefficient (ADC) and

fractional anisotropy (FA) as measured by diffusion tensor imaging (DTI).

HYPOTHESIS: Test the hypothesis that the ADC and FA are affected by cerebral glucose metabolism.

RESULTS: Reversible deactivation of cerebral glucose metabolism resulted in ADC changes (12-20%) in regions where the temperature did not change. No changes in FA were observed. The *in vivo* ADC as a function of temperature was also measured.

ORIGINAL CONTRIBUTIONS: I apply the MR-compatible cortical cooling system to study the underlying mechanisms of diffusion MRI and find that the ADC has a metabolic component.

FUTURE APPLICATIONS: To study what aspects of cerebral glucose metabolism could account for the decrease in the ADC.

Specific Aim 5: Measure the hemodynamic response in the visual system during reversible deactivation of V1

PURPOSE: To apply the cortical cooling system to reversibly deactivate V1 and measure its affect on the hemodynamic response of the visual system.

HYPOTHESIS: Reversible deactivation of V1 modulates the hemodynamic response in visual structures.

RESULTS: Reversible deactivation of V1 decreased the hemodynamic response in regions upstream and downstream from V1. Compensatory effects were observed in both hemispheres within 2 minutes of deactivation. Positive and negative correlations between metabolic activity in V1 and the MRI signal in visually and non-visually driven structures were also observed.

ORIGINAL CONTRIBUTIONS: I apply the MR-compatible cortical cooling system to study the effect of cerebral glucose metabolism in V1 on the hemodynamic response in visual network.

FUTURE APPLICATIONS: To perform reversible deactivation fMRI experiments to explore the perception of the visual field and the plasticity of the macaque brain. Also, FDG-PET experiments can be performed to determine if visually and non-visually driven structures require input from V1 to remain metabolically active.

1.3 Outline

This thesis is divided into 7 sections (§2-8). §2, describes the development and construction of a 4-channel 3T phased array coil used for acquiring diffusion MRI and fMRI

(Specific Aim 1). §3 reviews the theory behind the diffusion MRI reconstruction methods. Then, I present a novel diffusion MRI reconstruction method for resolving white matter architecture with diffusion MRI in a more sampling efficient and accurate manner (Specific Aim 2) than previous methods (§4).

Again, I sought to quantify the effect of cerebral glucose metabolism on cerebral diffusion and the hemodynamic response (Specific Aims 3-5). §5 describes the development of a MR-compatible cortical cooling system capable of reversibly deactivating cerebral glucose metabolism (Specific Aim 3). §6 describes the application of the cortical cooling system to study the effect of cerebral glucose metabolism on cerebral diffusion (Specific Aim 4). In §7, the cortical cooling system was applied to study the effect of reversibly deactivating cerebral glucose metabolism in V1 on the hemodynamic response in the visual system (Specific Aim 5).

The thesis concludes with §8, which summarizes the major contributions of my research and future research projects.

§2 Phased Array Coil Development

2.1 Introduction

Awake monkey fMRI combined with conventional neuroscience techniques (e.g. electrophysiology, lesion studies, reversible deactivation, optical imaging, etc.) has the potential to study the hemodynamic response to external stimuli and the interactions between regions of the functional network[1-5]. The majority of monkey MRI experiments are performed with single coils[1,4,5]. Though previous monkey studies have provided valuable information, single coil full brain fMRI and diffusion MRI studies suffer from severe EPI distortions at resolutions higher than 1.25 mm isotropic for fMRI[1,4,5] and 1.5 mm isotropic for diffusion MRI[6].

By constructing phased array coils for monkey MRI studies, substantial gains in SNR and image quality could be achieved using parallel imaging[7-10]. *The major challenge associated with constructing phased array coils for monkeys is the variation in head size.* Phased array technology is based on placing the multiple receive channels as close to the head as possible[11]. Therefore, the natural variation in monkey head size makes rigid coils impractical. A more minor concern is the space constraints associated with awake monkey fMRI experiments. The monkeys is confined in a chair with its headpost secured to the outside of the chair[4]. This leaves very little room for RF coils and renders birdcage designs useless.

Here, we describe a 4-channel phased array coil capable of improving the resolution and image quality of full brain awake monkey fMRI and diffusion MRI experiments. The novel aspect of the phased array coil is that can adapt to different rhesus monkey head sizes (ages 4-8). The methodology described in this section can be used in the development of phased array coils for other primates and small animals with more than four coil elements and at higher magnetic fields.

2.2 Background

The most popular fast image acquisition scheme used in diffusion MRI and fMRI studies is called echo planar imaging (EPI). EPI suffers from susceptibility distortions at the boundary between regions with differing magnetic susceptibilities. The distortions can be so severe that registration with anatomical MRI images is not possible leaving the results difficult to interpret.

It is necessary to increase the resolution of EPI in order to further neuroscience applications. Also, improving the resolution may provide new applications of MRI.

The technique of parallel imaging emerged in the late 1990's as a means to decrease the distortions in EPI imaging [9,10]. The theory of parallel imaging allows one to reduce number of lines sampled in k-space, thus reducing the accumulation of phase errors due to susceptibility distortions. Parallel imaging accomplishes this by using the coil sensitivity functions of multiple radio-frequency (RF) receive coils (termed phased array). Parallel imaging is capable of producing relatively distortion free EPI images without increasing the scan time and with little loss in SNR. Parallel imaging allows neuroscientists and clinicians alike to achieve higher resolution and make use of the advances in MR hardware.

Diffusion MRI and fMRI studies on monkeys can provide valuable information unattainable in humans. However, little effort has been put towards developing a robust full brain phased array coil capable of parallel imaging for awake and anesthetized monkey studies. Therefore, diffusion MRI and fMRI studies on monkeys have been limited in resolution by EPI distortions and SNR.

2.3 Materials and Methods

2.3.1 10 cm Transmit/Receive Coil

Most full brain awake monkey fMRI experiments have been performed with a single transmit/receive coil[3-5,12]. A single transmit receive coil has the advantage of being easy to setup and is not affected by variations in size of monkeys heads. In order to quantify the benefits of the 4-channel phased array receive coil, we designed a 10 cm transmit/receive coil.

A 10 cm transmit/receive coil was made from flexible circuit board material (Dupont Pyralux, Durham, NC) and glued (Gougeon Corp. - G5 Adhesive Hardener and Resin Epoxy, Bay City, MI) to a thermoplastic base. The coil was formed in the shape of a 'saddle' to improve the uniformity of the field compared to a circular coil while not affecting the vision of the monkey. The conductor width was 4 mm. The coil had seven capacitors on it and one variable capacitor (Voltronics, Denville, NJ). The coil plugged into a single preamplifier (Advanced Receiver, Burlington, CT). The orientation of the transmit coil (both for the single coil and phased array) is shown in Figure 2-1a,b. The physical shape of the single transmit/receive coil and transmit-only coil was the same.

2.3.2 10 cm Transmit-Only Coil

It would be ideal to use the body transmit coil of the MRI scanner in conjunction with all phased array coils because of its uniform magnetic field over the object. However, the duration and magnitude of RF pulses necessary to reach high resolution (< 1.0 mm isotropic) in animal experiments can induce spiking in the preamplifiers. However, with a custom build 10 cm transmit-only coil, the field of the transmitter is not large enough to reach the preamplifiers. Thus, functional and diffusion MRI experiments are only limited in resolution by the coil properties and not other hardware considerations.

The transmit-only coil was constructed in the same manner as the 10 cm transmit/receive coil. However, a detuning circuit was added so the transmit coil did not interfere with the phased array receive coil during image acquisition. A orientation of the transmit coil relative to the phased array coil is shown along with a schematic of its circuitry in Figure 2-1.

2.3.3 4-Channel Receive Coil

A model of a monkey's head was made from T1 anatomical images using 3D stereolithagraphy (Medical Modeling, Golden, CO). The monkey model is shown in Figure 2-1a,b. A monkey helmet was made from fiberglass cloth (Bondo, Atlanta, GA) and shaped to the monkey model. Four layers of fiberglass cloth were glued together using epoxy to give the monkey helmet a combination of strength and flexibility. The four receive coils were made from flexible circuit board material (Dupont Pyralux, Durham, NC) and glued to the monkey helmet (Gougeon Corp. - G5 Adhesive Hardener and Resin Epoxy, Bay City, MI). A standard capacitive bridge match and PIN diode (MA4P4002B-402; Macom, Lowell, MA) trap was used to detune the receive coils[13]. Two coils were overlapped on the left side of the helmet and two coils were overlapped on the right side. The coupling, S_{12}, between the overlapping coils was checked (< -20 dB) before gluing the coil to the monkey helmet. The coupling between second nearest neighbor coils was minimized using preamplifier decoupling (see next section). Figure 2-1a,b shows a picture of the phased array coil from the sagital and horizontal views on the monkey model and Figure 2-1c shows a schematic of the phased array coil circuitry.

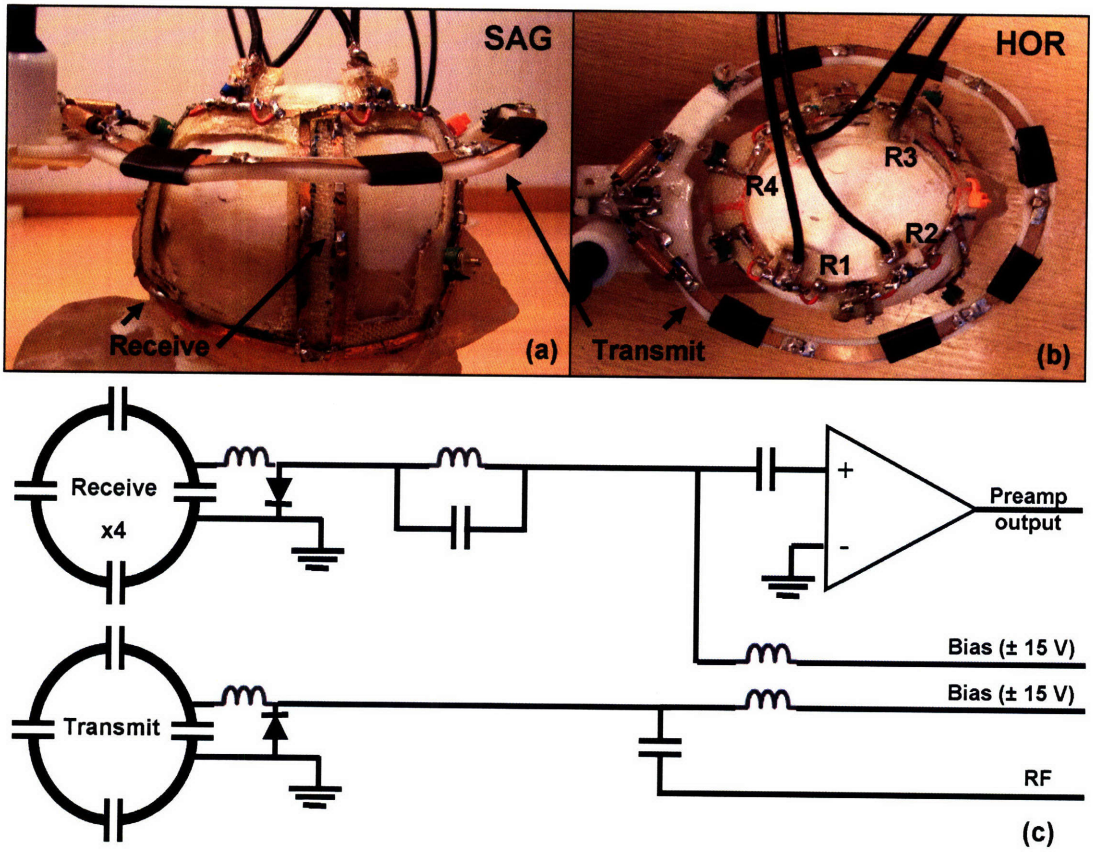

Figure 2-1. (a) Sagital and (b) horization orientations of the 4-channel phased array receive coil (R1 – R4) and 10 cm transmit coil on the monkey model. (c) Circuit schematic of the transmit and receive coils.

2.3.4 Preamplifiers

A preamplifier board was constructed and made portable to accommodate the different stereotactic apparatus and monkey chairs used in awake and anesthetized MRI experiments. The preamplifier board consists of eight preamplifiers (Siemens Medical Solutions, Erlangen, Germany), and four bias lines (± 30 V) to tune and detune the transmit and receive coils. Preamplifier decoupling was employed using a cable trap with semi rigid coax (Suhner UT-070 type) to suppress any residual coil coupling from next nearest neighbor interactions[11,14]. The preamplifier circuitry is shown in Figure 2-1c.

2.3.5 Animal Preparation

MRI data were acquired from three juvenile male rhesus monkeys (macaca mulattas, M1, 5.5 kg, ID #3704, M2, 4.9 kg, ID #0404, M3, 5.7 kg, ID #4505). The data were acquired on a Siemens Trio 3T MRI scanner located at the Athinoula A. Martinos Center for Biomedical

Imaging, Massachusetts General Hospital (Charlestown, Massachusetts). All procedures conformed to Massachusetts General Hospital, Massachusetts Institute of Technology, and the National Institutes of Health guidelines for the care and use of laboratory animals (Subcommittee on Research Animal Care protocol #2003N000338).

M1 was placed into a magnet compatible stereotactic apparatus (Kopf Instruments, Tujunga, California) for an anaesthetized experiment to compare the performance of the single coil to the phased array coil. Anaesthesia was maintained using ketamine and xylazine (induction 10 and 0.5 mg/kg, i.m., maintenance with ketamine only). Local anesthetic (lidocaine cream) was applied to the ends of the ear bars and ophthalmic ointment was applied to the eyelids to minimize discomfort induced by the stereotactic apparatus. A heating pad was placed beneath the monkey to keep it warm during the scan session.

The monkeys were placed in a monkey chair (Crist Instruments, Washington, DC) during awake experiments. All monkeys were implanted with a headpost (Crist Instruments, Washington, DC) that was secured to the monkey chair using two M5 peek plastic screws. Also a rail system was used to slide the monkey chair in the magnet to minimize motion. The following sequences were used to quantify the behavior of the phased array coil and single coil.

2.3.6 Data Acquisition

2.3.6.1 g-factor Maps

Proton density gradient-echo images were acquired in order to calculate g-factor maps of the phased array coil for horizontal, coronal, and sagital slices as described in Wiggins et al [11]. Raw k-space data was obtained with TR/TE/flip = 200 ms/4.14 ms/20°, 1.5 mm single slice, 128 x 112, and 100 x 87 mm FOV.

2.3.6.2 Coil sensitivity maps

Proton density gradient-echo images were also acquired in order to perform a non-uniform signal normalization on the T1 anatomical images to improve gray and white matter contrast and aid in image registration (50 slices, TR/TE/flip = 1190 ms/3.72 ms/8°, 1.0 mm isotropic, 96 x 96 matrix size).

2.3.6.3 fMRI

Functional single shot echo planar images (EPI) were acquired at two different resolutions (1.25 mm, 1.0 mm isotropic) to compare the SNR and image quality of the single coil to the phased array coil. The SNR properties of the coils was compared on a voxel-wise basis using the following equation for SNR;

$$SNR = \frac{S}{\sigma_{background}} \quad (2.1)$$

where S is the signal in a voxel and $\sigma_{background}$ is the standard deviation of the background.

fMRI - 1.25 mm

Forty horizontal slices were acquired using TE/TR = 26/2980 ms, 72 x 64 matrix, 90° flip angle at 1.25 mm isotropic resolution. The same sequence was used for the both the single coil and phase array coil.

fMRI - 1.0 mm BOLD

Fifty horizontal slices were acquired using TE/TR = 26/3290 ms (phased array coil), 26/5000 ms (single coil), 96 x 84 matrix, 90° flip angle at 1.0 mm isotropic resolution. The phased array coil had a lower TR because parallel imaging[9,10,15] was employed, specifically generalized auto-calibrating partially parallel acquisitions (GRAPPA, R = 2)[15].

fMRI - 1.0 mm MION

Microcrystalline iron oxide nanoparticles, (MION)[26,27], enhanced fMRI data was collected on all monkeys. Fifty horizontal slices were acquired using TE/TR = 24/2700 ms, 96 x 84 matrix, 90° flip angle at 1.0 mm isotropic resolution using the phased array coil. The Siemens AC88 gradient insert was used (BW = 1305 Hz/voxel) to decrease the TR. GRAPPA with an acceleration factor of two was employed[15].

2.3.6.4 Diffusion MRI

The diffusion preparation used a twice-refocused spin echo [16]. Fifty-seven horizontal slices were taken of M1 at 0.9 mm (0 mm skip). The in-plane resolution was 0.9 x 0.9 mm, with

a matrix size of 96 x 96. The sequence parameters were TE/TR = 93/10100 ms, b = 700 s mm^{-2}. The diffusion gradient sampling scheme consisted of n = 60 directions which were obtained using the electrostatic shell method [17]. Ten images with no diffusion weighting were also obtained for a total of 70 acquisitions. The total acquisition time was 11 min 48 sec. The diffusion images from five acquisitions were averaged and reconstructed using the diffusion tensor model[18].

2.3.7 T1 Anatomical Images

T1 anatomical images were acquired with an MPRAGE sequence[19] with TR/TI/TE = 1910/1100/3.06 ms, $\alpha = 8^{o}$, 0.65 mm isotropic resolution, total acquisition time: 6 min 35 sec. The functional EPI, proton density and GRE images were registered to the T1 images for comparison between the single and phase array coils.

2.3.8 Image registration and visualization

Images were registered using the flirt command (rigid registration, 6 degrees of freedom) in the FSL toolbox (http://www.fmrib.ox.ac.uk). All visualization post-processing was performed using custom software written in Matlab (version 6.5.1.199709 (R13) Service Pack 1). DTI reconstructions were visualized with custom software written in C++ and VTK (version 4.2) (http://public.kitware.com/VTK). The tensors were visualized as color-coded rectangloids.

2.4 Results

2.4.1 Coil Properties

The coupling between the coils was measured using the S_{12} measurement on a network analyzer. The two sets of overlapping coils had < -20 dB decoupling between them. Next nearest neighbor coupling was < -10 dB. In addition, the preamp decoupling added -20 dB of decoupling. Therefore, all coils had < -30 dB of decoupling between them ensuring each coil behaved as a single element in the tuned state. PIN diode detuning achieved > 35 dB isolation between the tuned and detuned states. The unloaded/loaded Q-factors of the individual coils was Q_{R1} = 117/123, Q_{R2} = 154/145, Q_{R3} = 129/137, Q_{R4} = 123/145.

2.4.2 SNR

The SNR for all images was calculated using Eq. (2.1). The SNR in four slices of M1 for the single and phased array coils is shown in Figure 2-2. The identical sequence was used for both coils and both images are on the same scale. Note the SNR benefit of the phased array coil is along the edge of the brain closest to the coils. In the center of the brain, the SNR is nearly the same for both coils.

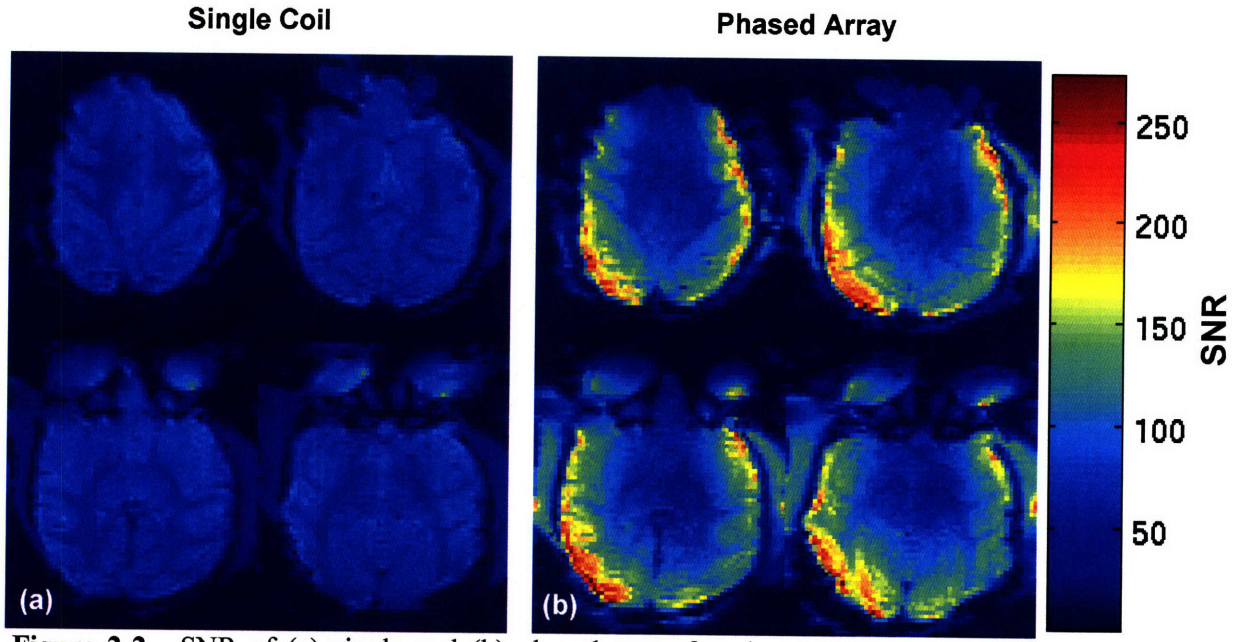

Figure 2-2. SNR of (a) single and (b) phased array functional EPI at 1.25 mm isotropic resolution with identical sequence parameters. Both images are on the same scale.

Figure 2-3 presents the SNR profile along the different axes of the brain. Table 2-1 presents the relative SNR of the phased array coil to the single coil in regions relevant to fMRI studies.

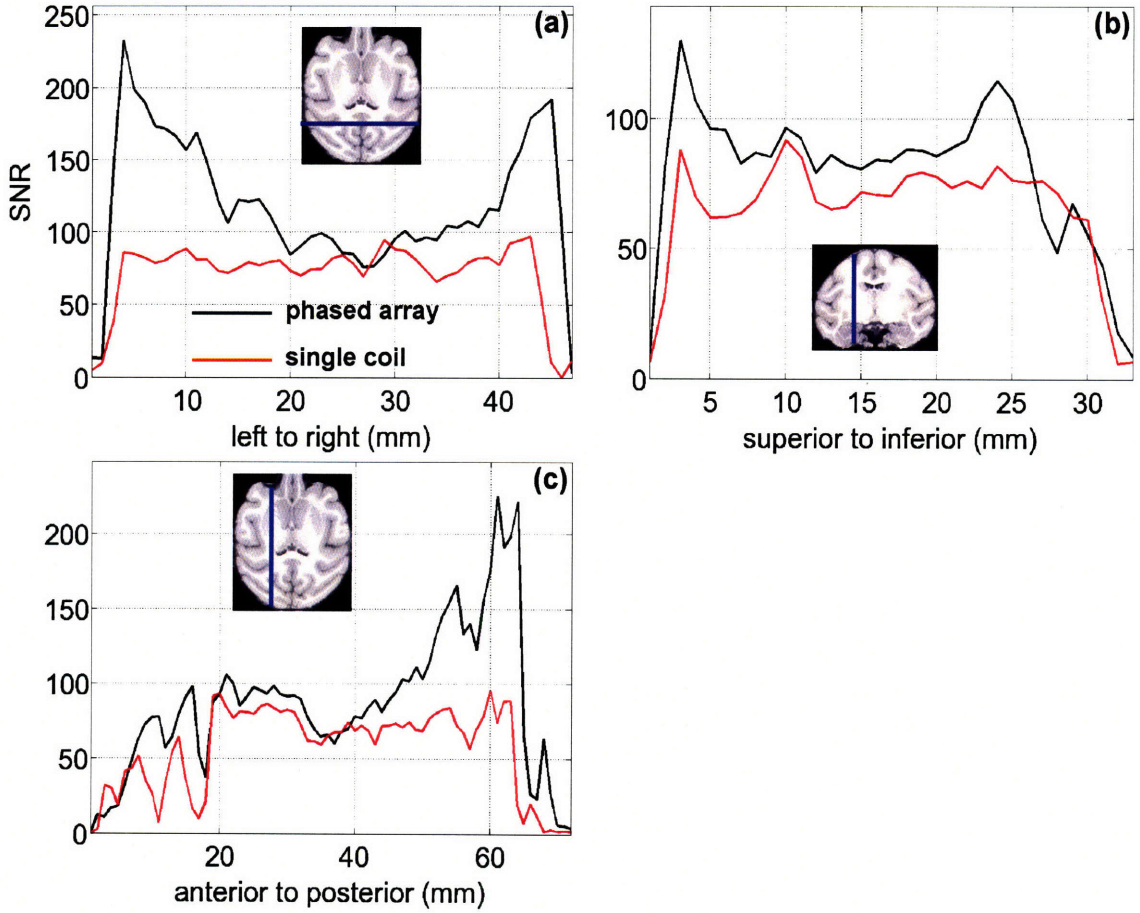

Figure 2-3. SNR of (a) left-right, (b) anterior-posterior, and (c) superior-inferior projections of the phased array and single coil for functional EPI at 1.25 mm isotropic resolution. The SNR of the phased array coil is always greater than or equal to that of the single coil.

Table 2-1. Relative SNR (± SEM) in the phased array coil relative to the single coil in primary visual cortex (V1), the frontal eye fields (FEF), and the lateral geniculate nucleus (LGN) in the left and right hemispheres (LH, RH). Values in parenthesis represent significant p-values from a two sample t-test comparing the SNR in the single and phased array coils (α = 0.01).

Region	SNR_{PA}/SNR_{SC}	
	LH	RH
V1	2.5 ± 0.07 ($6e^{-19}$)	1.8 ± 0.07 ($3e^{-10}$)
FEF	1.5 ± 0.04 ($3e^{-5}$)	2.2 ± 0.1 ($2e^{-5}$)
LGN	0.99 ± 0.06	1.1 ± 0.08

2.4.3 g-factor

An important property of a phased array coil is its g-factor map. The inverse g-factor map quantifies how much SNR is lost in the brain during a parallel acquisition compared to an

image with no acceleration, R = 1. The parallel imaging capabilities of a 4 channel coil limit the acceleration factor to two, (i.e. R = 2)[9]. Figure 2-4 presents the inverse g-factor maps for the phased array coil for an acceleration factor of two in the different phase encode directions. Less than 15% of the SNR is lost during an acceleration factor of two in 85% of the brain. The maximum g-factor of 1.35 (Figure 2-4a) occurs in the horizontal slice with left-right phase encoding.

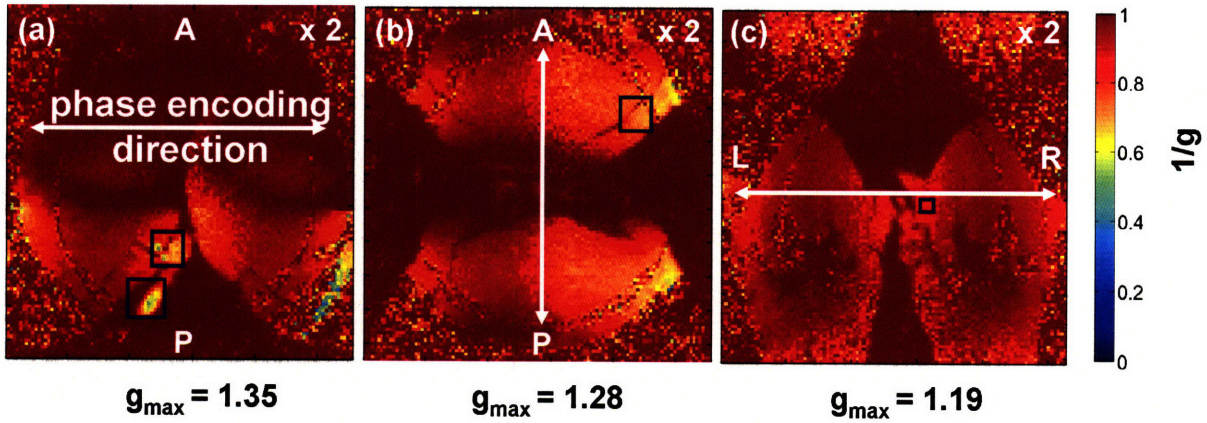

Figure 2-4. 1/g-factor maps for the (a) left-right horizontal, (b) anterior-posterior horizontal, and (c) left-right coronal phase encode directions for two-fold GRAPPA acceleration, R = 2. The blue boxes indicate where the maximum g-factor in the slice is located. In 85% of the brain, the SNR decrease is less than 15% for two-fold GRAPPA acceleration. The average SNR decrease in the brain is ~ 50% for R = 3 (data not shown).

2.4.4 fMRI

Functional EPI (BOLD) was acquired at 1.0 mm isotropic resolution. The TR of the phased array coil was much shorter (3290 ms) compared to that of the single coil (5000 ms) because parallel imaging (GRAPPA, R = 2) was employed. Figure 2-5 presents EPI at 1.0 mm isotropic for the single and phased array coil. The benefit of parallel imaging with regards to EPI distortions is apparent around the edge of the brain along with the benefit in SNR.

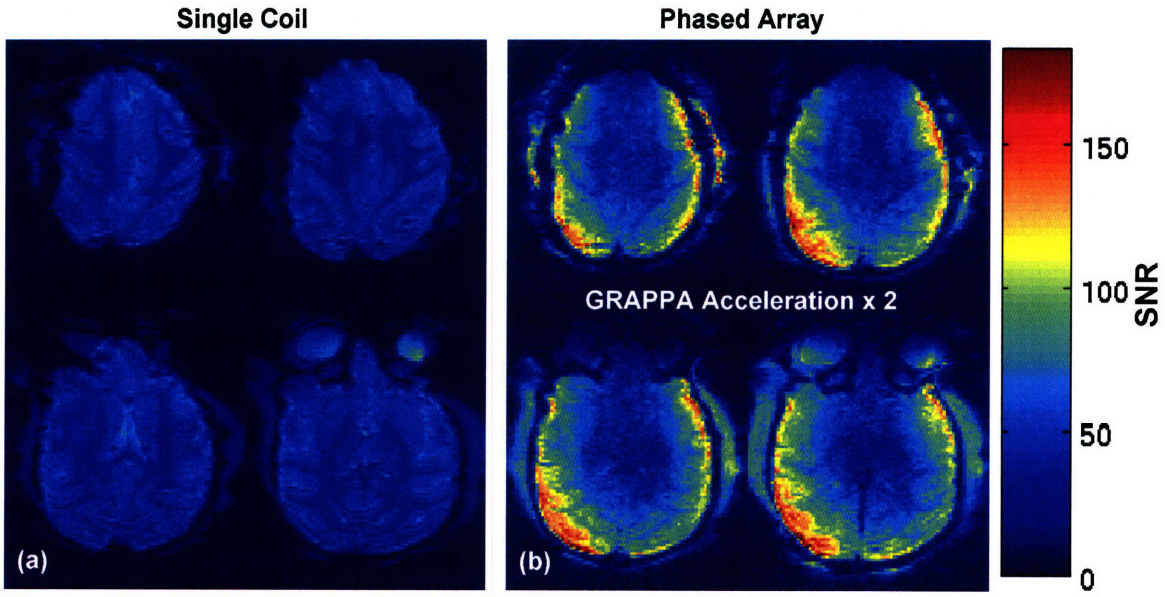

Figure 2-5. SNR of (a) single and (b) phased array functional EPI at 1 mm isotropic resolution. The phased array coil images where taken with a GRAPPA acceleration factor of 2. Note, the improvement in the image quality on the around the edge of the brain in the phased array image. Both images are on the same scale.

Figure 2-6 presents functional EPI (MION) of M1, M2, and M3. The images were acquired with the AC88 gradient insert (Siemens, Erlangen, Germany). The SNR profiles in the brain are relatively consistent between the monkeys despite the natural variation in head size. M1 has the largest head and thus the signal in the middle of the brain is the lowest compared to M2 and M3.

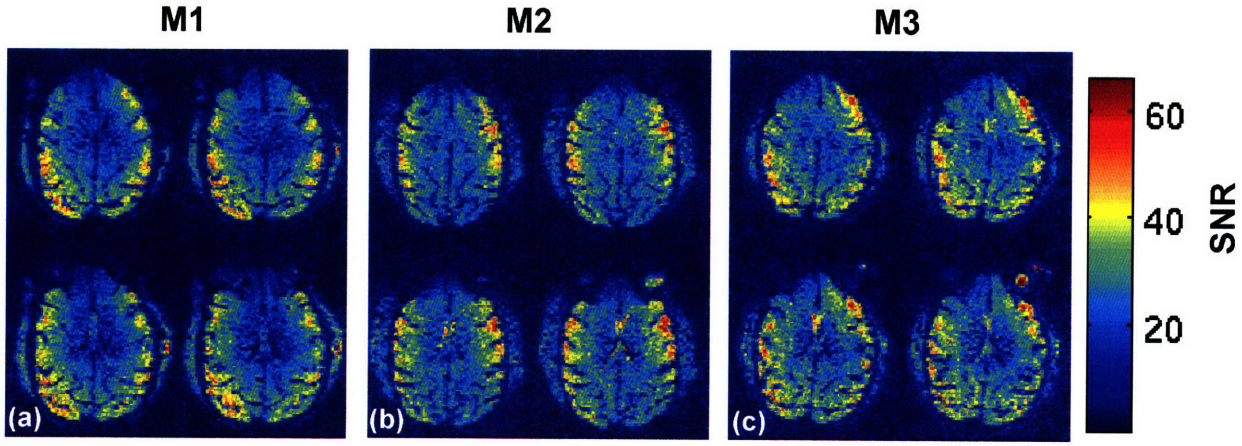

Figure 2-6. Functional EPI (with MION) acquired with the phased array coil for (a) M1, (b) M2, and (c) M3 at 1.0 mm isotropic resolution, TE/TR = 24/2700 ms. M1 has a larger brain than M2 and M3 resulting in lower SNR in the middle of the brain. However the SNR in all monkeys is sufficient (~ 25) to measure the MION response in visually driven cortex.

2.4.5 Diffusion MRI

Figure 2-7 depicts the DTI reconstruction of a 0.9 mm isotropic acquisition in M1. The tensor map is overlayed on a T1 with a rigid registration algorithm. ADC and FA maps calculated from the tensors are presented in panels b and c. The phased array coil resolves the ADC and FA throughout the brain.

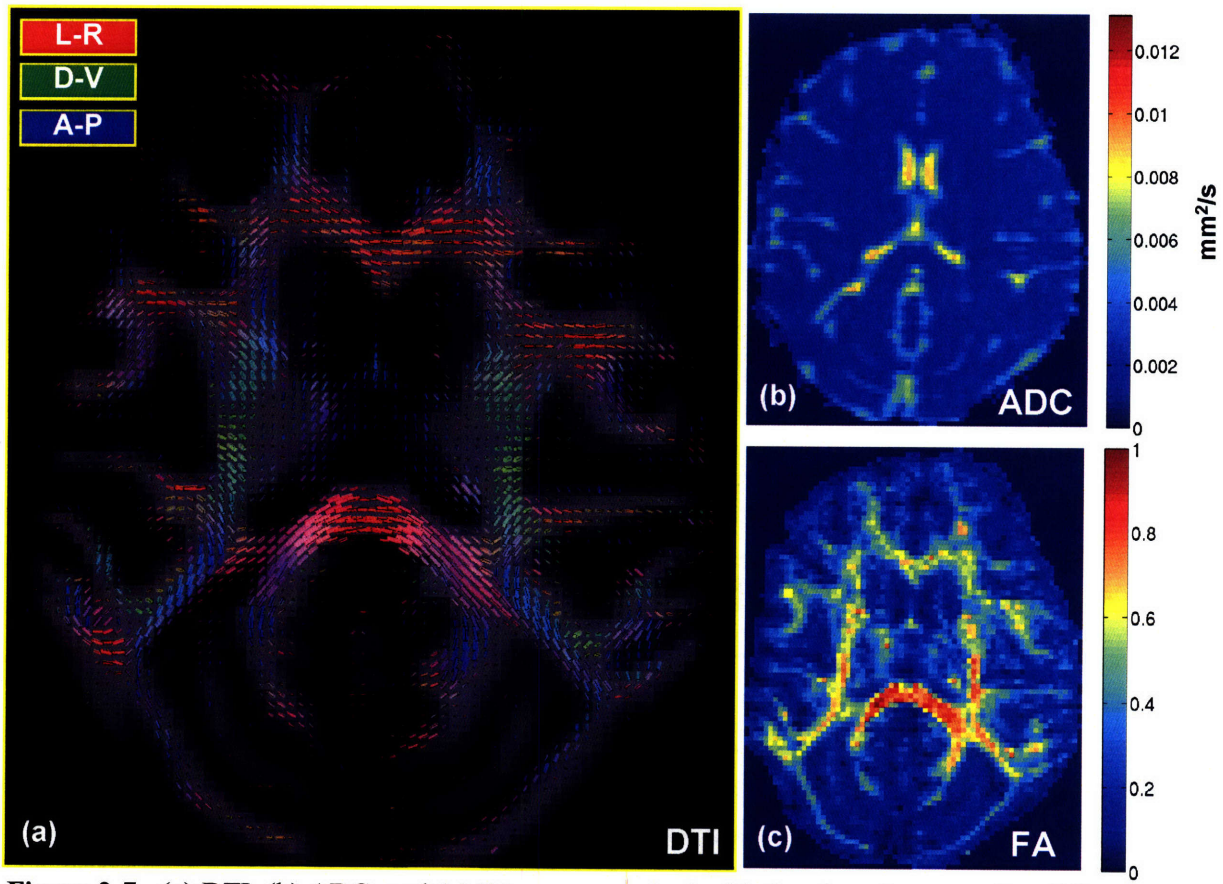

Figure 2-7. (a) DTI, (b) ADC, and (c) FA maps acquired with the phased array coil at 0.9 mm isotropic resolution in M1. The phased array coil resolves the ADC and FA throughout the brain.

2.5 Discussion

The SNR benefit of the phased array coil compared to the single coil throughout visual cortex, make it ideal for awake monkey fMRI studies (Figure 2-2, Figure 2-3, and Table 2-1). In addition the benefit of using the phased array coil with parallel imaging improves the resolution of awake monkey fMRI experiments at 3T by a factor of 2 (Figure 2-5 and Figure 2-7) and diffusion MRI experiments by a factor of 4 (Figure 2-7). Parallel imaging also improves the

time efficiency of fMRI studies by 35% due to a lower TR. The preservation of the anatomical integrity of the diffusion images implies registration with T1 images is possible with a rigid registration algorithm. Thus, tensor maps can be visualized on a T1 image making tractography more accurate. During parallel imaging, an SNR loss of less than 15% is present over 85% of the brain with a maximum loss of 26%, GRAPPA = 2 (Figure 2-4). The coil does not interfere with the eyes of the monkey, or with the headpost of the monkey because all of the coils are on the side of the head (Figure 2-1). This allows eye tracking to be performed during fMRI experiments. In addition, the flexibility of the fiberglass helmet allows the coil to easily adapt to different monkeys (Figure 2-6).

Though four coils were used in this phased array, future phased arrays with more coils could be constructed using the same techniques described in this section. The general methodology of making a monkey helmet from a mold based on T1 anatomical images, can be applied to primates and other animals. More importantly, the practical application of the coil should be taken into account when developing a phased array coil. For example, for fMRI studies only interested in retinotopy, it may be more suitable to use more channels regardless of the coils performance in deep cortical structures[20]. Also, for T1 anatomical studies of rhesus monkeys, a headpost is not necessary. This would allow one to put coils on top of the brain making the phased array coil superior to the single coil throughout the brain.

2.6 Conclusion

A 3 Tesla 4-channel phased array coil was developed to improve the resolution and image quality of awake monkey fMRI and diffusion MRI experiments. The phased array coil had a SNR benefit of ~ 2 on surface cortex and was equal to that of a single coil in the center of the brain. The phased array coil allowed parallel imaging to be employed reducing EPI distortions. It improved the resolution of fMRI studies by a factor of 2 while increasing the efficiency by a factor of 35% in time. When applied to diffusion MRI studies, the phased array coil improved the resolution of diffusion MRI images by a factor of 4 compared to single coil studies.

§3 Diffusion MRI Reconstruction Methods

3.1 The Diffusion MRI Signal is Proportional to the Average Self Propagator

All practical diffusion imaging is performed with some variation on the pulsed gradient spin echo (PGSE)[21]. Recently, with larger magnetic fields and larger gradients, adjustments have to be made to the PGSE to account for Eddy currents[16]. The amplitude of the PGSE signal is directly related to the average self propagator $\bar{P}_s(\mathbf{R},\tau)$. The average propagator is the Fourier Transform of the amplitude of the diffusion signal, $E(\mathbf{q},\tau)$.

$$E(\mathbf{q},\tau)=\int \bar{P}_s(\mathbf{R},\tau)e^{2\pi i\mathbf{q}.\mathbf{R}}d^3R \tag{3.1}$$

with

$$\mathbf{q}\equiv\frac{1}{2\pi}\gamma\mathbf{g}\delta \tag{3.2}$$

where $\mathbf{g}$ is the gradient vector and δ is the duration of the gradient. Both variables are defined by the user in the pulse sequence. The average propagator represents the probability of a particle to travel a distance R in the direction $\mathbf{u}=\mathbf{R}/|\mathbf{R}|$ in a time τ, given that it started at the origin [21,22]. In reconstructing the data, there are three major schemes to extract information on the cerebral diffusion of water. They are; diffusion tensor imaging (DTI)[18], q-space imaging (QSI)[21], and high angular resolution diffusion imaging (HARDI) [6,21,23-32].

3.2 Reconstruction Methods

3.2.1 Diffusion Tensor Imaging (DTI)

Diffusion imaging methods to date have chiefly been based on analytical models of the underlying diffusion process. For example, diffusion tensor imaging assumes homogeneous Gaussian diffusion within each voxel, an assumption which is clearly invalid for the vast majority of the brain at presently achievable voxel resolutions [33]. The assumption of the Gaussianity of the diffusion signal is very limiting and suppresses multimodal angular information in the diffusion signal. However, DTI has high SNR as compared with other diffusion imaging methods.

A number of different parameters are calculated from the diffusion tensor. First, the diffusion tensor has six parameters, termed diffusion coefficients. Recall that a 2nd rank symmetric tensor can be represented as shown below

$$\mathbf{D}=\begin{bmatrix} D_{xx} & D_{xy} & D_{xz} \\ D_{xy} & D_{yy} & D_{yz} \\ D_{xz} & D_{yz} & D_{zz} \end{bmatrix} \tag{3.3}$$

Assuming that diffusion is Gaussian in nature and described by a tensor, the average propagator, $\bar{P}_s(\mathbf{R},\tau)$, is proportional to

$$\bar{P}_s(\mathbf{R},\tau) \propto e^{\frac{-\mathbf{R}^T\mathbf{D}^{-1}\mathbf{R}}{2\tau}} \tag{3.4}$$

Using the relationship between the average propagator and the diffusion signal in Eq. (3.1), the diffusion signal then becomes

$$E(b,\mathbf{u})=E_o e^{-b\mathbf{u}^T\mathbf{D}\mathbf{u}} \tag{3.5}$$

with

$$b=(2\pi)^2\,\mathbf{q}^T\mathbf{q}\,\tau \tag{3.6}$$

The diffusion tensor components are determined by applying the gradients in different directions (at least six) and at least one image where no gradient is applied in order to determine E_o in Eq. (3.5). Figure 3-1 shows diffusion tensors calculated in the monkey brain and visualized with solid rectangloids. The colors of the rectangloids indicate the direction of the principle eigen-vector.

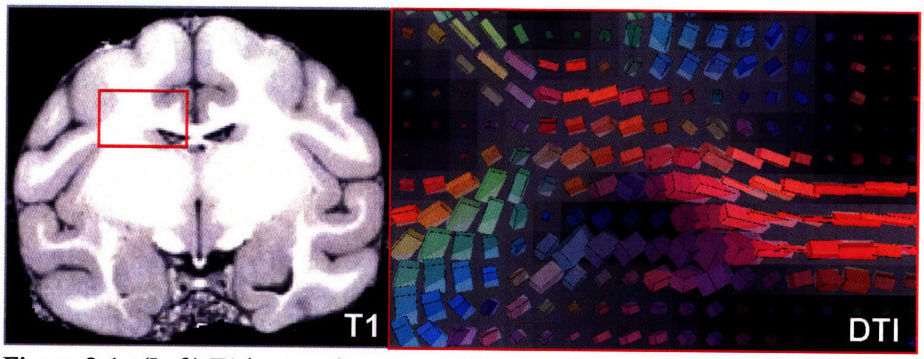

Figure 3-1. (Left) T1 image of monkey. (Right) Diffusion tensors calculated from a 0.9 mm isotropic DTI acquisition. The colors of the rectangloids indicates their direction; red = left-right, blue = anterior-posterior, green = superior-inferior.

Besides, the diffusion coefficients, two other parameters of interest are calculated from the tensor. The apparent diffusion coefficient (ADC) is a scalar measure of the amount of diffusion in a voxel. The ADC is calculated using the three eigenvalues $(\lambda_1,\lambda_2,\lambda_3)$ of the diffusion tensor.

$$\mathrm{ADC} = \frac{1}{3}(\lambda_1+\lambda_2+\lambda_3) \tag{3.7}$$

The second parameter calculated from the diffusion tensor is the fractional anisotropy (FA). The fractional anisotropy is a scalar measure of the symmetry of the tensor. An FA value of one indicates a highly anisotropic diffusion tensor whereas a value of zero represents isotropic diffusion. The FA is calculated from the equation below.

$$\mathrm{FA} = \frac{\sqrt{(\lambda_1-\lambda_2)^2+(\lambda_1-\lambda_3)^2+(\lambda_3-\lambda_2)^2}}{\sqrt{2}\sqrt{\lambda_1^2+\lambda_2^2+\lambda_3^2}} \tag{3.8}$$

The diffusion coefficients, the ADC, and the FA describe the most of the important features of a diffusion tensor. An example of ADC and FA maps is shown in Figure 3-2 in the macaque monkey.

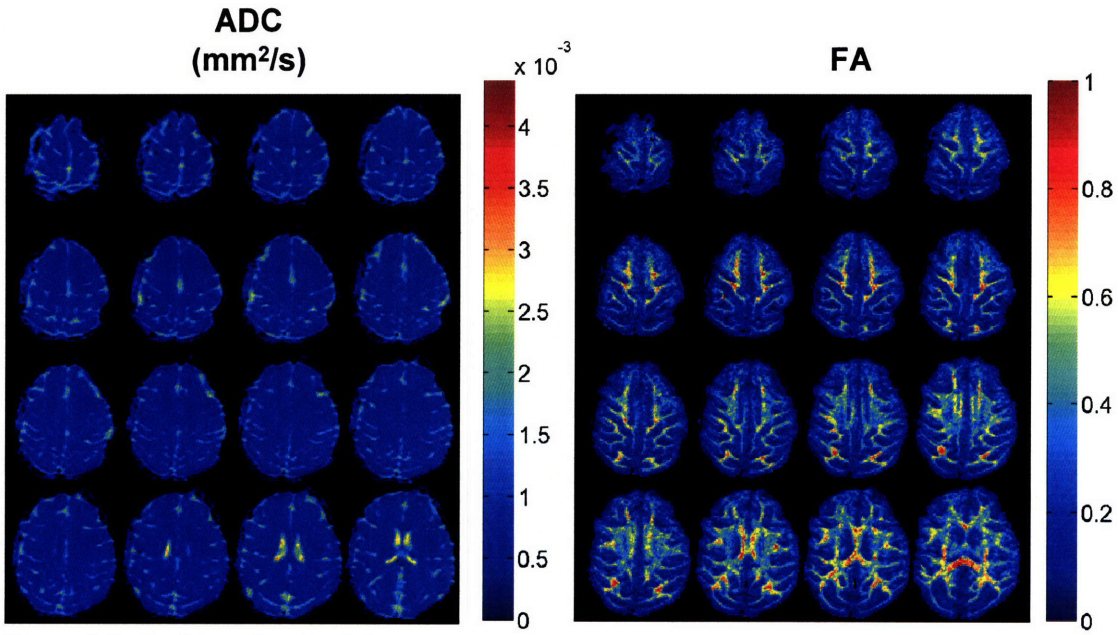

Figure 3-2. (Left) ADC and (Right) FA maps calculated from a DTI acquisition at 0.9 mm isotropic on a monkey. The FA, which is a measure of anisotropy, is highest in white matter.

The two other diffusion reconstruction methods are QSI and HARDI, which don't assume a single mode of diffusion. Both QSI and HARDI calculate the orientation distribution

function. Here we limit our discussion to HARDI methods which are model independent, specifically Q-ball imaging (QBI)[24].

3.2.2 Q-space Imaging (QSI)

Both QSI and QBI calculate the orientation distribution function. The angular distribution function or orientation distribution function (ODF), $\psi(\theta,\varphi)$, of the water molecules, represents the likelihood of water to diffuse in a particular direction, and can provide neuroscientists considerable information about microscopic brain architecture. Mathematically, it is defined as the radial projection of the average propagator onto the unit sphere.

$$\psi(\theta,\varphi)=\int_R \bar{P}_s(\mathbf{R},t)\,dR \qquad (3.9)$$

The ODF contains much more information than the diffusion tensor because it is capable of describing multimodal diffusion. QSI and QBI calculate the ODF using two different methods.

QSI measures the average propagator directly by sampling the diffusion signal on a three dimensional Cartesian lattice. The average propagator is then calculated by taking the 3-D inverse Fourier Transform of Eq. (3.1). The ODF is then calculated from the average propagator using Eq. (3.9). However, QSI suffers from two practical weaknesses. Because the technique requires gradient sampling on a three-dimensional Cartesian lattice, it is time-intensive. Furthermore, QSI requires large pulsed field gradients that may not be available for various types of MR scanners.

3.2.3 Q-ball Imaging (QBI)

To address the concerns of QSI, investigators proposed an approach based on sampling on a spherical shell (or combination of shells) in diffusion wavevector space. The spherical sampling approach is referred to as high angular resolution diffusion imaging (HARDI) [23,32,34]. In theory, the efficiency gain of HARDI would stem from need to sample only on a spherical shell as opposed to the three-dimensional Cartesian volume required by QSI. By selecting a sampling shell of a particular radius the acquisition could also be targeted towards specific length scales of interest. David Tuch has developed a reconstruction scheme for the HARDI data acquisition which is called Q-ball imaging (QBI)[24]. QBI is not as limited by SNR as QSI and scan times of

40 minutes are achievable with QBI. In QBI, the ODF is calculated by applying the Funk-Radon transform to the diffusion signal sampled on a spherical shell[24].

3.2.4 Technical Limitations

Although QSI and QBI are capable of probing tissue architecture and neural connectivity, they suffer from two problems that limit its effectiveness and applicability; (i) low signal to noise/long scan times, and (ii) noise instability of the reconstruction algorithm. The SNR difficulties arise from the high wavevectors that are necessary to resolve the angular peaks in the diffusion signal. These high wave vectors give SNRs ranging from 2 – 10. In addition, the scan time is to long to be used consistently in a clinical setting (> 30 minutes) [35].

§4 Q-ball Imaging Using Multiple Wavevector Fusion[36]

4.1 Introduction

Q-ball imaging (QBI) is a high angular resolution diffusion imaging (HARDI) method which can resolve complex, subvoxel white matter architecture [24,25,37]. Other HARDI methods include persistent angular structure MRI (PASMRI) [32], mixture model decomposition [26,27], generalized DTI [28,29], spherical harmonic transformation [23], spherical harmonic deconvolution [30], and composite hindered and restricted model of diffusion (CHARMED) [31]. Resolving multiple diffusion peaks with QBI and other HARDI techniques requires time-intensive sampling and large diffusion wavevectors. The time-intensive sampling and large wavevectors entail long data acquisition times ($\approx$ 20 minutes) and low signal-to-noise, which limit the feasibility of the method for routine clinical or investigative scans. Improving the sampling efficiency and signal-to-noise of HARDI represents an active area of research in diffusion imaging.

We show here that the sampling efficiency and signal-to-noise of QBI can be increased substantially by fusing the diffusion signal from different diffusion wavevectors. This reconstruction procedure is referred to as multiple wavevector fusion (MWF). In the MWF reconstruction, the low wavevector signal provides high signal-to-noise and the high wavevector data provide the angular contrast-to-noise necessary to resolve multiple diffusion peaks. The MWF method also provides a framework for combining information from diffusion tensor imaging (DTI) [18] and QBI, while retaining overall model independence. More generally, the MWF approach provides a framework for combining information from different diffusion length scales.

Previous work [24,25,37] described combining multiple wavevectors using linear summation. Linear summation offers a number of advantages including retaining the overall linearity of the QBI reconstruction [24], and providing a clear interpretation of the transfer function in terms of the diffusion space projection function [24,37]. It is not clear though that linear summation provides an optimal estimate of the diffusion orientation distribution function (ODF) for a fixed number of samples. The present study sought to test whether nonlinear fusion of diffusion signals acquired at low and high wavevectors could provide a more accurate estimate of the diffusion ODF. The organization of the remainder of this section is as follows. We review the theory of QBI; introduce the MWF fusion algorithm; demonstrate the reconstruction performance of MWF on

numerical simulations; and compare human DTI/QBI data reconstructed using the standard method and with the MWF reconstruction.

4.2 Theory

4.2.1 Q-ball Imaging

QBI reconstructs the diffusion ODF $\psi(\mathbf{u})$ from the diffusion signal by using the Funk-Radon transform [24]. The diffusion ODF describes the probability for a spin to displace in a cylindrical element around the director **u**. The diffusion ODF is defined as the radial projection of the diffusion probability density function (PDF), $\psi(\mathbf{u}) = \frac{1}{Z}\int_0^\infty dr\, P(r\mathbf{u})$ where $P(r\mathbf{u})$ is the PDF and **r** is the relative spin diffusion vector [24]. Investigators have recently validated the QBI reconstruction in a rayon fiber phantom [38] and separately in a phantom constructed from excised rat spin cord [39].

The diffusion ODF measured by QBI is modulated by a zeroth-order Bessel beam [24], which induces spectral broadening of the diffusion peaks. The width of the Bessel beam is defined by the experimental diffusion wavevector $\mathbf{q}=(2\pi)^{-1}\gamma\delta\mathbf{g}$ where γ is the gyromagnetic ratio, δ is the pulsed gradient duration, and **g** is the pulsed gradient vector [21]. Larger wavevectors provide higher angular resolution but lower signal, and vice versa. It would therefore be desirable to combine information from separate ODFs acquired using low and high wavevectors.

4.2.2 Multiple Wavevector Fusion

The objective of the MWF procedure is to obtain a more accurate estimate of the true diffusion ODF by combining ODFs acquired with different diffusion wavevectors. The MWF algorithm we present here consists of the following steps: (1) represent the ODFs in a common linear basis; (2) select the optimal basis coefficients; and (3) reconstruct the fused ODF from the optimal basis coefficients. This approach borrows from the multiscale signal processing framework originally described by Burt and Adelson [40].

We are given two normalized ODF vectors $\boldsymbol{\psi}_l$ and $\boldsymbol{\psi}_h$ which were acquired using low and high diffusion wavevectors, respectively, q_l and q_h. . The ODFs are indexed over the same set of directors so that $\boldsymbol{\psi}$ and $\boldsymbol{\psi}_h = [\, \psi_h(\mathbf{u}_i)]$. We seek to obtain an estimate ψ_f of the true ODF, where f denotes fused. The ODFs are decomposed into a common linear basis $\boldsymbol{\psi}_l = \mathbf{G}\mathbf{w}_l$ and $\boldsymbol{\psi}_h = \mathbf{G}\mathbf{w}_h$,

where **G** is a spherical basis matrix. The spherical basis matrix is constructed from basis functions on the sphere such as spherical harmonics, spherical wavelets, or spherical radial basis functions. The basis coefficients for the low and high wavevector ODFs are computed using the matrix pseudoinverse: $\mathbf{w}_l = \mathbf{G}^+\boldsymbol{\psi}_l$ and $\mathbf{w}_h = \mathbf{G}^+\boldsymbol{\psi}_h$, where $\mathbf{G}^+ = (\mathbf{G}^H\boldsymbol{\Sigma}^{-1}\mathbf{G})^{-1}\mathbf{G}^H\boldsymbol{\Sigma}^{-1}$ is the Moore-Penrose pseudoinverse of **G** and H denotes the conjugate transpose and $\boldsymbol{\Sigma}$ is the noise covariance matrix of the ODF. The basis coefficient vector $\mathbf{w}_f$ for the fused ODF is determined using a selection rule $\mathbf{w}_f = \oplus(\mathbf{w}_l,\mathbf{w}_h)$. Here, we use the choose-max selection rule [40,41], also known as the max modulus rule, $\oplus(\mathbf{w}_l,\mathbf{w}_h) = [\text{maxmod}(w_l^i, w_h^i)]$. The maxmod function

$$\text{maxmod}(a,b) = \begin{cases} a & \text{if } |a| \geq |b| \\ b & \text{otherwise} \end{cases} \tag{4.1}$$

returns the argument with the largest complex modulus. Other possible selection rules include weighted average or window based verification [41]. The fused ODF is then reformed from the fused basis vector, $\boldsymbol{\psi}_f = Z^{-1}\mathbf{G}\mathbf{w}_f$, where Z is a normalization constant to ensure that $\mathbf{1}^T\boldsymbol{\psi}_f = 1$. The general scheme for the MWF procedure is shown in Figure 4-1. The algorithm is also summarized in Table 4-1.

$$\left.\begin{array}{l} \boldsymbol{\psi}_l \xrightarrow{\mathbf{G}^+} \mathbf{w}_l \\ \boldsymbol{\psi}_h \xrightarrow{\mathbf{G}^+} \mathbf{w}_h \end{array}\right\} \xrightarrow{\oplus} \mathbf{w}_f \xrightarrow{\mathbf{G}} \boldsymbol{\psi}_f$$

Figure 4-1. Schematic diagram of MWF fusion algorithm.

Table 4-1. Summary of the MWF algorithm.

Objective: Given 2 ODFs $\boldsymbol{\psi}_l$ and $\boldsymbol{\psi}_h$, compute the fused ODF $\boldsymbol{\psi}_f$
1. Construct spherical basis matrix **G**
2. Calculate basis coefficient vectors for each ODF: $\mathbf{w}_l = \mathbf{G}^+\boldsymbol{\psi}_l$, $\mathbf{w}_h = \mathbf{G}^+\boldsymbol{\psi}_h$
3. Construct fused basis coefficient vector using choose max rule:
$\mathbf{w}_f = [w_f^i] = [\oplus(w_l^i, w_h^i)] = [\text{maxmod}(w_l^i, w_h^i)]$
4. Reconstruct fused ODF: $\boldsymbol{\psi}_f = Z^{-1}\mathbf{G}\mathbf{w}_f$, where Z is a normalization constant.

4.2.3 Spherical Wavelet Basis

The MWF fusion algorithm requires specifying a basis set for the ODF decomposition. For the numerical simulations and experimental data reconstruction, we used the spherical Gabor

wavelet basis [42-44]. The spherical Gabor wavelets are Gaussian modulated sine and cosine waves on the sphere:

$$G(\alpha,k)=\frac{k^2}{\sigma^2}e^{-\frac{k^2\alpha^2}{2\sigma^2}}\left(e^{ik\alpha}-e^{-\sigma^2/2}\right) \tag{4.2}$$

where α is the angular distance between two points on the sphere, σ is the width of the Gaussian kernel, and k is the frequency of the complex exponential. The spherical Gabor wavelets have a number of advantages including local support, the tendency to provide sparse descriptions, and a straightforward implementation [42-44]. The tendency to provide sparse descriptions in this application refers to considering only a neighborhood of points around a given director.

4.2.4 Intravoxel Peak Connectivity Metric (IPCM)

An intravoxel peak connectivity metric (IPCM) was developed that rewards intravoxel peak connectivity to compare the QBI and MWF reconstructions. The connectivity metric, $\mathrm{IPCM}(\mathbf{r})$, at position $\mathbf{r}$ for a ODF, $\psi(\mathbf{r},\mathbf{u}_i)$, where $\mathbf{u}_i$ is the set of directors, rewards ODFs that point to peaks in neighboring voxels. The connectivity metric can be written as

$$\mathrm{IPCM}(\mathbf{r})=\sum_i \psi(\mathbf{r},\mathbf{v}_i)\cdot\psi(\mathbf{r}+\mathbf{v}_i,\mathbf{v}_i) \tag{4.3}$$

Where $\mathbf{v}_i \subset \mathbf{u}_i$ that satisfies the following two conditions:

$$\frac{\mathrm{minmax}(\psi(\mathbf{r},\mathbf{v}_i))}{\sum_i \mathrm{minmax}(\psi(\mathbf{r},\mathbf{u}_i))}>0.0015 \tag{4.4}$$

and

$$\mathrm{Re}\left(\cos^{-1}\left|\mathbf{v}_i\cdot\mathbf{v}_j\right|\right)>20^\circ \quad j\neq i \tag{4.5}$$

The threshold value in Eq. (4.4) was chosen to be greater than the value of an isotropic ODF. An isotropic ODF which is reconstructed at 752 directions would have a value of 1/752 = 0.0013. The numerical simulations suggest QBI recon can clearly resolve peak angular separations of more than 20°. Therefore, 20° was chosen as the threshold for the minimum angular difference between peaks in Eq. (4.5).

4.3 Methods

4.3.1 Numerical Simulation

Numerical simulations were performed to evaluate the reconstruction accuracy of the MWF fusion algorithm using typical parameters from diffusion MRI experiments. The numerical phantom consisted of two Gaussian diffusion processes in slow exchange. The spin echo signal $E(\mathbf{q})$ for this system is given by

$$E(\mathbf{q}) = E(0)\sum_{i=1}^{n} f_i e^{-\mathbf{q}^T \mathbf{D}_i \mathbf{q} \tau} \qquad (4.6)$$

where $n = 2$ is the number of compartments, $\mathbf{q}$ is the diffusion wavevector, $E(0)$ is the spin echo signal with no diffusion weighting, τ is the diffusion time, and f_i and $\mathbf{D}_i$ are respectively the volume fraction and diffusion tensor for compartment i. The b-value is $b = (2\pi)^2 \mathbf{q}^T \mathbf{q} \tau$. For the numerical simulation, the compartment volume fractions were set at $f_1 = 0.55$ and $f_2 = 0.45$ for the first experiment and $f_1 = 0.25$ and $f_2 = 0.75$ for the second experiment. The diffusion tensor eigenvalues were $\{\lambda_1, \lambda_2, \lambda_3\} = \{1.7, 0.3, 0.3\}$ μm^2 ms^{-1} for both compartments. The simulations were performed for four different SNR values; SNR = 4.8, 3.5, 2.5, 1.4. The angle between the principal eigenvector of the diffusion tensors was varied from 0^o to 90^o in intervals of 7.5^o.

Three acquisitions were simulated: DTI (b = 700 s mm^{-2}, 10 T2, 60 DWI), QBI (b = 4000 s mm^{-2}, 0 T2, 252 DWI), and a hemispherical QBI (b = 4000 s mm^{-2}, 0 T2, 126 DWI). The 10 T2 values where simulated using a $\mathbf{q}$ value of zero in Eq. (4.6) to estimate $E(0)$. The QBI reconstruction does not require any information from the T2 weighted images so no T2 images were simulated. For the DTI, the 60 sampling directions were obtained using the electrostatic shell method [17], and for the QBI the sampling directions were obtained from the vertices of a 5-fold regularly tessellated icosahedron projected onto the sphere. Five reconstructions were considered: standard reconstruction of DTI followed by the Funk-Radon Transform (FRT); FRT of QBI; MWF of the DTI and QBI; MWF of the DTI and hemispherical QBI; and linear average of the DTI and QBI. The simulated acquisition parameters and reconstruction procedures are summarized in Table 4-2. The diffusion signal was sampled from a Rician noise distribution with the prescribed SNR values for the DTI and QBI data[37]. The SNR values chosen for the DTI and QBI represented typical experimental values. Reference ODFs representing the ground truth were calculated by applying the FRT to the diffusion signal given by Eq. (4.6) with b = 700 s

mm^{-2}, 252 directions, and no noise. The Funk-Radon transform was implemented with a spherical Gaussian radial basis function width of 8°, and a smoothing kernel width of 1° [24]. For the MWF fusion, the spherical basis set was constructed from spherical Gabor wavelets with k = 8 rad^{-1} and $\sigma = 1$. All ODFs were reconstructed onto the 752 directions obtained from the 5-fold tessellated dodecahedron.

Table 4-2. Acquisitions and reconstructions used in numerical simulations.

Acquisition	Reconstruction	Fusion	Directions	b [s mm^{-2}]
DTI	Tensor, Gaussian PDF, FRT	N/A	10 T2, 60 DWI	700
QBI	FRT	N/A	252 DWI	4000
QBI+DTI	FRT + Tensor, Gaussian PDF, FRT	MWF	252 DWI + 10 T2, 60 DWI	4000+700
Hemi QBI + DTI	FRT + Tensor, Gaussian PDF, FRT	MWF	126 DWI + 10 T2, 60 DWI	4000+700
QBI + DTI	FRT + Tensor, Gaussian PDF, FRT	Linear	252 DWI + 10 T2, 60 DWI	4000+700

The reconstruction accuracy was measured using the Kullback-Leibler (KL) divergence between the reference ODF and the estimated ODF [24]. The KL divergence is an information theoretic measure of the dissimilarity between two probability densities [45]. The KL divergence between the reference ODF ψ_R and the estimated ODF ψ is written as:

$$KL(\psi_R, \psi) = \psi_R (\log \psi_R - \log \psi) \qquad (4.7)$$

The KL divergence was calculated over 110 noise trials for each acquisition/reconstruction method (Table 4-2) and for each angular separation between the Gaussian compartments.

4.3.2 Human Data Acquisition

DTI and QBI data were collected on 7 healthy participants with a 1.5 T Siemens Avanto using an 32-channel phased array coil and a SENSE acceleration factor of R = 2 [9]. The data was collected at the Martinos Center for Biomedical Imaging using a protocol approved by the Massachusetts General Hospital Internal Review Board. The diffusion preparation used a twice-refocused spin echo [16]. All post-processing was performed using custom software written in C++ and Matlab (version 6.5.1.199709 (R13) Service Pack 1). A single participant was scanned with 70 direction DTI and 262 direction QBI protocols. The MWF data was reconstructed using the full acquisition (70 DTI + 262 QBI) and a hemisphere 136 direction QBI acquisition (70 DTI +

136 QBI). The hemisphere acquisition resolved sufficient white matter architecture as measured by the GFA maps. Therefore, the subsequent six participants were scanned with a 123 direction QBI and 70 direction DTI protocols to test the efficiency and reproducibility of the MWF technique across human participants.

DTI Data

Fifty axial oblique slices were taken of the first participant at a slice thickness of 2.2 mm (0 mm skip). The in-plane resolution was 2.2 x 2.2 mm, with a matrix size of 128 x 128. The sequence parameters were TR/TE = 6200/77 ms, b = 700 s mm^{-2}. The diffusion gradient sampling scheme consisted of n = 60 directions which were obtained using the electrostatic shell method [17]. Ten images with no diffusion-weighting were also obtained for a total of 70 acquisitions. The total acquisition time was 7 min 20 sec.

Sixty axial oblique slices were taken of the six subsequent participants at a slice thickness of 2.0 mm (0 mm skip). The in-plane resolution was 2.0 x 2.0 mm, with a matrix size of 128 x 128. The sequence parameters were TR/TE = 6200/77 ms, b = 700 s mm^{-2}. The diffusion gradient sampling scheme consisted of n = 60 directions which were obtained using the electrostatic shell method [17]. Ten images with no diffusion-weighting were also obtained for a total of 70 acquisitions. The total acquisition time was 7 min 20 sec.

QBI Data

Fifteen axial oblique slices were acquired from the first participant with a slice thickness of 2.2 mm (0 mm skip). The 15 slices were a subset of the 50 slices used in the DTI acquisition. The in-plane resolution was 2.2 x 2.2 mm, with a matrix size of 88 x 128. The sequence parameters were TR/TE = 3000/130 ms, b = 3200 s mm^{-2}, q = 691 cm^{-1}, g_{max} = 28 mT m^{-1} and a q-space resolution of $\Delta r = 5.53$ μm according the Rayleigh criterion [24]. The diffusion gradient sampling scheme consisted of 252 directions which were obtained from the vertices of a 5-fold regularly tessellated icosahedron projected onto the sphere. Ten images with no diffusion-weighting were also obtained for a total of 262 acquisitions. The total acquisition time was 10 min 31 sec.

Sixty axial oblique slices were acquired from the subsequent six participants with a slice thickness of 2.2 mm (0 mm skip). The in-plane resolution was 2.2 x 2.2 mm, with a matrix size

of 96 x 128. The sequence parameters were TR/TE = 8900/111 ms, b = 3200 s mm^{-2}, q = 691 cm^{-1}, g_{max} = 28 mT m^{-1} and a q-space resolution of $\Delta r = 5.53\ \mu m$ according the Rayleigh criterion [24]. The diffusion gradient sampling scheme consisted of 123 directions which were obtained from the vertices of a 4-fold regularly tessellated icosahedron projected onto the sphere. One image with no diffusion-weighting was also obtained for a total of 123 acquisitions. The total acquisition time was 18 min 25 sec. All of the data were acquired with the same slice orientation to facilitate cross-participant comparison.

The FRT reconstruction for the QBI data was implemented with a radial basis function width of 8°, and a smoothing kernel width of 6°. The MWF was performed on the 15 corresponding slice from the DTI and QBI scans. The Gabor wavelet basis used k = 8 rad^{-1}, σ = 1.

4.3.3 MWF Fusion

The MWF fusion procedure show in Figure 4-1 was applied to the human data sets. The MWF algorithm was applied to fuse the DTI and the full QBI data, and the DTI and hemisphere QBI. The fusion was applied to the Gaussian ODF provided by DTI and the ODF provided by QBI. The fusion used the spherical Gabor wavelet basis (Eq. (4.2)) with k = 8 rad^{-1}, σ = 1. The raw DTI data was interpolated to the QBI resolution for the six healthy participants using the interpn command (linear 3D interpolation) in Matlab. The IPCM was calculated for all QBI and MWF reconstructions.

4.3.4 Visualization

All visualizations were generated using custom software written in C++ and VTK (version 4.2) (http://public.kitware.com/VTK). The ODFs were visualized as color-coded spherical polar plots. For visualization purposes the QBI and MWF ODFs were min-max normalized and scaled by the generalized fractional anisotropy (GFA) as described in reference [24]. The GFA was visualized as a grayscale background. The transparency of the GFA background was set to 0.6 so the entire ODF could be seen. Interactive visualization of the ODF field required decimating the polygonization of the ODFs. Each ODF was decimated to 15% of its original polygon count from 1500 to 225 polygons. The decimation eliminated vertices but did not move them.

4.4 Results

4.4.1 Numerical Simulation

The numerical simulations showed that reconstruction accuracy of DTI and QBI outperformed the other methods for all angular separations and different SNR values (Figure 4-2a). MWF fusion of DTI and the QBI hemisphere outperformed the remaining methods, including linear fusion of DTI and full QBI despite the fact that the latter had more sampling directions. The accuracy of DTI increased at intermediate angular separations and then decreased. Figure 4-2b shows sample ODFs from individual noise trials for SNR = 2.5. The MWF reconstruction tends to provide sharper diffusion peaks without introducing artificial peaks. The numerical simulations for f_1=0.25 and f_2=0.75 in Figure 4-3a show the reconstruction accuracy of the MWF also outperformed DTI and QBI for all SNR values and angular separations. Figure 4-3b shows sample ODFs from individual noise trials for SNR = 2.5.

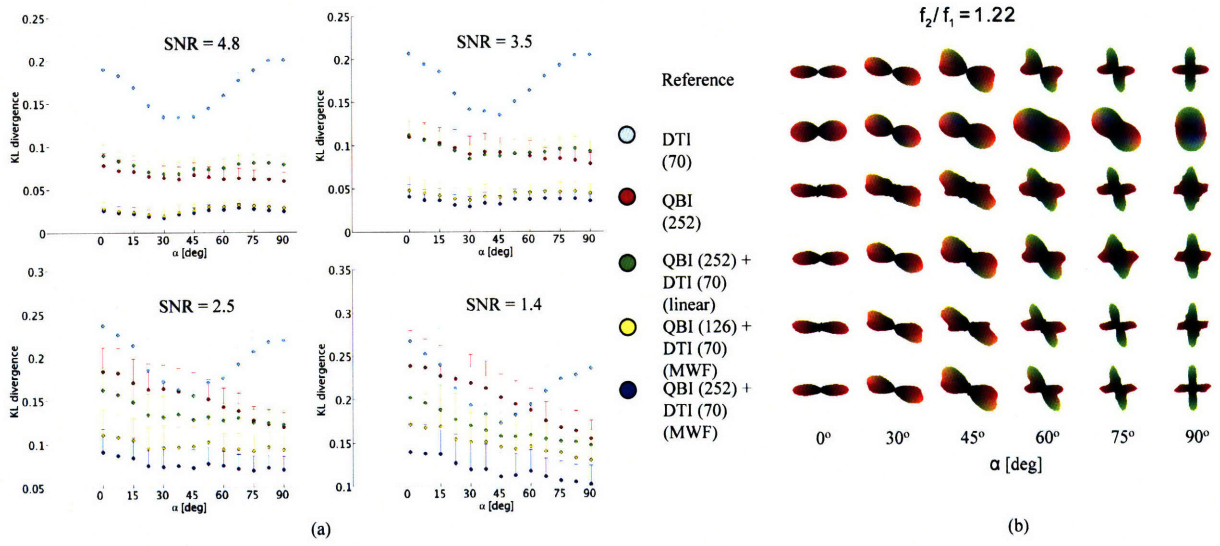

Figure 4-2. (a) Reconstruction accuracy of diffusion ODF reconstruction methods (Table 4-2) for a synthetic 2-Gaussian system with f_1=0.45 and f_2=0.55 for four SNR values. KL (±SEM) divergence between reference ODF and estimated ODF as a function of separation angle α between the principal eigenvector of the Gaussian compartments. (b) ODFs from randomly selected, individual noise trials from (a) with SNR = 2.5.

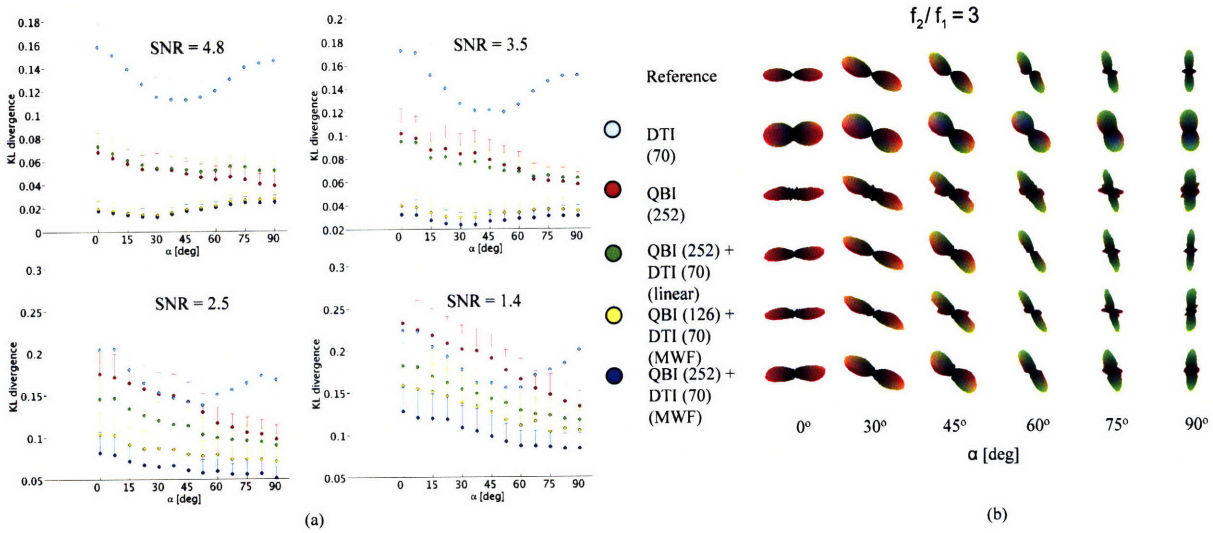

Figure 4-3. (a) Reconstruction accuracy of diffusion ODF reconstruction methods (Table 4-2) for a synthetic 2-Gaussian system with f_1=0.25 and f_2=0.75 for four SNR values. KL (±SEM) divergence between reference ODF and estimated ODF as a function of separation angle α between the principal eigenvector of the Gaussian compartments. (b) ODFs from randomly selected, individual noise trials from (a) with SNR = 2.5.

The reconstruction accuracy of the DTI, QBI, and the MWF technique as a function of total sampling directions is presented in Figure 4-4 for (left) f_1=0.55 and f_2=0.45 and (right) f_1 = 0.25 and f_2 = 0.75. Data points in blue represent the MWF reconstruction accuracy calculated with full sphere QBI sampling where as data points in yellow represent the MWF reconstruction accuracy calculated with hemisphere (z > 0) QBI sampling. DTI with 40 directions (30 dirs. + 10 T2s) and 70 directions (60 dirs. + 10 T2s) was used in the MWF reconstruction. The KL divergence plot in Figure 4-4 suggests that the optimal number of reconstruction directions for QBI is 362. The simulations show MWF with full sphere QBI and a total of 132 directions (92 QBI + 40 DTI) outperforms the 362 direction QBI resulting in an improvement in sampling gain of 274%. Also, MWF with hemisphere QBI and 86 directions (46 QBI + 40 DTI) outperforms 362 QBI resulting in an improvement in a gain of 377%. MWF with hemisphere QBI is not as accurate as full sphere QBI but could be used to minimize scan time.

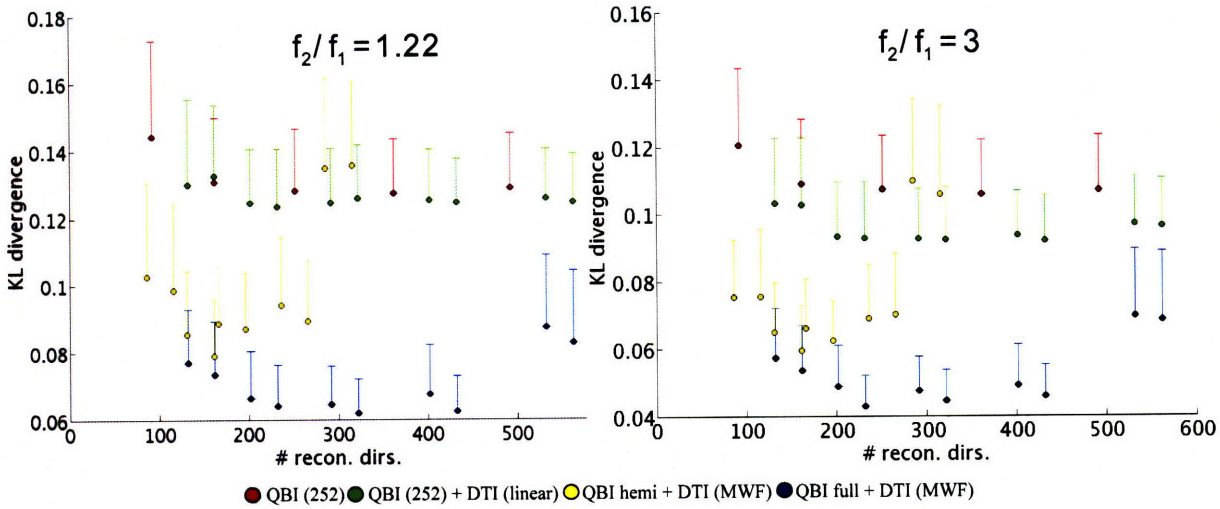

Figure 4-4. Reconstruction accuracy of the DTI, QBI, and the MWF technique as a function of total sampling directions for (left) $f_1 = 0.55$ and $f_2 = 0.45$ and (right) $f_1 = 0.25$ and $f_2 = 0.75$. The subsampling was done by taking only the top hemisphere of directions ($z > 0$) for a given sampling scheme.

4.4.2 Human Data

Figure 4-5 compares the reconstruction methods in the intersection (arrow) between the optic radiation and the arcuate fasciculus. Fibers from the middle temporal gyrus project anteriorly to join with fibers of the arcuate, inferior, and superior longitudinal fasciculi projecting to the frontal lobe. The optic radiations travel posteriorly from the lateral geniculate nucleus to the calcarin sulcus. Crossing between the optic radiation and arcuate sciculus (arrow) cannot be resolved by DTI (Figure 4-5a), is suggested by the QBI map (Figure 4-5b), but is clearly defined on the MWF images (Figure 4-5c,d). Note that the peaks are more clearly defined on the hemisphere MWF (Figure 4-5d) than the full QBI (Figure 4-5b) despite the fewer number of sampling directions.

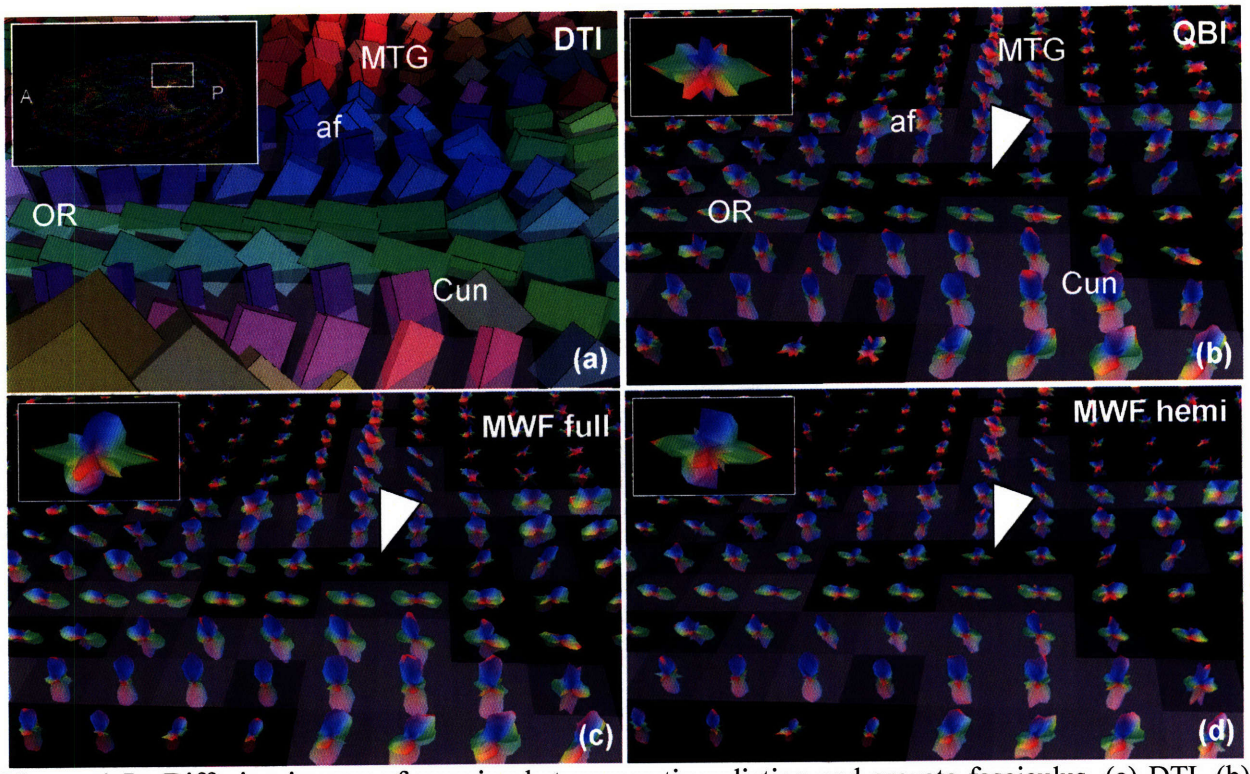

Figure 4-5. Diffusion images of crossing between optic radiation and arcuate fasciculus. (a) DTI, (b) QBI, (c) MWF of DTI and full QBI, (d) MWF of DTI and hemisphere QBI. Note that the crossing peaks (arrow) are more clearly defined on (d) than on (b). af, arcuate fasciculus; Cun, cuneus; MTG, middle temporal gyrus; OR, optic radiation. The ODFs that the arrows point to in (b,c, and d) are magnified in the insets.

Figure 4-6 shows the crossing (arrow) between the posterior cingulum bundle and the splenium of the corpus callosum. The MWF images (Figure 4-6c,d) support the single modal diffusion in the corpus callosum while enhancing the fiber crossing at the interface between the callosum and the cingulum bundle. The crossing is more clearly defined on the hemisphere MWF than on the standard QBI.

The IPCM in Eq. (4.3) was applied to the QBI and MWF results for all participants. Table 4-3 summarizes the difference of the mean IPCM of MWF and QBI in white matter (WM) voxels (DTI FA > 0.2). The difference in mean IPCM between the 252 QBI and 196 MWF illustrates the sampling efficiency gain of the MWF technique. A one sample t-test of the mean difference between the connectivity metric in WM for the six participants (II-VII) from Table 4-3 yields a value of $p = 4.6 \times 10^{-9}$.

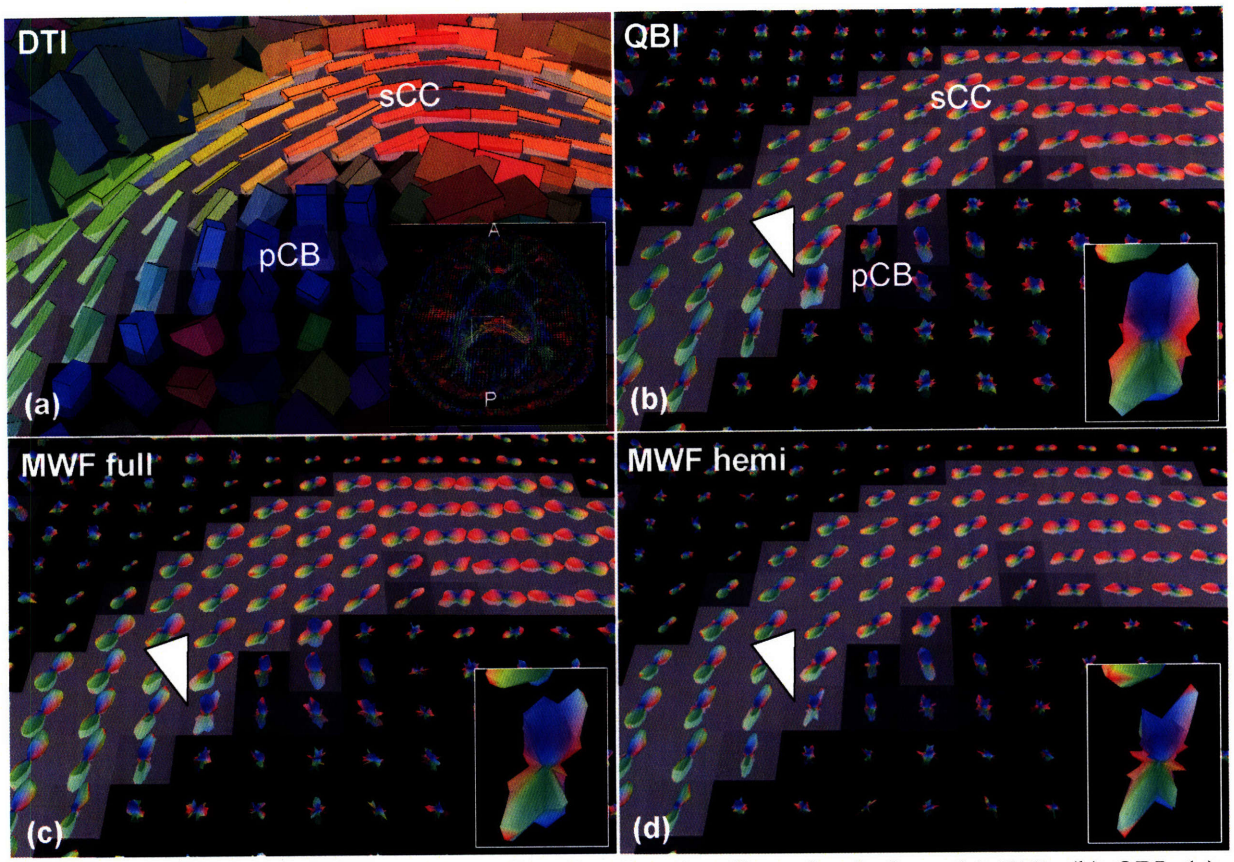

Figure 4-6. Intersection between posterior cingulum bundle and splenium. (a) DTI, (b) QBI, (c) MWF of DTI and full QBI, (d) MWF of DTI and hemisphere QBI. The crossing peaks (arrow) are discernible on the MWF images (c,d) but not the standard QBI (b). pCB, posterior cingulum bundle; sCC, splenium of corpus callosum. The ODFs that the arrows point to in (b,c, and d) are magnified in the insets.

Table 4-3. Difference of the mean IPCM between the MWF and QBI reconstructions for seven subjects in white matter.

Participant	**322 MWF vs. 252 QBI** $\left(\overline{IPCM_{MWF_{WM}}} - \overline{IPCM_{QBI_{WM}}}\right)$	**196 MWF vs. 252 QBI** $\left(\overline{IPCM_{MWF_{WM}}} - \overline{IPCM_{QBI_{WM}}}\right)$
I	1.086×10^{-5}	0.872×10^{-5}
Participant	**192 MWF vs. 122 QBI** $\left(\overline{IPCM_{MWF_{WM}}} - \overline{IPCM_{QBI_{WM}}}\right)$	
II	1.095×10^{-5}	
III	1.069×10^{-5}	
IV	1.034×10^{-5}	
V	1.103×10^{-5}	
VI	1.124×10^{-5}	
VII	1.102×10^{-5}	

The MWF technique show more intravoxel peak connectivity in white matter throughout the brain as shown in Figure 4-7 which compares the IPCM in six slices between the 252 QBI and the 196 MWF for a single participant.

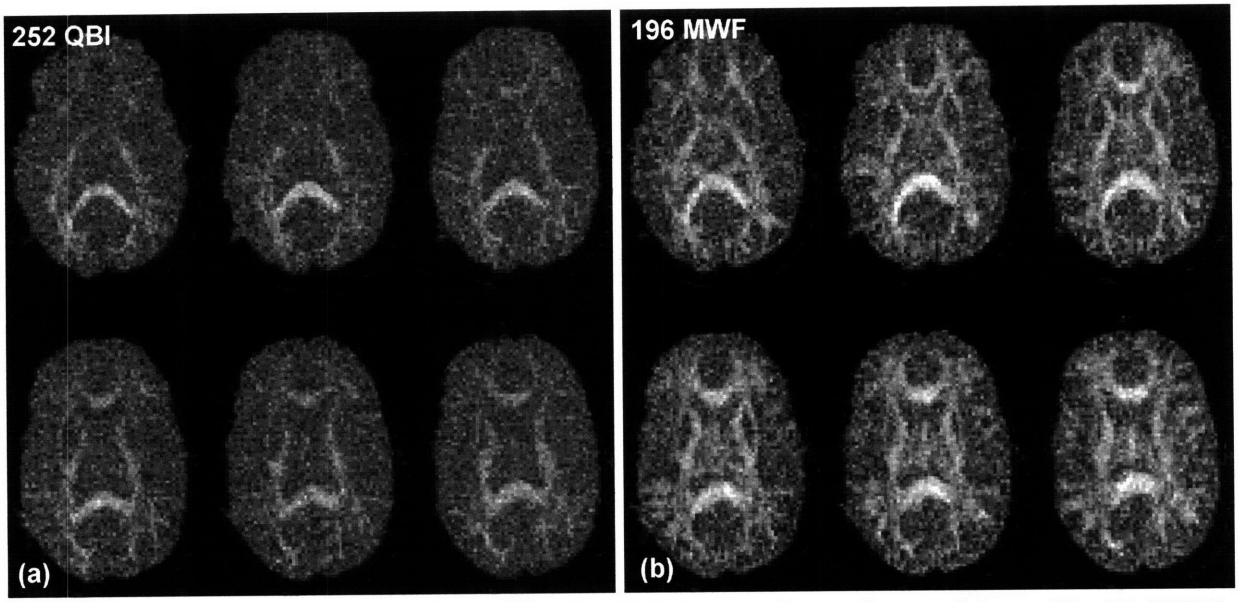

Figure 4-7. (a) IPCM calculated for 252 dir. QBI in six slices of a participant (I). (b) IPCM calculated for 196 dir. MWF in the same six slices as (a). All images are on the same scale.

Figure 4-8 illustrates the robustness of the MWF technique comparing the ICPM over six subjects between 122 QBI and 196 MWF.

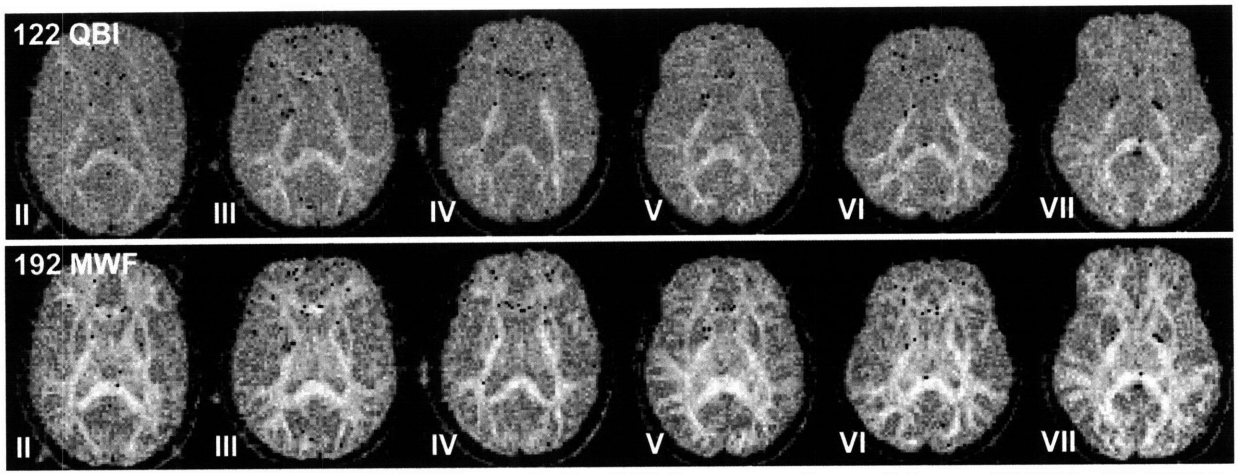

Figure 4-8. (a) IPCM calculated for 122 dir. QBI in across six participants (II-VII). (b) IPCM calculated for 196 dir. MWF in the same slices as (a). All images are on the same scale.

4.5 Discussion

The greatest challenge faced by all who develop diffusion measurement techniques is how to quantify the accuracy of the reconstruction. The ground truth could be obtained through histological validation of diffusion imaging. In this section, we present a connectivity metric in Eq. (4.3) that rewards intravoxel peak connectivity. The purpose of this metric to compare *in vivo* HARDI reconstructions. The benefit of using this metric is that it does not assume anything about the underlying shape of the diffusion propagator.

The numerical simulations and human data indicate the MWF technique provides a more accurate estimate of the ODF over a range of fiber angles. (Figure 4-2, Figure 4-3) and different SNR values. The fusion is nonlinear and so the noise propagation will be nonlinear. In addition, Figure 4-4 provides illustrates the efficiency gain with the MWF technique. MWF of full sphere QBI provides a 274% increase in reconstruction accuracy compared with 362 direction QBI. MWF of hemisphere QBI provides a 377% increase in sampling efficiency compared with 362 direction QBI.

The improved accuracy of the MWF technique stems from the fact that the DTI provides the basic low angular resolution structure of the diffusion propagator with high SNR while the QBI provides the high angular resolution information with low SNR. By combining the data in such a way to use the high SNR from the DTI to stabilize the QBI reconstruction in a given neighborhood around a certain direction ($\approx 10^{o}$ on the sphere in our case), it is possible to improve the angular resolution of the ODF. Taking a single wavevector would give some form of a weighted average of the DTI and QBI. An average of the data is shown to be less optimal than a non-linear fusion in the numerical simulations. In addition, the MWF technique retains the model independency since it assumes nothing about the shape of the underlying diffusion propagator. For this reason, the MWF technique is applicable to combining DTI with any HARDI technique from which an ODF can be calculated.

The fusion technique requires combining data with different TEs and diffusion times. The echo time, TE, for a DTI scan is $\approx$ 80 ms whereas the echo time for a QBI scan is nearly $\approx$ 115 ms. Thus, DTI and QBI have different T2 weightings. The T2 normalization will account for the overall differences in T2 however this will not account for intra-voxel T2 heterogeneity.

In the DTI and QBI acquisition the diffusion time is also different. Due to the high b-values used in QBI, the diffusion time has to be increased due to SAR constraints on gradient

slew rates and gradient overheating. However, there is no evidence for a change in the mean diffusivity, fractional anisotropy, or eigenvectors over a range of diffusion times [46]. Therefore, the DTI data measured with an echo time similar to QBI would not result in significantly different eigenvectors. This leads to the interpretation that in effect the MWF technique combines diffusion data from different length scales.

In QBI b-values between 2500 and 4500 have been shown to resolve fiber crossing without sacrificing SNR [24]. Similarly b-values for DTI of 500 to 1000 have been shown to resolve white matter architecture [18]. It is very possible that sampling directions of 70 DTI and 252 QBI is not the optimal choice. In fact, the authors found that only 123 QBI directions were need to obtain desirable MWF results (Figure 4-5, Figure 4-6, and Figure 4-7). Future work includes the optimization of the relevant experimental parameters (b-value, sampling directions).

4.6 Conclusion

We have described a reconstruction method for fusing diffusion images acquired with different diffusion wavevectors. Also, a intravoxel peak connectivity metric (IPCM), is presented to compare HARDI reconstruction methods. The IPCM rewards ODFs that points to peaks in neighboring voxels. Numerical simulations showed that the MWF fusion procedure provided greater reconstruction accuracy than linear fusion, despite using fewer sampling directions resulting in an improvement in efficiency of 274% - 377% depending on the sampling scheme. MWF fusion of DTI and QBI data of human resolved more white matter as measured by the IPCM as compared to QBI for all sampling schemes presented. The improved reconstruction accuracy provided by the MWF reconstruction promises to boost the sampling efficiency and clinical feasibility of QBI. Future work will focus on using the IPCM to optimize the wavevector fusion rule, wavevector combination, sampling scheme, and b-values.

§5 Design of a MRI-Compatible Cortical Cooling System[2]

5.1 Introduction

In order to investigate the effect of cerebral glucose metabolism on cerebral diffusion and the hemodynamic response, it was necessary to develop an MR-compatible cortical cooling system capable of reversibly deactivating cerebral glucose metabolism[2]. Previous cortical cooling systems used flexible stainless steel tubing (OD = 0.95 mm)[47] to cool cortical tissue which is not MR-compatible. The design of an MR-compatible cortical cooling system presents a number of material and design challenges. The material used to cool the cortical tissue must have good heat transfer properties while minimizing distortions in the image.

The next section describes the available reversible deactivation techniques and their advantages and disadvantages.

5.2 Background

Reversible deactivation in relation to neuroscience refers to the ability to control some aspect of neural activity over a finite time period. When using any reversible deactivation technique, there must be a well-defined region of deactivation. It is also desirable to quantify the degree of deactivation in the region. Two of the most widely used reversible deactivation techniques that can control cerebral glucose metabolism are (1) cortical cooling, and (2) drug injection[48]. Cortical cooling limits neural capabilities by affecting cerebral glucose metabolism [35]. Below a critical temperature (termed metabolic cutoff = 20 °C), glucose metabolism ceases because the chemical reactions necessary to produce energy cannot occur below this temperature [47,49]. In most reversible cooling deactivation studies, a small cryoloop or peltier element is implanted in the brain of an animal and can be turned on/off to control glucose metabolism. In the proposed experiments combining reversible deactivation with MRI, the advantage of using temperature to control glucose metabolism is that MRI can calculate temperature maps using proton resonance frequency shift thermometry (PRFST) dynamically during a reversible deactivation experiment. Therefore, the degree and extent of the deactivation region could be quantified because it is directly related to temperature.

Another type of reversible deactivation technique that can control cerebral glucose metabolism is drug injection. There exist a number of drugs to reversible deactivate different

aspects of brain function such as local anesthetics, sodium channel blockers, inhibitory neurotransmitters, and excitatory neurotransmitter antagonists having durations of deactivation of 1 hour to one day [35]. The only drugs that are capable of limiting metabolic flow through cerebral metabolism are local anesthetics like lidocaine and tetrodotoxin [35]. The advantages of using drug injection to control cerebral metabolism is that it does not have a direct effect on diffusion as does temperature. The major disadvantage with drug injection is that multiple reversible deactivation experiments cannot be performed during the same scanning session since the minimum reversal deactivation time is 1 hour (local anesthetics). Also, a limited number of drug injections can be performed before the cortical tissue is damaged. Another disadvantage is that it is more difficult to quantify the deactivation region because of the low MR sensitivity (10^{-5}) of NMR spectroscopy compared to conventional MRI. Table 5-1 outlines the advantages and disadvantages of reversible deactivation by cortical cooling and drug injection.

Table 5-1. Advantages and disadvantages of using cortical cooling and drug injection.

Technique	Advantages	Disadvantages
cortical cooling	1. Measure the region and degree of deactivation. 2. Cycle through many deactivations during an experiment.	1. Direct effect on diffusion.
drug injection (e.g., lidocaine or TTX)	1. No known direct effect on diffusion. 2. Structures below cortical surface can be deactivated.	1. Long deactivation time (> 1 hour). 2. Difficult to administer in magnet. 3. Difficult to quantify deactivation region. 4. Limited number of drug injections.

Primary visual cortex (V1) would be a suitable deactivation region. V1 is known to receive feedforward connections from LGN and feedback connections from higher order visual areas (V2, V3, V4, etc.). By reversibly deactivating V1, regions which receive input or output from V1, which are not affected by changes in temperature, may also be affected [50]. Hence we expect to see changes in cerebral diffusion and the hemodynamic response at sites distant from the deactivation region.

5.3 Design Specifications

The ideal cortical cooling system would have the following properties:

A. cryoprobe
   1) maintains structural integrity at low temperatures (-60 °C)

2) biocompatible with tissue (i.e. dura, cortex)
3) minimal susceptibility artifacts
4) consistent placement above desired deactivation region

B. cooling properties
1) cool cortical tissue below the metabolic cutoff (< 20 °C) within minutes (< 5 minutes)
2) cooling fluid with low freezing point (< -100 °C)[47]
3) even in the case of a leak, no cortical damage should occur (passive system)
4) variable deactivation region: 0 - 0.4 cm^3

5.4 Cryoprobe

An ideal choice for the material of the cryoprobe is fiberglass (Polymer Plastics Corp - G10/FR4 Fiberglass – Sheet Thickness 0.05 mm and 0.20 mm). It is often used in MRI experiments (coils, preamps, etc.) and causes negligible susceptibility artifacts. Also, fiberglass is a biocompatible material.

A coolant probe was built out of fiberglass and maintained its structural integrity for methanol temperatures in the range of -80 to 20 °C. A picture of the coolant probe is shown in Figure 5-1a. The cylindrical symmetry of the cooling probe ensures a consistent deactivation region in all experiments. The coolant probe is glued together using adhesive hardener and resin (Gougeon Corp. - G5 Adhesive Hardener and Resin). More recent cryoprobes use silicon sealant. The cryosurface is ~ 0.6 mm thick.

Fiberoptic thermocouples (00-11874-01, Luxtron Corp.) were placed on the dura during experiments to ensure the dura was not cooled below the freezing point (Figure 5-1a). The fiber optic thermocouples ensured a constant cooling profile between deactivations. Thermocouple readings were recorded at 4 Hz.

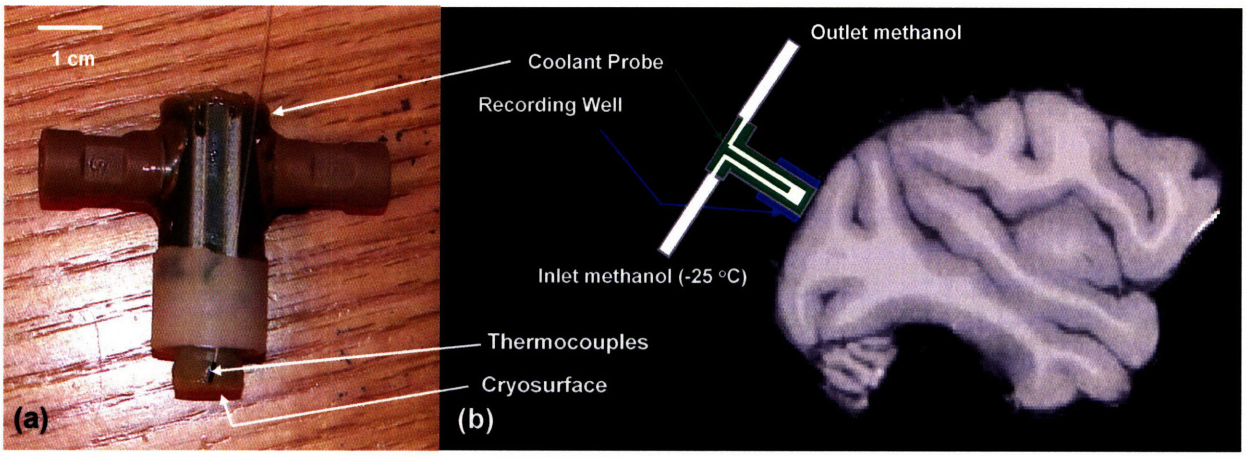

Figure 5-1. (a) Coolant probe used and attached thermocouples. (b) Schematic (not to scale) of coolant probe orientation on the dura above V1. The radial symmetry of the probe ensured that it was in the same position for each experiment.

The coolant probe was mounted on the dura of the monkey using the recording well shown in Figure 5-2. The recording well is secured to the skull of the monkey using dental acrylic.

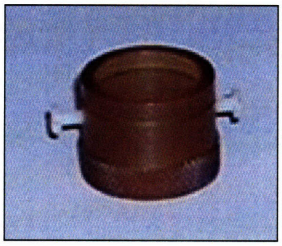

Figure 5-2. Recording well used in cortical cooling experiments. The recording well was glued to the skull using dental acrylic.

5.5 Pump System

A schematic of the cooling system is shown in Figure 5-3.

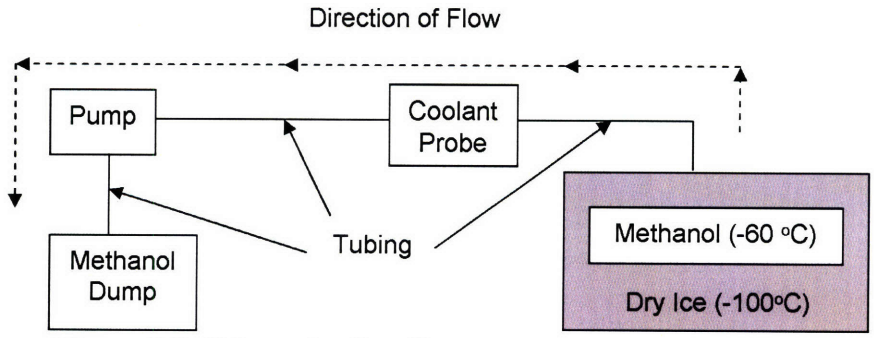

Figure 5-3. Schematic of cooling system.

The methanol is pulled through the cooling probe. This ensures the pressure inside the tubing is always lower than the ambient. Therefore, in case of a leak, air enters the line, and no methanol will have spilled onto the dura. Table 5-2 provides a list of the equipment in the cortical cooling system (Figure 5-3).

Table 5-2. Description of the cortical cooling system components.

Part	Description	Company
Pump	QSY - 120 V AC Pump; Flow Rate = 0 – 51.8 mL/min	FMI Pump
Tubing	3 mm OD/2mm ID Teflon Tubing	Upchurch Scientific
Ferrules & Nuts*	10/32" Thread	Upchurch Scientific
Methanol	reagent grade anhydrogenous, S75965	Fischer Scientific

5.6 Cooling System Properties

The cooling system met the design specifications. Methanol was used as a coolant fluid (freezing point ~ 110 °C). The cortical tissue as measured by MR thermometry under the cryoprobe can be cooled below the metabolic cutoff in one minute. In Figure 5-4, the thermocouples on the cortical surface shown the consistency of the cooling profile of the cortical cooling system for three trials.

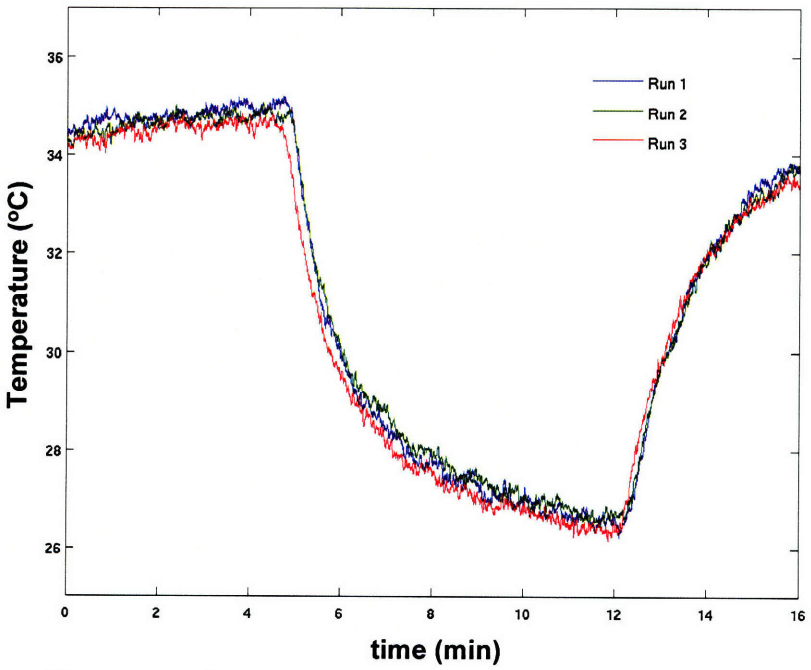

Figure 5-4. Thermocouple readings on the cortical surface during a cooling profile for three trials. The thermocouple measurements illustrate the consistency of the cooling profile.

5.7 Conclusions and Future Work

In this section we present a novel MR-compatible cortical cooling system capable of reversibly deactivating cerebral glucose metabolism of cortical tissue. Reversible deactivation can be achieved in 1 minute. The cooling probe does not create significant susceptibility distortions and is radially symmetric to ensure consistent placement above the deactivation region. Also, the flow rate of the cortical cooling system is consistent during multiple deactivations. Future work includes automated control of the cooling pump to allow for programmable cortical cooling profiles. In the next section, the cortical cooling system is applied to measuring the effect of cerebral glucose metabolism on cerebral diffusion.

§6 Reversible Deactivation of Cerebral Glucose Metabolism Affects the Diffusion MRI Signal[51]

6.1 Introduction

Diffusion-weighted MRI has emerged as a powerful tool to investigate a wide range of neuropathologies such as stroke, Parkinson's disease, HIV dementia, schizophrenia, cocaine addiction, normal aging, Alzheimer's disease, chronic alcoholism, multiple sclerosis, epilepsy, and ALS[52,53]. More recently, diffusion MRI has also been proposed as a promising technique to identify anatomical white-matter fiber tracts *in vivo*[54] and measure neural activity[55].

Diffusion MRI measures the Brownian motion of water molecules in brain tissue on length scales ranging from 10 nm to 100 μm, and on time scales ranging from 1 ms to 1 s[21]. In clinical diffusion MRI, the two scalar measures of diffusion in cerebral tissue are the apparent diffusion coefficient (ADC) and fractional anisotropy (FA). The ADC represents the magnitude of the diffusion whereas the FA is a measure of its anisotropy. Despite the widespread applications of diffusion MRI in basic and clinical neuroscience, the underlying biophysical mechanisms which affect diffusion contrast (ADC and FA) remain largely unknown[35].

Initially, it had been assumed that FA in cerebral white matter was caused by the diffusion barrier presented by the myelin sheath, however, recent evidence indicates that myelin is not *necessary* for diffusion anisotropy. For example, diffusion anisotropy has been observed in de-myelinated garfish nerve *ex vitro*[56], pre-myelinated newborn white matter[57], cortical gray matter in rat[58], and the thalamus[59]. Furthermore, FA changes in ischemia studies have been shown to occur over longer time periods (hours to days) and after lesions causing anterograde and retrograde secondary white matter degeneration[60,61].

With regards to the ADC, a recent study suggested that the ADC depends on neuronal activity[55]. Another study suggested that the ADC of water decreased during the inhibition of fast axonal transport, although this study was confounded by crystal formation during the artificial breakdown of microtubuli which could have affected the ADC[56]. Because of the decrease in ADC during ischemia and spreading depression, and since digestion of microtubuli leads to decreases in ADC[35], we hypothesized that processes dependent on cerebral glucose metabolism affect the ADC.

The goal of this study was to effectively block cerebral glucose metabolism in a reversible manner and quantify the effect of the reversible deactivation on ADC and FA.

Two often used types of reversible deactivation methods are cortical cooling and drug injection. In this experiment, we developed a magnet-compatible cooling probe which allowed us to focally deactivate and reactive cortical tissue over a shorter time scale (~ minutes) than drug injection (~ hours)[48]. Hence, we could perform multiple deactivations in the same scan session.

It is well-established that cooling cortical tissue below 20 °C abolishes glucose metabolism, hence also neuronal activity [47,49]. Here, we focally deactivated cerebral glucose metabolism while we measured ADC and FA before, during, and after cooling. By reversibly deactivating cerebral glucose metabolism, we avoided other confounding mechanisms that could contribute to the diffusion signal as observed during neuropathology. These mechanisms include, for example, functional and anatomical reorganization (plasticity), local swelling, blood accumulation, macrophage infusion, gliosis, and necrosis.

Hitherto, it has been difficult to quantify *in vivo* the degree and extent of brain tissue that is inactivated, irrespective the deactivation method applied (i.e. cooling, drug injection). To overcome this problem, we measured the temperature of the brain inside the MR-scanner using proton resonance frequency shift thermometry (PRFST) [62,63]. This allowed us to calculate 3D temperature maps (isothermals) at a temporal resolution of four seconds and to infer the amount of deactivated cortex during a cooling experiment (i.e. glucose metabolism is blocked at a temperature below 20°C)[47-49,64]. *Ex vivo* comparisons of MR-thermometry with MR-compatible thermocouples were performed to calculate the accuracy and precision of the PRFST method.

A potential confound during combined cooling-DTI experiments is the temperature dependence of ADC, such that a change in the ADC may simply reflect a change in temperature. However, the *in vivo* acquired 3D temperature maps allowed us to quantify precisely ADC changes in voxels in which temperature did not change.

In summary, we were able to reversibly deactivate cerebral glucose metabolism of a small portion of V1 in a magnet-compatible manner. Short-term deactivation led to pronounced changes in ADC, but not FA, in voxels at distant sites from the deactivation region where the temperature had not changed.

6.2 Background

Diffusion-weighted MRI has emerged as a powerful neuroimaging tool for identifying neuropathology in cerebral white matter [52,53] and has been proposed as a technique capable of mapping white matter axonal pathways *in vivo* [54]. However, the underlying mechanisms of cerebral diffusion contrast in the brain remain largely unknown [35]. In clinical diffusion MRI, the two scalar measures of diffusion in cerebral tissue are the apparent diffusion coefficient (ADC) and fractional anisotropy (FA). The ADC represents the magnitude of the diffusion whereas the FA is a measure of its anisotropy. The diffusion anisotropy (FA) is larger in white matter where there is more diffusion along the axon than perpendicular to it [52,53]. Changes in the FA in white matter have been observed in a number of neurodegenerative diseases[35]. Understanding the underlying mechanisms of the ADC and FA in the brain is key to providing biological interpretations for diffusion MRI findings in clinical and basic neuroscience. There is an intriguing line of evidence to suggest that intraaxonal flow associated with cerebral glucose metabolism may contribute to the ADC and FA[56]. The metabolic flow hypothesis maintains that intraaxonal flow associated with axonal transport can generate water diffusion detectable in the diffusion MR signal. While this theory had been considered speculative, it is now receiving increased attention in light of findings that myelin does not contribute substantially to FA[56].

Researchers have suggested a number of possible mechanisms that affect cerebral diffusion, although no explanation or combination of explanations has been shown to fully account for diffusion contrast (either ADC or FA). It is useful to break the different possible mechanisms into five categories: (1) myelin and axonal membranes, (2) microtubules/neurofibrils associated with fast axonal transport, (3) susceptibility induced nerve gradients in the nerve and white matter, (4) multiple compartmental diffusion caused by cellular edema, (5) surface relaxation, and (6) metabolic flow [35,65-67]. The myelin was thought to be the dominant cause of FA in DTI because its lipid bilayers are relatively impermeable to water. However, large FA values were found in non-myelinated olfactory nerves in the garfish [56]. Also, studies have found that diffusion anisotropy is still observed in newborns even though myelin has not been developed [57]. This is not to say that myelination is not a source of anisotropy, but it is not the only cause. It has also been hypothesized that the complex cytoskeleton of axons with longitudinally oriented microtubules, which allows fast axonal transport, affects the ADC and FA. However, it was shown that by depolymerizing the structure

of microtubules, which is thought to inhibit fast axonal transport, did not change the anisotropy in the nerves of the spotted and long-nosed garfish *ex vitro* although the ADC decreased [56]. Later, experiments using the axon of a squid showed longitudinal neurofibrils did not affect FA [68]. FA has also been postulated to be caused by susceptibility induced gradients in the nerve due to the static magnetic field, B_0. [69,70]. It is well known that during stroke and a number of other brain pathologies, neurons swell and the ADC drops by 30% [67,71]. This swelling, called cellular edema, is thought to restrict the motion of water in the region outside the cell thus causing a decrease in the diffusion signal. This hypothesis is a cause of great controversy in the field and there has been no concrete evidence to support it [35]. Surface relaxation of the magnetization near boundaries in the brain has also been suggested, but no studies have attempted to test this hypothesis.

The studies above suggest that there are multiple mechanisms affecting cerebral diffusion. The difficulty in determining which mechanisms effect cerebral diffusion, is that none of the mechanisms proposed so far can be controlled *in vivo*. One possible mechanism that could affect cerebral diffusion and has not been explored but can be controlled *in vivo* (by reversibly deactivation) is cerebral glucose metabolism. Cerebral glucose metabolism is the process by which cells produce energy (glycolysis), is involved in the regulation of ion channels, and also effects axonal transport and processes related to the trafficking of proteins to and from the axons. This flow process has two components, termed fast and slow axonal transport. An illustration of metabolic flow is given in Figure 6-1 [72].

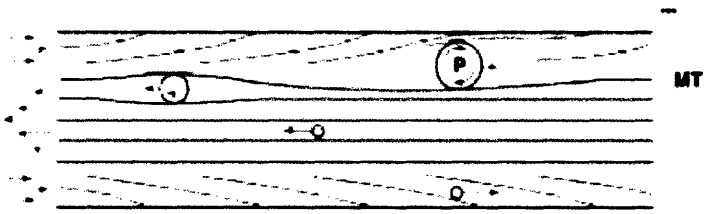

Figure 6-1. Schema [72]. The heterogeneity of flow velocities can give rise to apparent diffusion.

The effect of cerebral glucose metabolism on the diffusion MRI signal could be addressed by acquiring DTI before, during, after reversible deactivation of cerebral glucose metabolism.

6.3 Methods

6.3.1 Animals

MRI data were acquired from two juvenile male rhesus monkeys (macaca mulattas, M1: 5.5 kg, ID #M4000, M2: 4.2 kg, ID #1506). A 0.75 inch diameter recording well (Crist Instruments, Washington, DC) was placed over V1 of the right hemisphere. The recording well exposed the dura and was sealed with a cap when the monkey was not in the scanner. The data were acquired on a Siemens Allegra (M1) and Trio (M2) 3T MRI scanner located at the Athinoula A. Martinos Center for Biomedical Imaging, Massachusetts General Hospital (Charlestown, Massachusetts). All procedures conformed to Massachusetts General Hospital and National Institutes of Health guidelines for the care and use of laboratory animals (Subcommittee on Research Animal Care protocol #2003N000338). The animal was anaesthetized with a ketamine and xylazine (induction 10 and 0.5 mg/kg, i.m., maintenance with ketamine only). The monkey was placed into a magnet compatible stereotactic apparatus. Local anaesthetic (lidocaine cream) was applied to the ends of the ear bars and ophthalmic ointment was applied to the eyelids to minimize discomfort induced by the stereotactic apparatus. A heating pad was placed beneath the monkey to keep it warm during the scan session.

6.3.2 RD Cooling System

Right hemisphere primary visual cortex was deactivated by placing an MR-compatible coolant probe on the surface of the dura above V1. The probe was made from G10/FR4 (fiberglass). Up to three fiber optic thermocouples (00-11874-01, Luxtron Corp.) were placed on the lateral side of the probe (see Figure 5-1) surrounding the cooling surface. In experiments on M2, the recording well was adapted to allow a thermocouple to be placed directly under the cryo-surface of the cooling probe. All thermocouples touched the dura during the experiment and yielded a real time measure of the cortical surface temperature. Methanol (reagent grade anhydrogenous, S75965, Fisher Scientific) was passed through the probe with a pump (QV pump, Q3 pump head, FMI Pump). Teflon tubing (1667xl, Upchurch Scientific) was used to transfer the methanol from the pump, and ferrules and nuts (P-343 ferrule, P-331 nut, Upchurch Scientific) were used to secure the tubing to the pump and coolant probe.

6.3.3 Experimental Design

DTI was acquired at the beginning of the experiment while warm methanol flowed through the coolant probe. The brain was then cooled for 11 minutes while magnetic resonance (MR) thermometry images were taken. Flow rates ranges from 50 mL/min - 120 mL/min and inlet temperatures (1 meter from probe) ranged from -30 °C to -70 °C during the experiments. Only flow rates > 80 mL/min and inlet methanol temperatures < -40 °C resulted in cortical deactivation below the metabolic cutoff of 20 °C. Such low temperatures were needed because of the thermal conductivity properties of the fiberglass used to build the cooling probe. After 11 minutes, the temperature distribution in the brain was at equilibrium as measured by the supra-dural thermocouples. DTI was acquired during the remainder of the cooling period (~ 30 minutes). The temperature of the brain was then raised for 8 minutes using methanol at room temperature while MR thermometry images were taken. DTI images were then taken during the recovery period. Below is a description of the DTI, MR thermometry, and T1-weighted anatomical images acquired.

6.3.3.1 High resolution T1 images

For both monkeys, high resolution T1 images were acquired in a separate session with an MPRAGE sequence[19] with TR/TI/TE = 2500/1100/4 ms, $\alpha = 8^{o}$, 0.35 mm isotropic resolution, total acquisition time: 16 min. Eight T1 images were acquired with this sequence and reconstructed (motion corrected, averaged, and normalized) using Freesurfer, http://surfer.nmr.mgh.harvard.edu. The resulting T1 image was used as a template to co-register all diffusion images, and temperature maps.

6.3.3.2 Thermocouple measurements

Using a Luxtron 3100 Fluoroptic Thermometer (Luxtron Corp.), the thermocouples values were read and stored at 4 Hz throughout the entire experiment. The thermocouple readings were not applied in the analysis of the data but were used during the experiment to approximate the temperature of the deactivation region and to ensure an equilibrium temperature distribution during the cooling period (as was always verified post-hoc using the PRFST method).

6.3.3.3 DTI

Twenty-five axial slices were taken of the monkey at a slice thickness of 2.0 mm (0 mm skip). The in-plane resolution was 2.0 x 2.0 mm, with a matrix size of 64 x 64. The sequence parameters were TR/TE = 5500/87 ms, b = 700 s mm^{-2}. The diffusion gradient sampling scheme consisted of n = 60 directions which were obtained using the electrostatic shell method[17]. Ten images with no diffusion weighting were also obtained for a total of 70 acquisitions. The total acquisition time was 5 min 31 sec. ADC and FA maps were calculated from all diffusion scans[18]. The ADC was calculated by taking one-third of the trace (see Eq. (3.7)).

6.3.3.4 MR thermometry

MR thermometry imaging employed single shot multi-slice echo planar imaging with an isotropic resolution of 2.0 mm. Twenty-five axial slices were acquired using TR/TE = 4000/19 ms, 128 mm FOV, and a 90- flip angle. Magnitude and phase images were acquired. Temperature maps were calculated from the MR thermometry scans using the proton resonance frequency shift thermometry (PRFST) method which relates the temperature change to the difference in phase between successive time points[62,63]. The equation reads

$$\Delta\varphi = 2\pi \cdot \alpha \cdot \gamma \cdot TE \cdot \Delta T \qquad (4.1)$$

where $\Delta\varphi$ is the change in phase, α is the thermal coefficient (0.01 ppm/°C), TE is the echo time of the pulse sequence, and ΔT is the temperature change. Eq. (4.1) needed to be modified to account for the linear phase drift that occurs even in voxels where the temperature does not change. The change in the phase drift is constant over the image so Eq. (4.1) can be rewritten as

$$\Delta\varphi = 2\pi \cdot \alpha \cdot \gamma \cdot TE \cdot \Delta T + \Delta\varphi_{drift} \qquad (4.2)$$

where $\Delta\varphi_{drift}$ is calculated in a region far from the probe where the temperature has not changed.

The accuracy and precision of the MR temperature maps was quantified by cooling *ex vivo* muscle tissue. One cooling cycle lasted 5.5 minutes and was followed by a warm epoch of 7 minutes. The accuracy of the MR temperature maps relative to the thermocouple readings was quantified by averaging four voxels surrounding the thermocouple. The precision of the MR temperature maps was quantified by calculating the standard deviation of the temperature in a region far from the cooling probe.

6.3.3.5 Low resolution T1 images

Low resolution T1 images were acquired during each trial with an MPRAGE sequence[19] with TR/TI/TE = 2730/1100/3.19 ms, $\alpha = 8^{o}$, 1.5 mm isotropic resolution, total acquisition time: 2 min 54 seconds. Six T1 images were acquired for all experiments with this sequence and reconstructed (motion corrected, averaged and normalized) using Freesurfer, http://surfer.nmr.mgh.harvard.edu. All diffusion and temperature maps from an individual trial were registered to this image. The low resolution T1 image was then registered to the high resolution image (template). The transformation matrix from this registration was then applied to the diffusion and temperature maps so all analysis could be performed in the high resolution coordinates.

6.3.4 Image Registration and Visualization

Images were registered using the flirt command (rigid registration, 6 degrees of freedom) in the FSL toolbox (http://www.fmrib.ox.ac.uk). All visualization post-processing was performed using custom software written in Matlab (version 6.5.1.199709 (R13) Service Pack 1).

6.3.5 Statistical Analysis

6.3.5.1 Nonparametric Permutation Testing (NPPT)

NPPT was applied using the method of Nichols[73]. For each experiment, n = 500 permutations of 5 time points of condition A (warm) and 5 time points of condition B (cold) were performed. P-value maps were generated using a standard two sample t-test. The maximum cluster size (CS) was calculated for each permutation considering p-values < 0.05 using Matlab with a connectivity of 26 (i.e. each voxel in the cluster was surrounded by 26 statistically significant voxels, $p < 0.05$). The final p-value map was calculated using the equation

$$p_{final} = \frac{\sum_{n=1}^{500} (p_i < p_o)}{n} \qquad (4.3)$$

where p_o is the p-value of the original time series and p_i is the p-value from the i^{th} random permutation of the time series. The threshold for the size of statistically significant regions in the final p-value map was determined by considering the distribution of the maximum CS. The

minimum statistically significant cluster size was determined to be the 25th largest cluster size in the maximum CS distribution (i.e. 5% confidence for n = 500 is 25). The results from the NPPT analysis were used to determine suitable regions for the ROI analysis.

6.3.5.2 ROI Analysis

The statistically significant region found by NPPT was split into three sub ROIs based on temperature. The three temperature ranges were: > 34 °C (no temperature change), 20-34 °C, 8-20 °C (deactivated region). The value of 34 °C was chosen as the ambient cutoff because the precision of the *ex vivo* temperature measurements in a voxel was ±1.8 °C at a resolution of 2.0 x 2.0 x 1.1 mm. Therefore, the uncertainty in the *in vivo* temperature measurements at a resolution of 2.0 mm isotropic was ±1 °C. Thus, 37 ± 3σ °C or 37 ± 3 °C represented the 99% confidence interval where temperature did not change significantly ($p > 0.01$) from the ambient.

6.4 Results

We first give a short overview of the different experiments and analyses. Ten reversible deactivation experiments were performed on two male anesthetized rhesus monkeys (M1, M2). We cooled striate cortex (lower visual quadrant, surface area ~ 0.7 cm^2) to different cortical temperatures in order to quantify the effect of cortical cooling on ADC and FA. We focused separately on (1) voxels close to the cooling probe where the temperature changed, and (2) on regions at a distance, where no change in temperature was detected. An illustration of the MR-compatible cooling probe and a schematic of the placement of the probe relative to the brain are shown in Figure 5-1.

The cortical temperature during a particular experiment was controlled by adapting the flow rate and temperature of the cold methanol that was pumped through the cooling probe. We measured temperature in two ways: (1) using MR-compatible thermocouples on the dura (see Figure 5-1a) and (2) using 3-D MR thermometry. The MR temperature maps were used to define the extent of the cooling region. We first performed an *ex vivo* experiment on bovine muscle to quantify the accuracy and precision of the temperature maps relative to a magnet-compatible thermocouple (see Figure 6-2 and *Accuracy and precision of the MR temperature maps*).

In the main *in vivo* experiment we used a block design with the three conditions: warm, cold, and recovery epochs (see *Block Design*). Raw ADC and FA maps are shown in Figure 6-3. Nonparametric permutation testing (NPPT) was used to identify regions showing cooling-induced changes in either ADC or FA (see *Nonparametric Permutation Testing (NPPT)*). Figure 6-5 and Figure 6-6 illustrate the results of NPPT for the ADC in both animals. The warm and recovery conditions showed no statistically significant differences in ADC and FA (data not shown) and therefore were considered to be one equivalent condition, termed 'warm' condition throughout the remainder of the text (unless stated otherwise). Consequently, we limit the NPPT analysis to the warm versus cold conditions. NPPT only revealed statistically significant changes in ADC when the cortex was cooled below 20 °C (see *ADC decrease during cortical deactivation*). In addition, NPPT revealed no statistically significant changes in FA between any combinations of conditions (see *FA shows no change during metabolic deactivation*).

An additional ROI analysis was performed on the voxels showing significant changes in ADC by the NPPT analysis. These voxels were subdivided into three ROIs defined by temperature (see *ROI Analysis*). 2D isothermals (lines of equal temperature) were overlaid on ADC maps and showed that changes in ADC extended from the region below 20° C (i.e. where metabolism was blocked) into regions where no temperature changes occurred (hence, where metabolism was unaffected). Two additional control ROIs were chosen near and far from the cooling region to compare changes in ADC as a function of distance from the probe. Table 6-1, Figure 6-7, Figure 6-8, and Figure 6-9 summarize the behavior of the ADC during the warm, recovery, and cold conditions in M1 and M2 respectively (separately for voxels that reached a temperature during the cold epoch of > 34 °C, or between 20 and 34°C, or < 20 °C).

The sections below discuss the experiments and analyses in detail.

6.4.1 Accuracy and Precision of the MR Temperature Maps: *Ex Vivo* Experiment

The accuracy and precision of the MR temperature maps were quantified by cooling muscle tissue *ex vivo*. To this end, we compared 3D-thermometry maps with the temperature measured by a MR-compatible thermocouple placed immediately below the cooling probe in the muscle. The cooling epoch lasted 5.5 minutes and was followed by a 7 minute warm epoch of room-temperature ethanol (20 °C) flowing through the probe. The location of the thermocouple could be accurately (2 mm) determined by locating sharp changes in the phase maps.

Temperature maps were calculated using Eq. (4.2), (see **Methods**). Figure 6-2a shows a 2D temperature map of a slice (at a 2.1 x 2.1 x 1 mm^3 spatial resolution) under the cooling probe. Figure 6-2b shows the MR thermometry values (averaged from four voxels in the first slice under the probe) as compared with the thermocouple measurements from the same location.

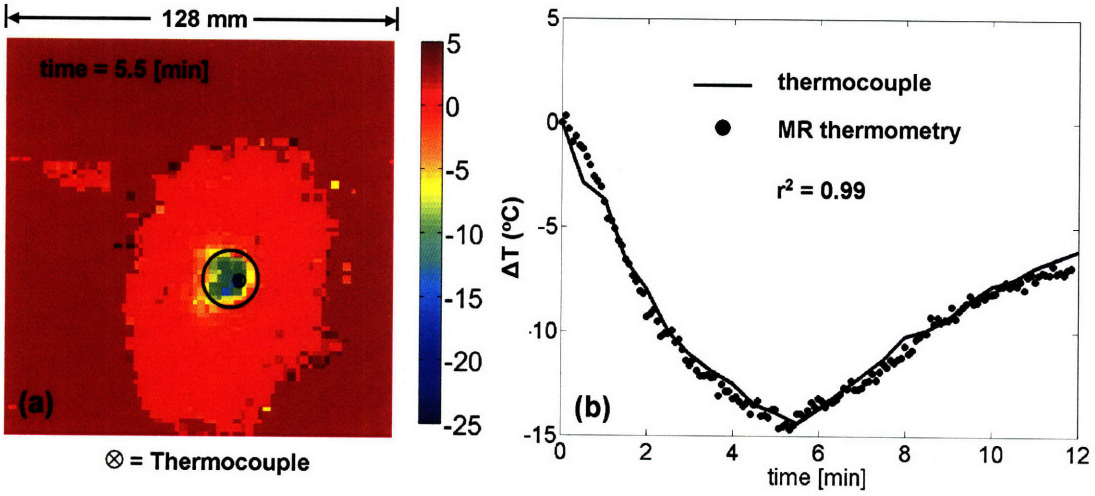

Figure 6-2. (a) MR-defined temperature map during cooling of *ex vivo* bovine muscle (5.5 min. after start of cooling). The location of the probe is indicated by the black circle and the location of the thermocouple under the probe by the circle with an 'x' inside. (b) Plot of MR thermometry measurements (average of 4 voxels) versus thermocouple readings during the cooling and recovery stages of the experiment. Both images shows the change in temperature from the ambient (22 °C).

The precision of the MR-based temperature maps was ± 1.8 °C and the accuracy of the average of four voxels was within ± 0.7 °C of the thermocouple measurements. The high correlation coefficient between the MR thermometry maps and the thermocouple (r^2 = 0.99) indicates the robustness of the phase difference method for calculating temperature.

6.4.2 Block Design: *In Vivo* Experiment

Diffusion tensor imaging (DTI) was acquired during a warm or 'normal temperature' epoch (12 minutes) while warm (20 °C) methanol was pumped through the cooling probe. This ensured that potential changes in diffusion as measured during the cold epochs could not be merely attributed to changes in methanol flow. Thereafter, we cooled a portion of the primary visual cortex (right hemisphere, lower visual field, 0.7 cm^2 surface) and acquired MR temperature maps until the temperature as measured by the MR-compatible thermocouple beneath the cooling probe reached the desired steady state temperature. We confirmed post-hoc

that a constant supra-dural thermocouple reading correlated with a stabilized intra-cortical PRFST measurement. By altering the flow rate of the methanol during each experiment, we were able to reach a steady-state cortical temperature (~ 40 minutes duration) immediately below the cooling probe of, T_c = 37, 34, 29, 26, 22, 11 (cortical deactivation #1, M1, 9.5 (cortical deactivation #1, M2), and 8 °C (cortical deactivation #2, M1). During the experiments at 21.5 and 20 °C the cortex was near but still above the metabolic cutoff temperature. The experiments at 11, 9.5, and 8 °C represent experiments were the brain was cooled as low as possible without inflicting damage to the dura. During the remainder of the cooling period we kept the cortical temperature constant while DTI images were acquired. Finally, the brain temperature was allowed to recover by pumping through warm ethanol (20 °C), while MR temperature maps were acquired. When the thermocouples revealed a steady-state 'recovered' temperature of 30°C, we acquired three additional DTI images.

6.4.3 ADC Decrease During Cortical Deactivation

Figure 6-3 shows examples of the raw ADC and FA maps acquired during the (1) warm, (2) cold, and (3) recovery conditions of cortical deactivation experiment #2 (M1). Note the difference in ADC maps during the cold condition in the region under the probe when the temperature was 10 °C (white rectangle) (in both cortical tissue and CSF). ADC maps when the temperature under the probe was 21.5 °C are shown in Figure 6-4.

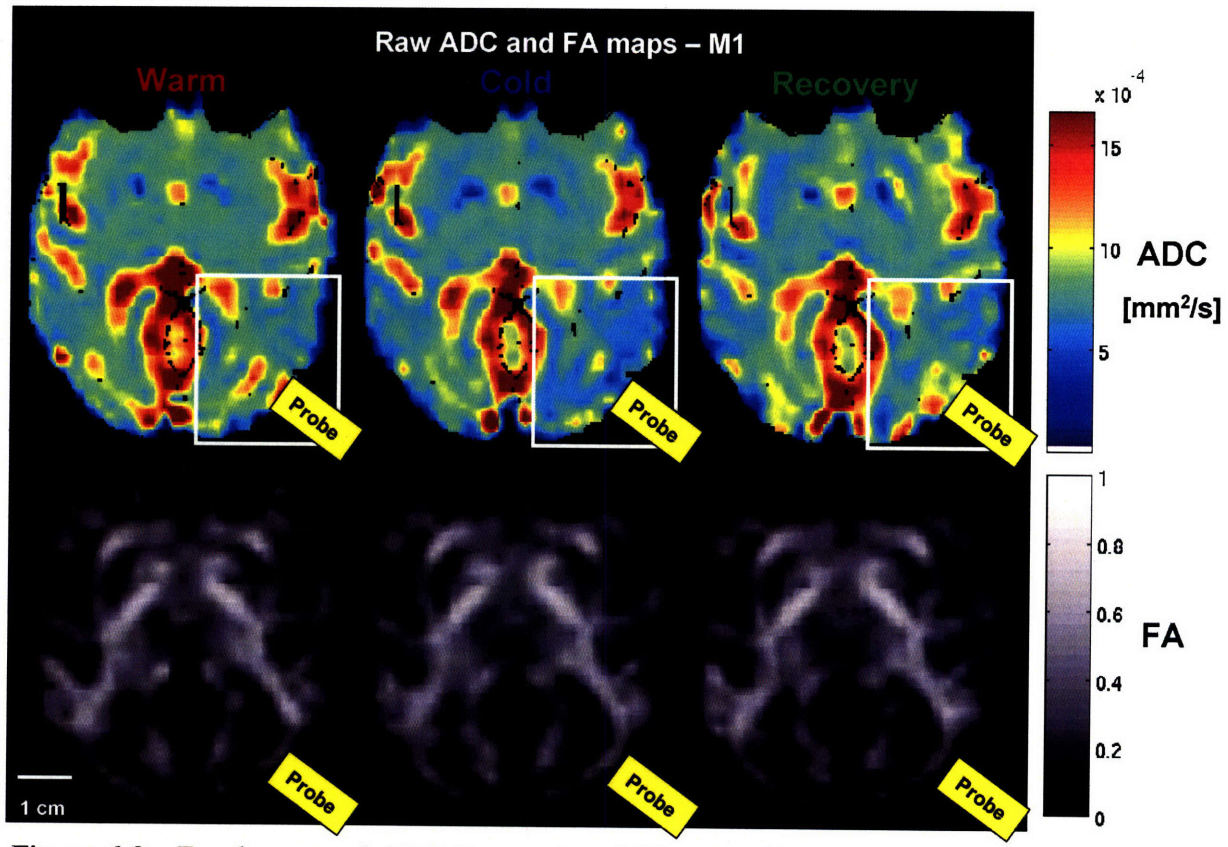

Figure 6-3. Epoch-averaged ADC (top row) and FA maps (bottom row) for the warm, cold, and recovery conditions for an experiment where the temperature under the probe = 8 °C (cortical deactivation #1, M1). The change in ADC is apparent under the probe (white rectangle) during the cold condition, however, no change in the FA is visible.

In order to identify voxels showing a significant change ($p < 0.05$) in ADC and FA between the warm and cooling epochs, nonparametric permutation testing (NPPT) was applied[73].

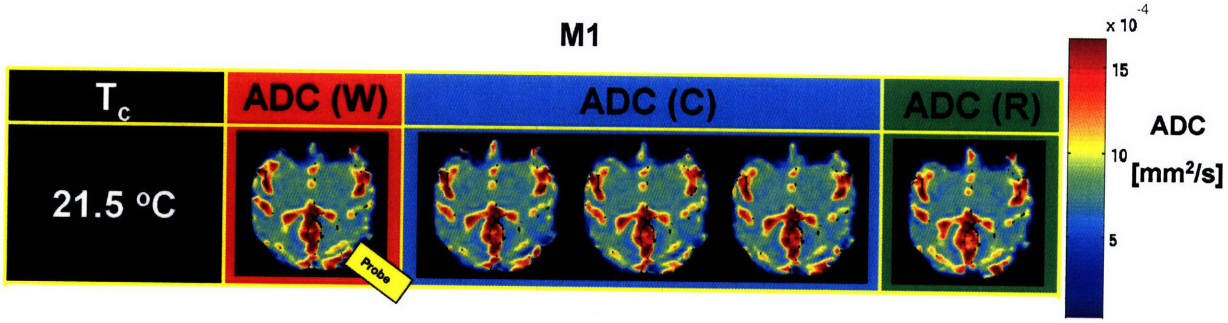

Figure 6-4. ADC maps during warm, cold, and recovery conditions for an experiment with the temperature under the probe, T_c = 21.5 °C as measured by MR thermometry (M1). Only in experiments where there was a significant amount of tissue below the metabolic cutoff of 20 °C were changes in the ADC observed during cooling.

6.4.4 Nonparametric Permutation Testing (NPPT)

The entire volume was used in the NPPT analysis (both ADC and FA). Importantly, NPPT revealed cooling-induced ADC changes only in those experiments where cortical tissue was cooled well below 20 °C – thus not even in these experiments in which the cortical temperature reached 22 °C. Figure 6-5a shows a large region in M1 (3.36 cm^3 brain tissue) where ADC had changed significantly ($p < 0.05$) when $T_c = 11$ °C (cortical deactivation #1, M1).

This result raised the question whether the ADC changes were restricted to these voxels in which the temperature was below 20 °C (i.e., the cortex where metabolic activity was blocked) or whether the ADC changes extended outside the deactivation region. In order to test this, we calculated the 3D-temperature maps using the PRFST-method and overlayed them upon ADC maps. The 20 °C isothermal reveals the region of the cortex where metabolism has been blocked[47,49] (see Figure 6-5b). Figure 6-5b clearly indicates decreased ADC in a substantial region where temperature did not change. Figure 6-6 illustrates largely similar data from a second monkey in which 3.83 cm^3 of brain tissue showed a statistically significant change in ADC (cortical deactivation #1, M2). The amplitude of the observed ADC changes in the region where temperature did not change was similar across both monkeys (see Table 6-1), although the effect was spatially more extended in M1 (40% of the voxels that showed significant ADC changes were > 34 °C) compared to M2 (10% of the voxels).

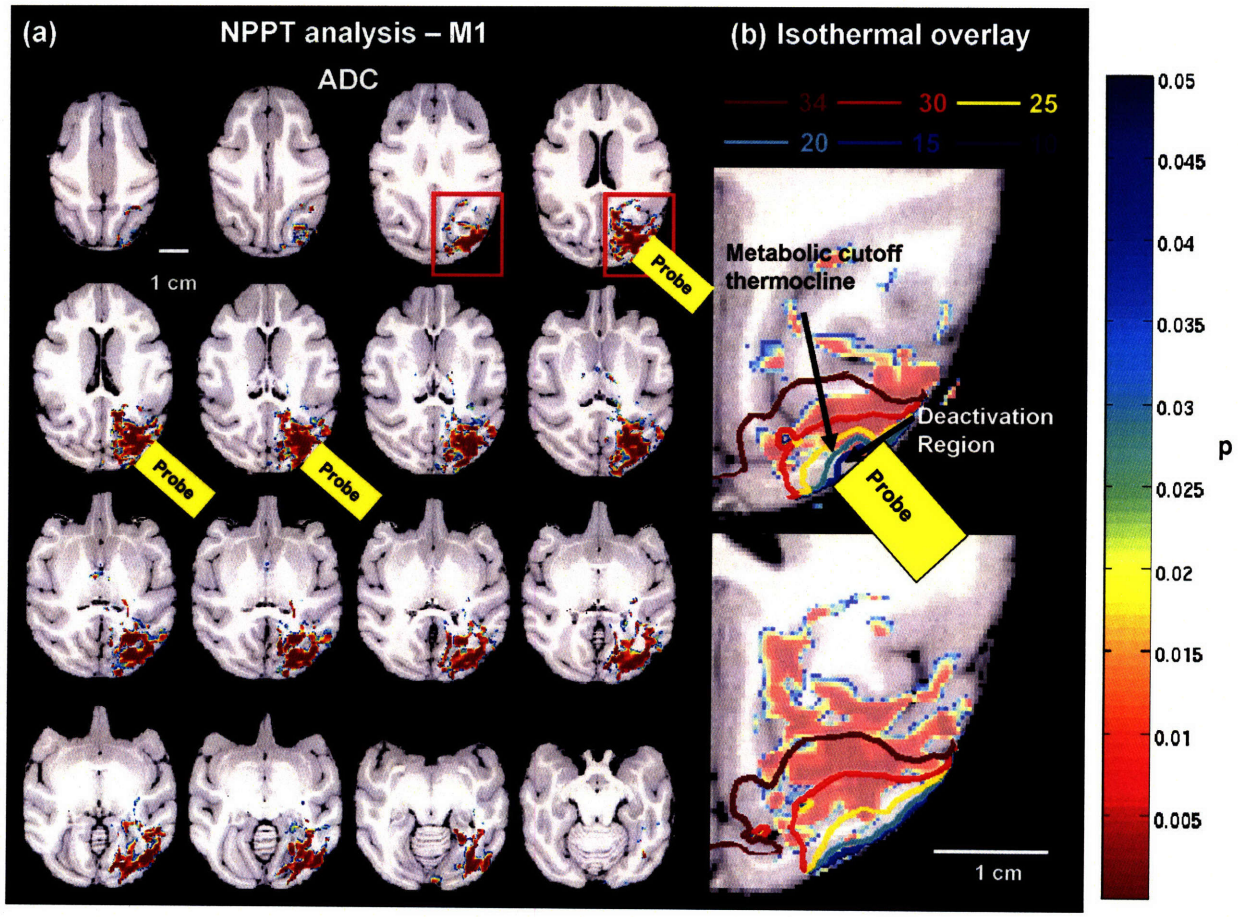

Figure 6-5. (a) Region where ADC changed significantly ($p < 0.05$) between the warm and recovery conditions versus the cold condition as calculated by NPPT (cortical deactivation #1, M1). (b) Isothermals at 34, 30, 20, 15, 10 °C overlaid on the region with significant ADC changes as shown in (a). Note that the statistically significant region extends far beyond the cooled region and is present where the temperature has not changed significantly from the body temperature (T > 34 °C isothermal).

Table 6-1. Percent change in ADC relative to the first warm ADC value for three temperature ranges (> 34 °C, 20-34 °C, < 20 °C) during the warm, cold, and recovery conditions (± SEM). The values in the parenthesis are statistically significant p-values (alpha level = 0.001) from a one sample t-test.

M1						M2					
Gray			White			Gray			White		
ROI 1 (> 34 °C)						ROI 1 (> 34 °C)					
W	C	R	W	C	R	W	C	R	W	C	R
-0.1 ± 0.9	**-18.7 ± 0.6 (6e-6)**	-4.8 ± 0.7	1.1 ± 2.1	**-12.00 ± 0.3 (2e-6)**	2.3 ± 1.7	-0.5 ± 0.8	**-21.2 ± 3.1 (9e-4)**	3.1 ± 3.7	0.5 ± 0.8	**-19.3 ± 2.5 (6e-5)**	6.6 ± 2.4
ROI 2 (20-34 °C)						ROI 2 (20-34 °C)					
W	C	R	W	C	R	W	C	R	W	C	R
0.5 ± 0.5	**-40.9 ± 0.8 (3e-8)**	0.6 ± 2.4	-0.9 ± 2.01	**-37.0 ± 1.1 (4e-7)**	3.8 ± 3.6	-0.9 ± 2.4	**-42.0 ± 1.7 (3e-8)**	-3.2 ± 2.7	-0.7 ± 1.8	**-41.8 ± 1.1 (7e-8)**	-0.2 ± 3.9
ROI 3 (< 20 °C)						ROI 3 (< 20 °C)					
W	C	R	W	C	R	W	C	R	W	C	R

0.5 ± 1.5	**-54.3 ± 1.8 (8e-5)**	-7.1 ± 2.9	1.0 ± 2.8	**-54.6 ± 2.8 (1e-5)**	-14.7 ± 3.0	1.4 ± 3.2	**-67.5 ± 3.0 (1e-8)**	-6.00 ± 2.9	1.3 ± 2.5	**-62.6 ± 2.8 (2e-9)**	-20.7 ± 3.7

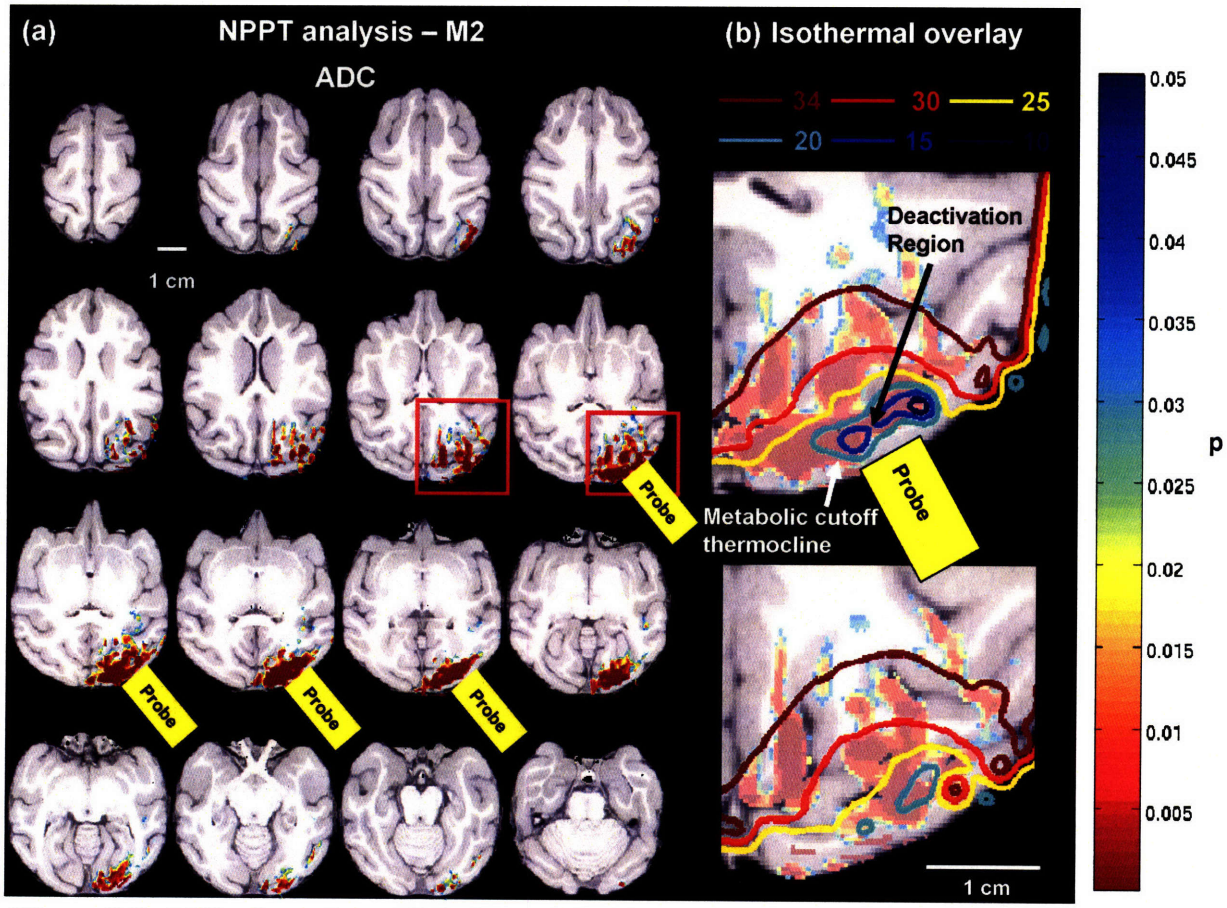

Figure 6-6. (a) Regions where ADC changed significantly ($p < 0.05$) between the (warm + recovery conditions) versus the cold condition as calculated by the NPPT (cortical deactivation #1, M2). (b) Isothermals at 34, 30, 20, 15, 10 °C overlaid on the region with significant ADC changes as shown in (a). Note that the statistically significant region extends beyond the cooled region and is present where the temperature has not changed significantly from the body temperature ($T > 34$ °C isothermal).

6.4.5 ROI Analysis

In order to quantify in detail ADC changes as a function of temperature, we performed an additional ROI analysis on the three experiments in which the cortex was cooled below the critical temperature of 20 °C (i.e. to 11 °C, 9.5 °C, or 8 °C, see Figure 6-5b and Figure 6-6b). Cerebral spinal fluid (CSF) was masked out of all ADC images at a threshold of ADC < 0.0012 mm^2/s. CSF accounted for 7% of the statistically significant region in M1 and 3% in M2.

We first defined three ROIs (ROI 1-3, Figure 6-7, Figure 6-8) which were based on the isothermals measured during the cold epochs, ROI 1-3 encompassed voxels that showed a

significant ADC change and were further subdivided in gray and white matter compartments. ROI 1 included those voxels that showed a significant ADC change but that did *not* change in temperature during the cold epochs (T > 34 °C). ROI 2 and ROI 3 showed significant ADC changes when the temperature during the cooling period was either between 20-34 °C, or between 8-20 °C, respectively.

Figure 6-7 and Figure 6-8 show the results from the ROI analysis within this normal body temperature range in the two monkeys. Note that in ROI 1, cooling resulted in a statistically significant decrease in ADC (12% - 20%, $p < 0.001$, one sample t-test). A first control ROI, cROI 1, was located far from the cooling probe in the anterior left hemisphere and outside the NPPT analysis volume. cROI 2 was positioned closer to the cooling probe than ROI 1, yet it showed no change in ADC. This shows that the observed ADC changes are independent of the distance from the cooling probe and independent from the actual temperature (i.e. some voxels > 34 °C do show a decrease in ADC, others do not).

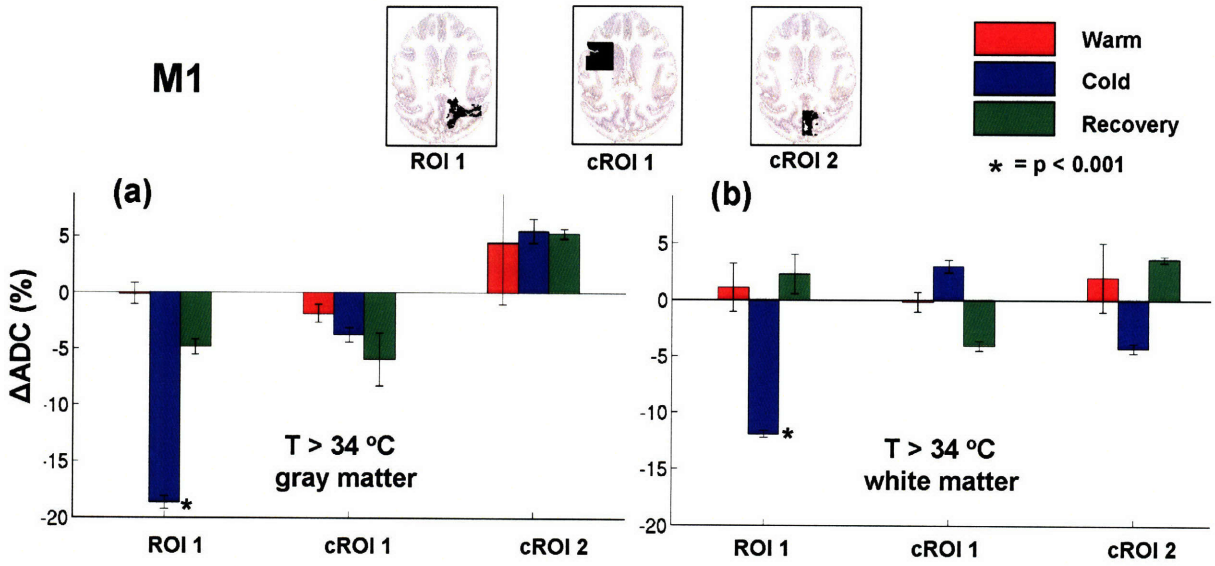

Figure 6-7. ROI analysis of ADC changes (± SEM) during the warm, cold and recovery epochs in M1. Data are plotted for all voxels which showed a significant change in ADC but that did not change in temperature (T > 34 °C) during the cold condition. Panels a and b show data of gray and white-matter voxels respectively. Two control regions where also included. The 1st control region (cROI 1) was chosen to measure the variation of ADC in a region far from cooling (see anatomical inset). The 2nd control region (cROI 2) is closer to the probe as ROI 1 but shows no change in ADC. This indicates that the change in ADC is not a function of temperature, nor of distance from the probe.

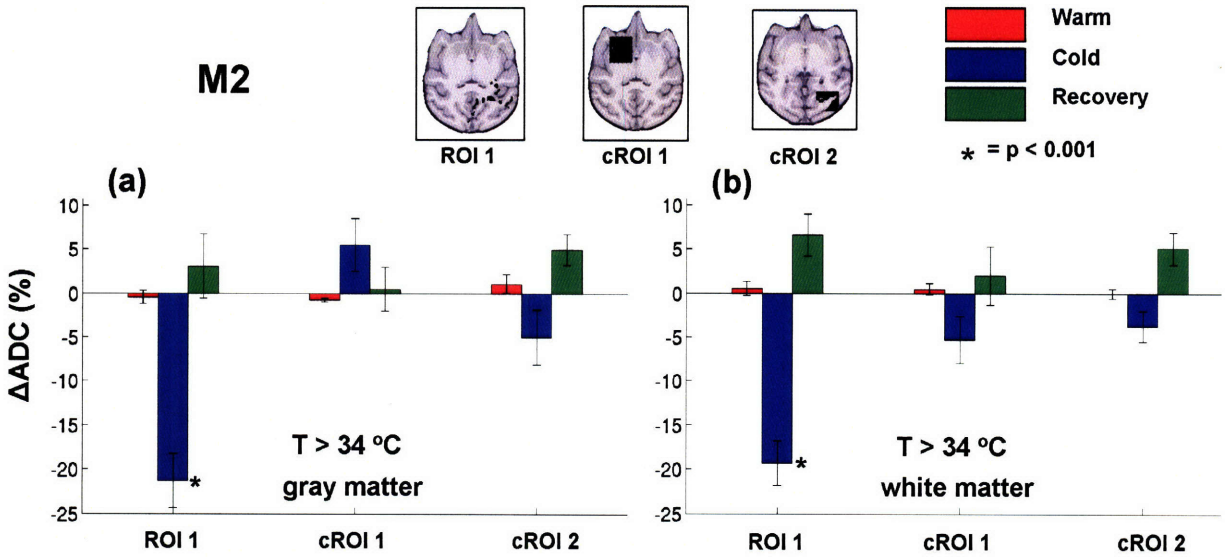

Figure 6-8. ROI analysis of ADC changes (± SEM) during the warm, cold and recovery epochs in M2. Same conventions as in Figure 6-7.

The ADC values from ROI 1 (where temperature did not change) during the warm, cold, and recovery conditions are also shown in Figure 6-9 for comparison with the ADC values in those compartments that changed in temperature during the cold epochs (ROI 2 and 3). We normalized the data relative to the first warm ADC value (see also Table 6-1). The red, blue and green symbols indicate the ADC values during the warm, cold and recovery epochs, respectively. As can be observed, significant changes in ADC are present in ROI 2 and 3. However, unlike the ADC changes observed during the cold epoch in ROI 1, we cannot be entirely conclusive as to what fraction of the ADC changes in ROI 2 and 3 is due to cerebral glucose metabolism and what fraction is due to temperature. Note that we were able to cool cortex below the metabolic cutoff temperature of 20 °C only in a relatively small region (0.2 cm^3 voxels in M1 and 0.4 cm^3 in M2, see Figure 6-5 and Figure 6-6).

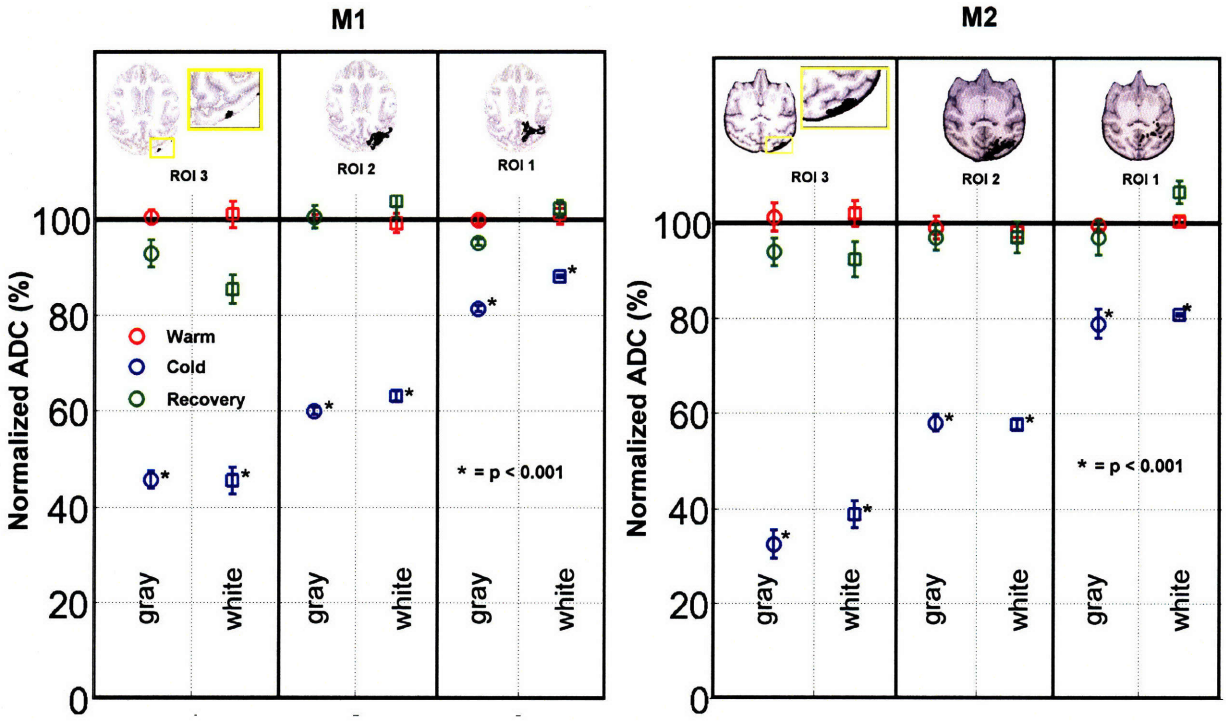

Figure 6-9. (Left) Plot of the mean normalized ADC (± SEM) in M1 for gray matter and white matter voxels in the three temperature ranges: T > 34 °C (ROI 1), 20-34 °C (ROI 2), 8-20 °C (ROI 3). Red, blue, and green values indicate the normalized ADC during the warm, cold, and recovery conditions respectively. (Right) Plot of the mean normalized ADC (± SEM) in M2.

Using the data from the nine reversible deactivation experiments, we were able to calculate the ADC as a function of temperature and compare it to the diffusion of free water[74]. The deactivation region from M1 and M2 (ROI 1, T < 20 °C) was used to define an ROI to calculate the ADC as a function of temperature for the reversible deactivation experiments. Figure 6-10 plots the *in vivo* ADC as a function of temperature relative the diffusion of free water. The *in vivo* ADC follows the same trend as the diffusion of free water above the metabolic cutoff, but shows a decrease (~ 20%) relative to the diffusion of free water below the metabolic cutoff.

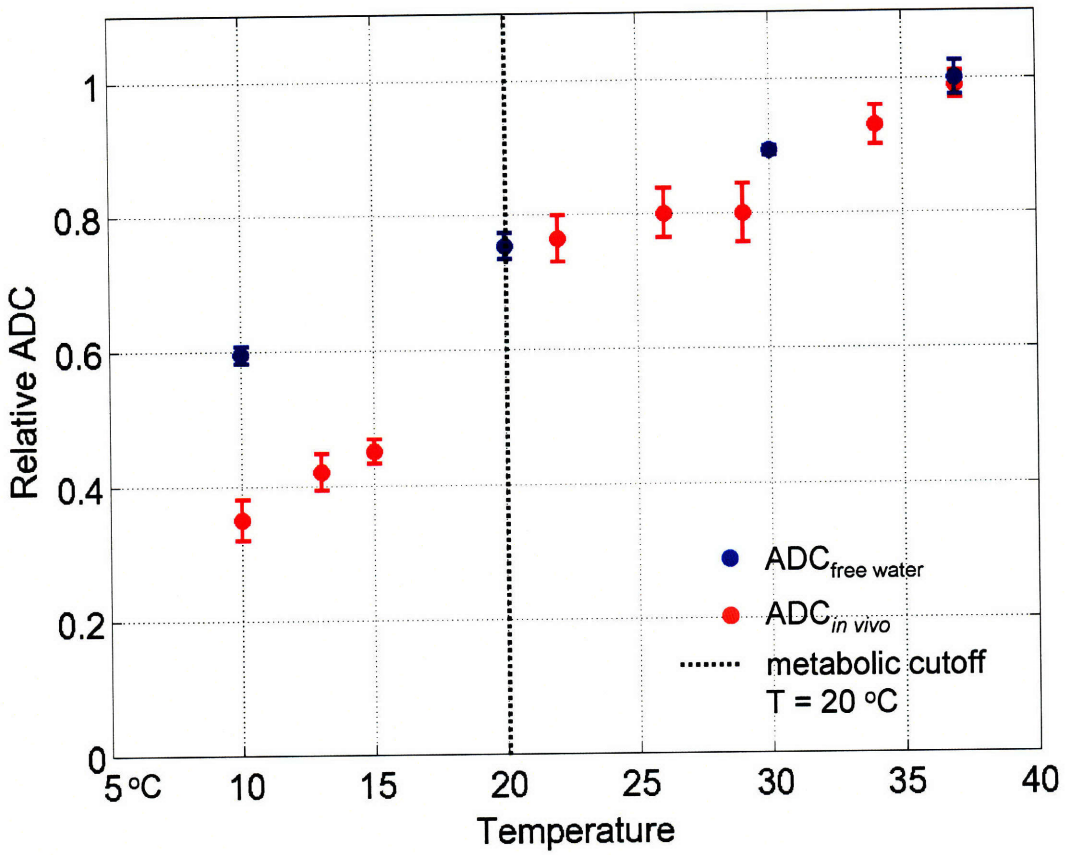

Figure 6-10. The *in vivo* ADC ($ADC_{in\ vivo}$, red) and the ADC of free water ($ADC_{free\ water}$, red) plotted as a function of temperature from the nine reversible deactivation experiments. The deactivation region, T < 20 °C, from M1 and M2 was used to define an ROI to compare the ADC between the nine reversible deactivation experiments. Note the $ADC_{in\ vivo}$ follows the diffusion of free water for T > 20 °C, but not below the metabolic cutoff.

6.4.6 FA Shows No Change During Metabolic Deactivation

Using NPPT, we compared the FA maps between all combinations of the warm, cold, and recovery conditions. In addition, we compared the FA values in ROI 1, 2, and 3 between the warm, cold, and recovery conditions. These analyses revealed no changes in the FA maps in either of the two monkeys.

6.5 Discussion

The effect of cerebral glucose metabolism on the ADC and FA

Reversible deactivation of cerebral glucose metabolism by cortical cooling resulted in ADC decreases of 12-20% in regions far from the deactivation site where the temperature did not change. Nowhere in the brain were changes in FA observed using NPPT or ROI-based statistics.

The decrease in ADC at distant sites induced by cooling can be explained by the effect that cooling has on cerebral glucose metabolism. Cooling blocks deoxyglucose uptake in neurons that are at a temperature below 20 °C[75-77]. Moreover, cortical cooling has a profound functional effect at distant sites receiving anatomical projections from the deactivated region[50,75]. In addition, reversible deactivation cooling studies in combination with electrophysiology indicated that action potentials cannot be generated below 20 °C, hence cooling also blocks neuronal activity[47].

In the present study, changes in ADC were revealed only during those cooling experiments where the cortical temperature under the cooling probe was below the metabolic cutoff of 20 °C and not in those experiments where the cortical temperature reached 22 °C. Moreover, the extent of ADC changes in those experiments went far beyond the cooling region, extending into areas in which temperature had not changed (20% decreased ADC in gray matter and 12% in white matter, Figure 6-7). These results indicate that the changes in ADC are not due to the effect of temperature on diffusion alone and are due to deactivation of cerebral metabolism. Moreover, voxels in a control ROI (cROI 2 of Figure 6-7) closer to the cooling probe than ROI 1, did not show significant changes in ADC. These results suggest that changes in ADC can be observed in sites not directly affected by temperature, which are most likely anatomically connected to the cortical region that was cooled below 20 °C. Also, comparison of the *in vivo* ADC as a function of temperature to that of free water shows a marked change in the behavior of the *in vivo* ADC below the metabolic cutoff (Figure 6-10).

The next question is then, which biophysical mechanisms dependent on cerebral metabolism could be responsible for such ADC changes?

One possible mechanism could be fast axonal transport (cytosolic streaming)[56]. Fast axonal transport of proteins and vesicles is induced by the motion of the microfilaments and microtubuli[78] and is regulated by ATP[79]. Local anoxia (cold-block) experiments showed inhibition of fast axonal transport by affecting oxidative metabolism responsible for ATP production[80-83]. It is possible that the reversible deactivation of cerebral glucose metabolism by cooling affected the diffusion of water by inhibiting the fast axonal transport throughout the axon (cytosolic streaming[72]). The diffusion coefficient of water arising from fast axonal transport can be calculated by assuming a parabolic velocity profile of water in the axon with no flow on the boundary of the axon and a maximum velocity, v_{max}, in the center of the axon. The range of v_{max}

can be approximated by the velocity range of the fast axonal transport of proteins, $v_{max} = 1 - 10$ μm/s[84-87]. The range of diffusion coefficients resulting from this parabolic flow profile would be $2.5 < D < 250$ μm^2/ms which is in the range of diffusion coefficients, $D \cong 0.1-10$ μm^2/ms, measured in the brain.

Another possible mechanism which could explain the ADC decrease at distant sites from cooling is cellular swelling associated with axon deploarization[55]. As local deactivation of cerebral glucose metabolism has been shown to affect action potential generation at distant sites[75], changes in the electric potential of axons and neurons at distant sites may affect the diffusion of water in the intracellular and extracellular space.

Cellular swelling associated with temperature may also explain the ADC decrease observed in this experiment. Cooling may shrink the neuron and result in a shrinking of the axon which would decrease the ADC while not affecting the FA.

ADC decreases observed during this experiment (12-20%) could partially explain the marked decrease in ADC during ischemia (20% to 50%) and post-mortem studies (~ 40%)[35]. FA changes were not expected to change in this experiment because of the short deactivation period (~40 minutes). FA changes in stroke and lesion studies have been shown to occur over a long time period (hours to days) and may be related to other neural processes like Wallerian degeneration[60].

Future Work

The results from this experiment suggest testing directly the affect of fast axonal transport and action potential blockers on the diffusion of water *in vivo*. Also, reversible deactivation in conjunction with MR-spectroscopy could measure which metabolites are suppressed during deactivation to more accurately quantify the effects of cooling on cerebral glucose metabolism. The MR-compatible RD cooling system can also be used to explore functional interactions between anatomically connected regions. The fast deactivation capabilities of the cooling system (~4 min) makes it ideal for awake monkey fMRI studies[3,4,88] in which regions can be deactivated and re-activated many times within a typical scan session (§6).

6.6 Conclusion

In summary, we presented a novel method to deactivate cerebral glucose metabolism in an MR-compatible, focal, and reversible manner. Combined with *in vivo* 3D thermometry measurements with an accuracy of ± 1 °C, the present experiments indicated that reversible short-term deactivation of the cortex resulted in a significant decrease in ADC at distant sites from cooling but has no measurable effect on FA. In our study we used MR temperature maps to show that ADC changes occurred even where there was no change in temperature. These data suggest that a relatively large fraction of the ADC changes (12-20%) observed during pathology may depend on process associated with cerebral glucose metabolism. The *in vivo* ADC as a function of temperature was measured and showed a marked change in its behavior below the metabolic cutoff of 20 °C.

§7 Reversible Deactivation of V1 During Awake Monkey fMRI

7.1 Introduction

Data from reversible deactivation experiments provides information that fills an important gap to assess neural assemblies. When a region in the brain is cooled below 20 °C, termed the 'metabolic cutoff', it looses functionality since the neurons cannot generate action potentials necessary to transmit information to other neurons at this temperature[47]. Using this method one can investigate whether a brain region is activated during a particular task and plasticity effects: i.e. other brain regions might take over (partially) the functions normally carried out by the deactivated region, as is seen in patients after strokes. Reversible deactivation studies have been done with cats and monkeys but not with dynamic imaging techniques that yield detailed functional information throughout the brain. In other combined functional-imaging/reversible deactivation studies, the animal needed to be sacrificed [47,75]. More recently, optical imaging studies have been done in combination with electrophysiology while regions of the visual cortex have been deactivated [89]. It is more advantageous to perform reversible deactivation experiments in combination with fMRI since the monkey could be kept alive and the brain could be deactivated multiple times allowing many paradigms to be studied in the same animal.

Other reversible deactivation methods exist besides cortical cooling. Reversible deactivation with a variety of pharmacological and chemical agents has been used in conjunction with electrophysiological assays of neural function [90-92]. Procedures have been described using pressure injection of the chemical GABA (gamma-amino butyric acid) to reversibly deactivate sites in the cerebral cortex [93]. The disadvantage of using chemical agents to reversibly deactivate cortex is two fold: (1) drug deactivation is on the order of hours, and (2) due to the low sensitivity of MR spectroscopy (10^{-5}) compared to conventional MRI, it would be difficult to accurately define the deactivation region. Also a limited number of drug injections can be performed before the brain damage occurs.

In this section we present a MR-compatible cortical cooling system capable of reversibly deactivating cerebral glucose metabolism (hence neural activity) in conjunction with fMRI studies. The deactivation region was defined with MR-temperature maps calculated from *in vivo* MR-thermometry. The MR-compatible cortical cooling system can be used to measure the

functional consequences throughout the brain of reversibly deactivating a particular node of a functional visual network.

7.2 Background

The major advantage of fMRI is that it is a completely non-invasive technique that can be used to study functional properties of healthy and diseased human subjects[94-96]. This greatly simplifies the experimental procedure and allows multiple experiments to be performed on a single subject. fMRI also possesses higher temporal and spatial resolution than other neuroimaging techniques (i.e. PET). The fMRI signal measures the hemodynamic response to stimuli (visual, motor, etc.) and is based on the increase in blood flow, blood volume, and the cerebral metabolic rate of O_2 to the local vasculature. The flow of blood results in a local reduction in deoxyhemoglobin[97-100]. The decrease in deoxyhemoglobin, a paramagnetic molecule, increases the MRI signal during the hemodynamic response.

fMRI studies suffer from a number of criticisms; (1) the hemodynamic response is an indirect measure of neural activity, (2) the hemodynamic response is more associated with presynaptic activity and less so with spiking output[101], and (3) fMRI activation maps describe 'where' activation occurs but reveal nothing about neuronal mechanisms. Virtually of these criticisms stem from the complex relationship between the generation of the action potential and the hemodynamic response[102]. By developing a MR-compatible method to reversibly deactivate cerebral glucose metabolism, the effect of cerebral glucose metabolism on the hemodynamic response could be explored. Reversible deactivation of cerebral glucose metabolism has been shown to inhibit action potential generation[47]. Therefore reversible deactivation of cerebral glucose metabolism would affect the electrical input of regions functionally connected to the deactivation region. RD does not alter the input in the deactivated region but does abolish the output. Therefore, you can investigate the differential impact of input and output on the fMRI signal. Also, reversible deactivation of functional cortex would provide valuable information on the plasticity and functional hierarchy of the neural network.

So far, neuroscientists have focused mainly on 'mapping' questions (revealing valuable modern 'phrenological' information). However, besides knowing which brain areas are involved in the processing of a particular stimulus, or task, it is more important to know how brain regions interact with each other. In other words: what kind of calculations are performed in one area and

what kind of information is transmitted to the other areas. One tool to investigate the interactions between brain regions is to disable a small region in the brain and look at the functional consequences of this (reversible) deactivation upon regions anatomically connected to the inactivated site [47,48,75].

7.3 Materials and Methods

7.3.1 Animal Preparation

All procedures were approved by MGH's Subcommittee on Research Animal Care (Protocol #2003N000338) and MIT's Committee on Animal Care, and are in accordance with NIH guidelines for the care and use of laboratory animals. One male rhesus monkeys (Macaca mulatta; 4.3 kg, 4 years old) was prepared for fMRI as previously described and trained for a passive fixation task (full-field checkerboard stimuli) [26]. After the monkey mastered the task, a 0.75 inch diameter recording well (Crist Instruments, Washington, DC) was placed over V1 of the right hemisphere. The recording well exposed the dura and was sealed with a cap when the monkey was not in the scanner. The data were acquired on a Siemens Trio 3T MRI scanner located at the Athinoula A. Martinos Center for Biomedical Imaging, Massachusetts General Hospital (Charlestown, Massachusetts).

7.3.2 RD Cooling System

A portion of the primary visual cortex in the right hemisphere was deactivated by placing an MR-compatible coolant probe on the surface of the dura above V1 (see Figure 5-1). The probe was made from G10/FR4 (fiberglass). A fiber optic thermocouple (00-11874-01, Luxtron Corp.) was placed directly under the cryo-surface of the cooling probe. The thermocouple touched the dura during the experiment and yielded a real time measure of the cortical surface temperature. Methanol (reagent grade anhydrogenous, S75965, Fisher Scientific) was passed through the probe with a pump (QV pump, Q3 pump head, FMI Pump). Teflon tubing (1667xl, Upchurch Scientific) was used to transfer the methanol from the pump and ferrules and nuts (P-343 ferrule, P-331 nut, Upchurch Scientific) were used to secure the tubing to the pump and coolant probe.

7.3.3 Reversible Deactivation

Two cortical cooling profiles were chosen. The first cooling profile was 3 min warm methanol flow – 5 min cold methanol flow – 3 min warm methanol flow (RD 1). A second cooling profile was used with multiple reversible deactivations in the same scan; 1 min warm – 2.5 min cold – 3.5 min warm – 3 min cold – 2 min cold (RD 2).

7.3.4 Functional MRI Acquisition

Functional images were acquired with a gradient-echo T2*-weighted EPI sequence (40 horizontal slices, 64 x 56 matrix, TR = 3 s, TE = 24 ms) during cortical cooling. A saddle-shaped, radial transmit-receive surface coil (12 cm diameter) was employed.

7.3.5 Thermocouple Measurements

Using a Luxtron 3100 Fluoroptic Thermometer (Luxtron Corp.), the thermocouples values were read and stored at 4 Hz throughout the entire fMRI experiment. The thermocouple readings were applied in the analysis of the data as a regressor of interest for RD 2 and were also used during the experiment to approximate the temperature of the deactivation region and to ensure the dura and cortex did not freeze. We ensured that the temperature of the dura was not below 2° C. Thermocouple measurements from Experiment 2 are shown in Figure 7-1. The correlation coefficient, r^2, was always > 0.98.

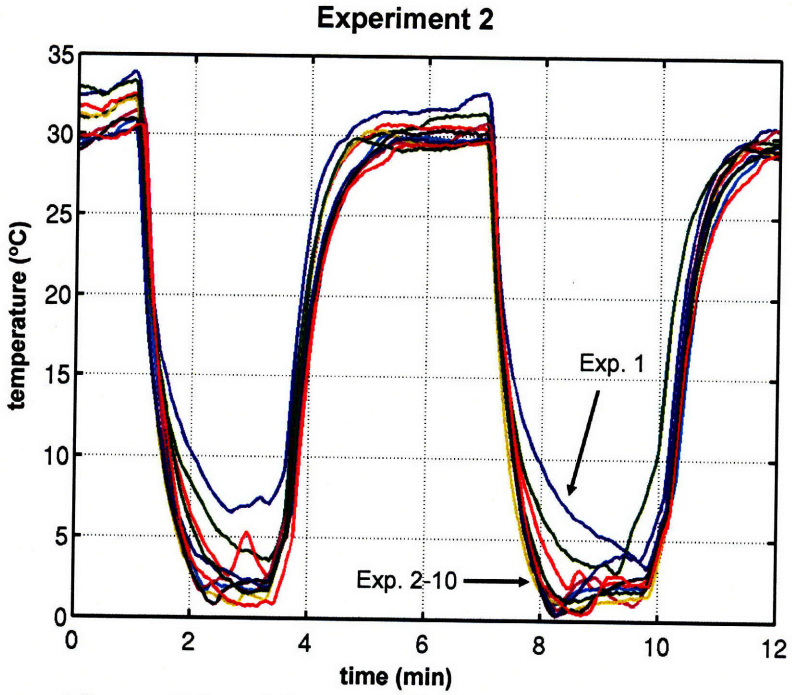

Figure 7-1. Thermocouple data from 10 reversible deactivation fMRI scans during Experiment 2. The cooling profile was 1 min warm – 2.5 min cold – 3.5 min warm – 3 min cold – 2 min warm. The consistency of the cooling profile is illustrated over Exp. 2-10. The first deactivation (Exp. 1, blue line) is warmer than subsequent deactivations because it is always more difficult to cool the brain in the first deactivation cycle.

7.3.6 Anatomical MRI Acquisition

High resolution T1 images were acquired under ketamine-xylazine anesthesia in a separate session with an MPRAGE sequence [19] with TR/TI/TE = 2500/1100/4 ms, $\alpha = 8^{o}$, 0.35 mm isotropic resolution, total acquisition time: 16 min, Siemens Trio. Eight T1 images were acquired with this sequence and reconstructed (motion corrected, averaged, and normalized) using Freesurfer, http://surfer.nmr.mgh.harvard.edu. A single radial transmit-receive surface coil (12.5 cm diameter) was employed.

7.3.7 MR-defined Temperature Maps

MR thermometry imaging employed single shot multi-slice EPI with an isotropic resolution of 1.5 mm. The MR-temperature maps were acquired under ketamine-xylazine anesthesia in a separate session using the same cooling profile in the functional experiments and registered to the high resolution anatomical image.

Twenty-five axial slices were acquired using TR/TE = 4000/19 ms, 128 mm FOV, and a 90° flip angle, at 1.5 mm isotropic resolution. Magnitude and phase images were acquired. Temperature maps were calculated from the MR thermometry scans using the proton resonance frequency shift thermometry (PRFST) method, Eq. (4.2), which relates the temperature change to the difference in phase between successive time points [2,62,63].

7.3.8 Statistical Analysis

A voxel-based analysis was performed using SPM99 (Wellcome Trust Centre for Neuroimaging, UCL), following previously described procedures to fit a general linear model (GLM)[26-29]. A block design was used with four epochs; warm fix, warm stim, cold fix, and cold stim. t-score maps from both monkeys were thresholded and overlaid on functional EPI images. Activity profiles were sampled using custom extensions to SPM99. Images were motion-corrected within a session and non-rigidly co-registered to each other using Match software[36]. After sub-sampling to 1 mm^3 isotropic voxels, functional and temperature images were smoothed (Gaussian kernel, $\sigma = 0.67$ mm) and co-registered using Match. Global scaling, high- and low-pass filtering were employed prior to fitting the GLM[26,29]. To account for head and eye movement-related activity, covariates of no-interest from the motion realignment parameters and eye traces were used. Eye traces were thresholded, convolved with the BOLD hemodynamic response function, and sub-sampled to the TR.

7.3.9 Activity Profiles

Percent MRI signal changes were calculated using SPM99 by taking a mean over the local t-score voxel and 2-3 bordering supra-threshold voxels. Percent signal changes, ΔS (%), were also sampled along line-plots parallel to the cortical surface.

7.3.10 Visualization

t-score maps from both monkeys were thresholded (see figure legends for the thresholds used) and overlaid on T1-weighed anatomical images, which were reconstructed with FreeSurfer[30,31]. A flattened surface of the ipsilateral hemisphere was generated in Caret. Classification was done in Caret, using our retinotopic mapping (white / black dashed lines

indicate vertical / horizontal meridians) for early visual areas and Caret stored libraries for higher visual areas, and ordered based on Felleman and Van Essen's scheme[39].

7.4 Results

7.4.1 Deactivation Region

The deactivated region (T < 20 °C) calculated from MR temperature maps was overlaid on inflated and flattened maps using Caret software. The deactivation region show in Figure 7-2 was the same for Experiments 1 and 2 and was achieved by reaching an average thermocouple value of ~2.5 °C on the dura (corresponding to a cortical temperature of ~10 °C). The deactivated region is 0.4 cm^3 (0.8 mm^2 surface area).

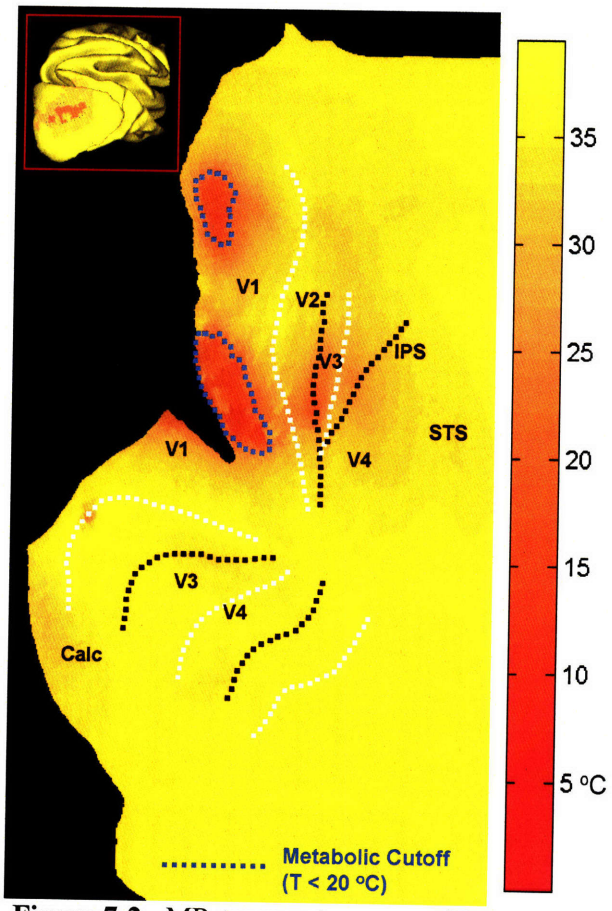

Figure 7-2. MR-temperature maps (T < 20 °C) overlayed on the inflated (inset) and ipsilateral hemisphere flat map.

The temperature maps show that not only did we deactivate parafoveal V1 (on the operculum) but also more peripheral V1 representations in the calcarine sulcus (the 1st sulcus

located immediately below the cortical surface). In the future, the amount of cooling can be decreased to only deactivate the cortical surface.

7.4.2 BOLD fMRI Response in the Warm and Cold Conditions

The BOLD hemodynamic response generally decreased during the cold epoch compared to the warm condition. Figure 7-3 shows the t-score maps comparing the visual stimuli epoch to the fixation epoch for the warm (left) and cold (right) conditions.

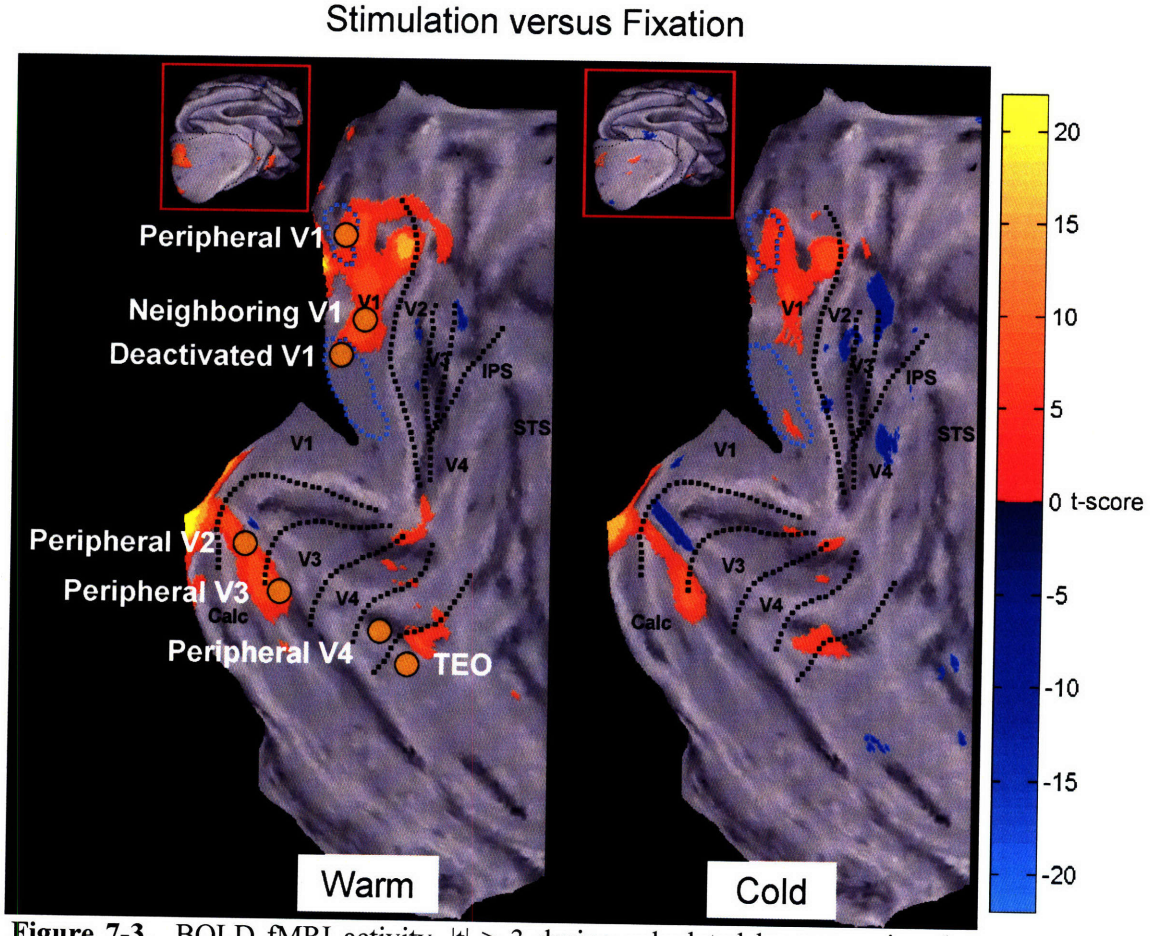

Figure 7-3. BOLD fMRI activity, $|t| > 3$ during calculated by comparing the visual stimuli epoch versus the fixation epoch for the (left) warm, W, and, (right) cold, C, conditions (Experiment 2). The deactivation region is enclosed by the dotted blue line. The hemodynamic response in the seven regions (brown dots) was compared in the ipsilateral and contralateral hemispheres (Figure 7-4, Figure 7-5).

The activity maps in Figure 7-3 do not show as much activity as one would expect from a full-field stimulus because of susceptibility distortions present near the probe. Nonetheless, note the clear reduction of fMRI activity during the cold epoch.

Eight regions were chosen in the ipsilateral and contralateral hemispheres to compare the BOLD hemodynamic response during the warm and cold epochs; deactivated V1 (DV1), V1 surrounding the deactivation region (termed 'Neighboring V1', NV1), parafoveal lower quadrant V1 (termed 'peripheral V1', PV1) , PV2, PV3, PV4, LGN, and TEO. Figure 7-4 and Figure 7-5 present bar plots of the BOLD fMRI activity (visual stimulation – fixation) between the warm (red) and cold (blue) epochs in the ipsilateral and contralateral hemisphere during Experiment 1 and 2 respectively. Notice that in neighboring V1 (both hemispheres) and TEO in the ipsilateral hemisphere, there is a boost in the BOLD fMRI response during the cold epoch. This suggests the activation of immediate compensatory mechanisms. The effect of deactivation on ipsilateral LGN implies the long-range functional implications of RD: both in areas connected through feedback (LGN) and feedforward connections (TEO).

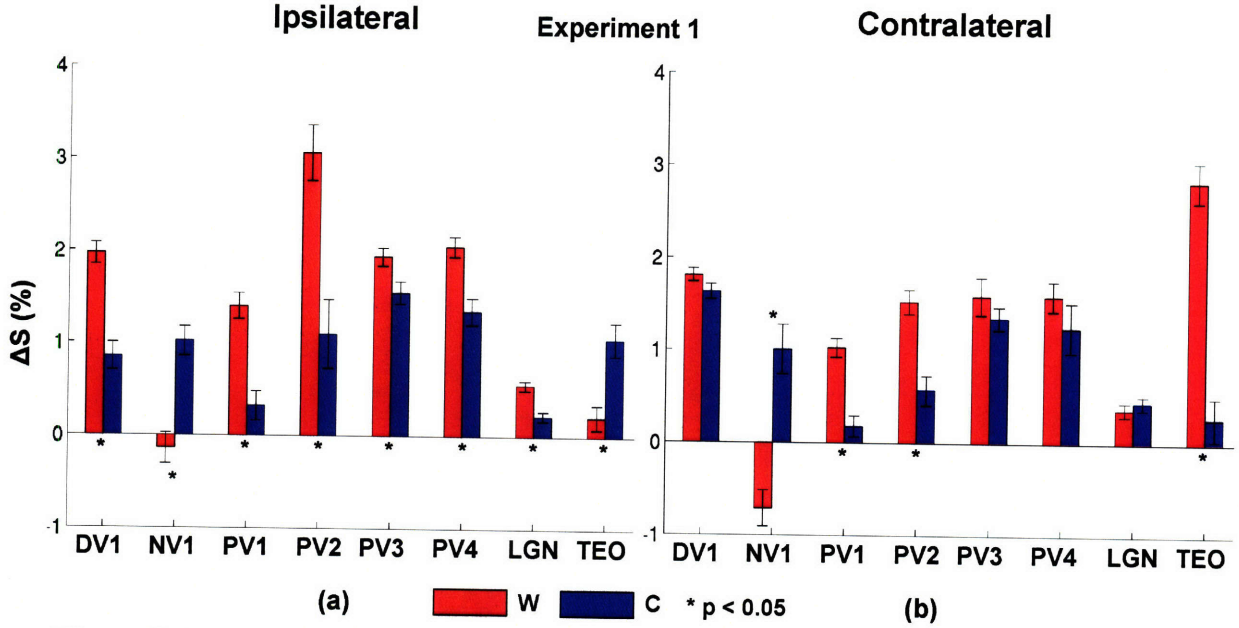

Figure 7-4. BOLD fMRI activity compared in deactivated V1 (DV1), neighboring V1 (NV1), peripheral V1 (PV1), PV2, PV3, PV4, LGN, and TEO in the (a) ipsilateral and (b) contralateral hemispheres during Experiment 1. Neighboring V1 was not visually driven during the warm condition but visually driven during the cold condition. The effects of reversible deactivation are seen in both hemispheres.

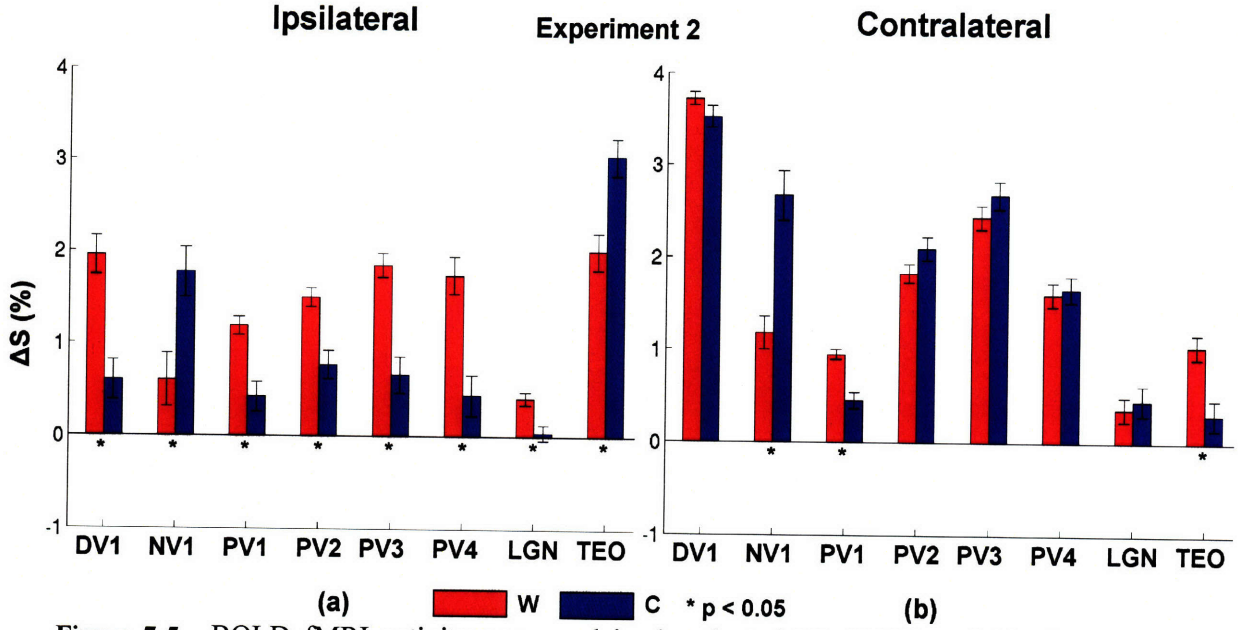

Figure 7-5. BOLD fMRI activity compared in deactivated V1 (DV1), neighboring V1 (NV1), peripheral V1 (PV1), LGN, and TEO in the (a) ipsilateral and (b) contralateral hemispheres during Experiment 2. Same conventions as Figure 7-4. There was a larger hemodynamic response across the brain during Experiment 2. However, the same general trends in the hemodynamic response during the warm and cold conditions are seen in Experiments 1 and 2.

7.4.3 MRI Signal Correlates with the Metabolic Activity of the Deactivated Region

By comparing the MRI signal between the warm and cold conditions, we can calculate how the baseline MRI signal correlates with the metabolic activity of the deactivated region. Figure 7-6 presents t-score maps that correlate positively and negatively with the thermocouple profile during Experiment 2. The regions that positively and negatively correlate with the metabolic activity of the deactivated region are located in the ipsilateral and contralateral hemisphere.

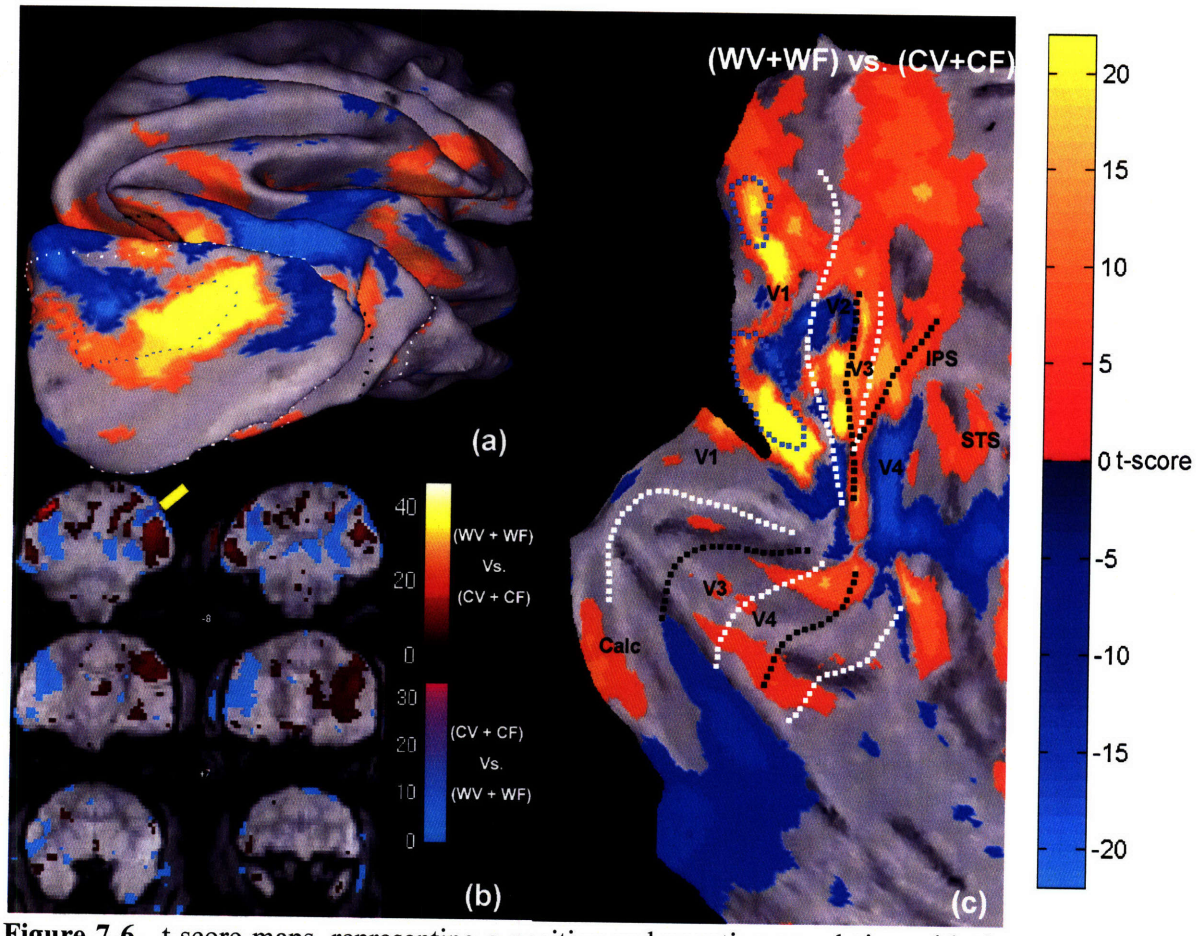

Figure 7-6. t-score maps, representing a positive and negative correlation with the metabolism of the deactivated region. (a) Inflated ipsilateral hemisphere, (b) functional maps, and (c) flat map of ipsilateral hemisphere,. The maps where thresholded for $|t| > 3$. Positive and negative correlations are seen in both hemispheres in visually and non-visually driven regions. In (b) the location of the probe is denoted by the yellow rectangles.

How does the relationship between temperature and the MRI signal affect the interpretation of the results from Figure 7-6 in the deactivation region. Decreasing the temperature has the effect of increasing T2*, and thus increases the MR signal. However, in Figure 7-6 we see that the MRI signal is higher during the warm condition than the cold condition in the deactivated region despite the effect of temperature on the MRI signal.

7.5 Discussion

fMRI combined with the cortical cooling system has the capability to study the immediate compensatory mechanisms of the brain after a particular region is deactivated. Reversible deactivation by cortical cooling in conjunction with MR-temperature maps, represents the first reversible deactivation technique capable of quantifying the degree and extent

of the deactivation region *in vivo* and non-invasively (Figure 7-2) [48]. Reversible deactivation decreased activity at the site of deactivation and regions connected to it via feedback connections (e.g. V1) and feedforward connections (e.g. TEO). Surprisingly, fast compensatory mechanisms seem to be activated in the regions immediately surrounding the deactivated region. It remains an open question whether these hemodynamic signal changes reflect neuronal signal changes. We believe that this may very well be the case since we observed also strong compensatory signal changes in areas at a long distance from V1 where temperature did not change (e.g. LGN, and TEO) (Figure 7-3, Figure 7-4, Figure 7-5).

The increase of the hemodynamic response in the visual system (ipsilateral and contralateral neighboring V1, ipsilateral TEO) during the cold epoch, indicates the inherent compensatory mechanisms in the brain. The results from this experiment suggest that the brain does not need to be permanently damaged before functional reorganization (plasticity) takes place. In other words, the plasticity of the visual system could be 'hardwired' into the functional network and is activated within minutes.

Positive and negative correlations between metabolic activity (cortical temperature) and the MRI signal in the ipsilateral and contralateral hemispheres were also observed (Figure 7-6). Interpretation of these results remains difficult since we don't know if the change in the baseline MRI signal reflects a change in neural metabolism or is a physiological response to the cooling.

Future Work

In future reversible deactivation fMRI experiments with cortical cooling, it would be desirable to design a custom phased array coil (as described in §7) to optimize the resolution and minimize EPI distortions in the functional images. This would greatly aid in image registration with anatomical images. Also, future experiments will employ a feedback system to control the cortical temperature to allow a variety of different cortical cooling profiles. Future reversible deactivation fMRI studies could employ multiple deactivation sites. In addition, combining reversible deactivation with fluorodeoxyglucose positron emission tomography (FDG PET) could confirm changes in baseline metabolic activity during the reversible deactivation of V1 [103-106].

7.6 Conclusion

We present a MR-compatible cortical cooling system capable of reversibly deactivating cerebral glucose metabolism (hence neural activity) in conjunction with awake monkey fMRI studies. The deactivation region (0.4 cm^3) was defined with MR-temperature maps calculated from *in vivo* MR-thermometry. Until now, the deactivation region has never been measured *in vivo* with any reversible deactivation method. Reversible deactivation of V1 decreased the hemodynamic response in V1 in both hemispheres and regions receiving feedback and feedforward from V1. Compensatory effects were observed in V1 (neighboring the deactivation region) in both hemispheres, and ipsilateral TEO with in 2 minutes of deactivation. Positive and negative correlations between metabolic activity in V1 and the MRI signal in visually and non-visually driven structures were also observed. Future FDG-PET experiments can be performed to determine if visually and non-visually driven structures require electrical input from the visual system to remain metabolically active.

§8 Conclusions

8.1 Summary

In this thesis, a 4-channel 3 Tesla phased array coil was developed to improve the SNR and EPI distortions of diffusion MRI and fMRI (§2). The phased array coil improved the resolution of functional EPI images by a factor of 2 and diffusion images from 1.5 mm to 0.9 mm isotropic (volumetric factor of 4). I developed a general framework, termed multiple wavevector fusion (MWF), to resolve white matter architecture by combining information from different diffusion wavevectors (§4). The MWF methods improves the sampling efficiency of the diffusion acquisition by 274-377%. In addition, I have developed a MR-compatible cortical cooling system capable of reversible deactivating cerebral glucose metabolism *in vivo* (§5). The cortical cooling system has been applied to study the effect of cerebral glucose metabolism on the cerebral diffusion of water and the hemodynamic response. Reversible deactivation of cerebral glucose metabolism affects the magnitude of diffusion (12-20%) but not the anisotropy (§6). Reversible deactivation of V1 decreased the hemodynamic response visually driven regions upstream and downstream from V1 (§7). Compensatory effects were observed in both hemispheres within 2 minutes of deactivation.

I see three areas of neuroscience research where the methodological and technical developments presented in this thesis could help neuroscientists; (1) study interactions between functional regions, (2) functional pathway mapping, and (3) resolving white matter architecture in neurodegenerative diseases.

8.2 Future Work

8.2.1 Reversible Deactivation fMRI Studies

The combination of reversible deactivation with fMRI has lead to two interesting results; (1) compensatory mechanisms are present in the brain within minutes of deactivation of V1, and (2) the metabolic deactivation profile in V1 correlates positively and negatively with non-visually driven structures in the brain. The sensitivity of reversible deactivation fMRI studies could greatly be improved with custom phased array coils to accommodate the presence of the cooling well. It would also be interesting to apply fluorodeoxyglucose positron emission

tomography (FDG PET) to confirm changes in metabolic activity during reversible deactivation of V1 [103-106]. Perfusion MRI studies could also be performed to measure the physiological response to deactivation[107].

8.2.2 Functional Pathway Mapping

A powerful application of combining diffusion MRI with fMRI is functional pathway mapping. Using a combination of diffusion MRI and fMRI activation, the optimal path between functional nodes can be calculated using diffusion tractography[108-110].

8.2.3 Resolving White Matter Architecture in Neurodegenerative Diseases

A number of neurodegenerative diseases affect the architecture of cerebral white matter[52,53]. However, due to the limitations of diffusion MRI methods that make underlying assumptions of the type of diffusion (i.e. DTI) and the sampling inefficiency of model-free diffusion methods (i.e. QSI, QBI), it has been difficult to accurately quantify the changes in white matter architecture during pathology. The MWF method for resolving white matter architecture presented in this thesis along with advances in phased array coil technology make it more practical to measure the complex motion of water in cerebral tissue and extract information on the underlying architecture. It may be possible to quantify the architecture of white matter at the gray matter/white matter boundary to infer diseased cortex.

References

1. Ekstrom L, Bonmasser G, Tootell RB, Roelfsema P, Vanduffel W. Investigating FEF microstimulation and distractor effects in visual cortex with awake monkey fMRI. In: Proceedings of the Society for Neuroscience: Wednesday, pg. 3. 2006; Atlanta, GA.

2. Khachaturian M. Solutions to Various Problems in Reversible Cooling fMRI Studies. Cambridge: MIT; 2003.

3. Sasaki Y, Rajimehr R, Kim BW, Ekstrom LB, Vanduffel W, Tootell RB. The radial bias: a different slant on visual orientation sensitivity in human and nonhuman primates. Neuron 2006;51(5):661-670.

4. Vanduffel W, Fize D, Mandeville JB, et al. Visual motion processing investigated using contrast agent-enhanced fMRI in awake behaving monkeys. Neuron 2001;32(4):565-577.

5. Tsao DY, Vanduffel W, Sasaki Y, et al. Stereopsis activates V3A and caudal intraparietal areas in macaques and humans. Neuron 2003;39(3):555-568.

6. Tuch D, Wisco J, Khachaturian M, Ekstrom L, Kotter R, Vanduffel W. Q-ball imaging of macaque white matter architecture. Philos Trans R Soc Lond B Biol Sci May 29th, 2005;360(1457):869-879.

7. Hayes CE, Hattes N, Roemer PB. Volume imaging with MR phased arrays. Magn Reson Med 1991;18(2):309-319.

8. Wright SM, Wald LL. Theory and application of array coils in MR spectroscopy. NMR Biomed 1997;10(8):394-410.

9. Pruessmann KP, Weiger M, Scheidegger MB, Boesiger P. SENSE: sensitivity encoding for fast MRI. Magn Reson Med 1999;42(5):952-962.

10. Sodickson DK, Griswold MA, Jakob PM. SMASH imaging. Magn Reson Imaging Clin N Am 1999;7(2):237-254, vii-viii.

11. Wiggins GC, Triantafyllou C, Potthast A, Reykowski A, Nittka M, Wald LL. 32-channel 3 Tesla receive-only phased-array head coil with soccer-ball element geometry. Magn Reson Med 2006;56(1):216-223.

12. Tootell RB, Tsao D, Vanduffel W. Neuroimaging weighs in: humans meet macaques in "primate" visual cortex. J Neurosci 2003;23(10):3981-3989.

13. Hardy CJ, Edelstein WA, Mueller OM. Surface-coil T1 images. Magn Reson Med 1986;3(6):935-940.

14. Roemer PB, Edelstein WA, Hayes CE, Souza SP, Mueller OM. The NMR phased array. Magn Reson Med 1990;16(2):192-225.

15. Griswold MA, Jakob PM, Heidemann RM, et al. Generalized autocalibrating partially parallel acquisitions (GRAPPA). Magn Reson Med 2002;47(6):1202-1210.

16. Reese TG, Heid O, Weisskoff RM, Wedeen VJ. Reduction of eddy-current-induced distortion in diffusion MRI using a twice-refocused spin echo. Magn Reson Med 2003;49(1):177-182.

17. Jones DK, Horsfield MA, Simmons A. Optimal strategies for measuring diffusion in anisotropic systems by magnetic resonance imaging. Magn Reson Med 1999;42(3):515-525.

18. Basser PJ, Mattiello J, LeBihan D. MR diffusion tensor spectroscopy and imaging. Biophys J 1994;66(1):259-267.

19. Mugler JP, 3rd, Brookeman JR. Three-dimensional magnetization-prepared rapid gradient-echo imaging (3D MP RAGE). Magn Reson Med 1990;15(1):152-157.

20. Kolster H, Mandeville JB, Vanduffel W, Wald LL. Methodology for Sub-Millimeter Resolution fMRI in Awake Monkeys at 7T. In: Proceedings of the 15th Annual Meeting of ISMRM, pg. 26. 2007; Berlin, Germany.

21. Callaghan P. Principles of nuclear magnetic resonance microscopy. Oxford: Oxford Press; 1993.

22. Cory DG, Garroway AN. Measurement of translational displacement probabilities by NMR: an indicator of compartmentation. Magn Reson Med 1990;14(3):435-444.

23. Frank L. Anisotropy in high angular resolution diffusion-weighted MRI. Magn Reson Med 2001;45(6):935-939.

24. Tuch DS. Q-ball imaging. Magn Reson Med 2004;52(6):1358-1372.

25. Tuch DS, Reese TG, Wiegell MR, Wedeen VJ. Diffusion MRI of complex neural architecture. Neuron 2003;40(5):885-895.

26. Parker GJ, Alexander DC. Probabilistic Monte Carlo based mapping of cerebral connections utilising whole-brain crossing fibre information. Inf Process Med Imaging 2003;18:684-695.

27. Tuch DS, Reese TG, Wiegell MR, Makris N, Belliveau JW, Wedeen VJ. High angular resolution diffusion imaging reveals intravoxel white matter fiber heterogeneity. Magn Reson Med 2002;48(4):577-582.

28. Liu C, Bammer R, Acar B, Moseley ME. Characterizing non-Gaussian diffusion by using generalized diffusion tensors. Magn Reson Med 2004;51(5):924-937.

29. Ozarslan E, Mareci TH. Generalized diffusion tensor imaging and analytical relationships between diffusion tensor imaging and high angular resolution diffusion imaging. Magn Reson Med 2003;50(5):955-965.

30. Tournier JD, Calamante F, Gadian DG, Connelly A. Direct estimation of the fiber orientation density function from diffusion-weighted MRI data using spherical deconvolution. Neuroimage 2004;23(3):1176-1185.

31. Assaf Y, Basser PJ. Composite hindered and restricted model of diffusion (CHARMED) MR imaging of the human brain. Neuroimage 2005;27(1):48-58.

32. Jansons KM, Alexander DC. Persistent angular structure: new insights from diffusion magnetic resonance imaging data. Inverse Problems 2003;19:1031-1046.

33. Tuch DS. Diffusion MRI of Complex Tissue Structure. Cambridge: Harvard-MIT; 2002.

34. Frank L. Characterization of anisotropy in high angular resolution diffusion-weighted MRI. Mag Res Med 2002;47(6):1083-1099.

35. Beaulieu C. The basis of anisotropic water diffusion in the nervous system - a technical review. NMR Biomed 2002;15(7-8):435-455.

36. Khachaturian MH, Wisco JJ, Tuch DS. Boosting the sampling efficiency of q-Ball imaging using multiple wavevector fusion. Magn Reson Med 2007;57(2):289-296.

37. Tuch DS, Wisco JJ, Khachaturian MH, Ekstrom LB, Kotter R, W V. Q-ball imaging of macaque white matter architecture. Philos Trans R Soc Lond B Biol Sci May 29th, 2005;360(1457):869-879.

38. Perrin M, Poupon C, Rieul B, et al. Validation of q-ball imaging with a diffusion fibre-crossing phantom on a clinical scanner. Philos Trans R Soc Lond B Biol Sci 2005;360(1457):881-891.

39. Campbell JS, Siddiqi K, Rymar VV, Sadikot AF, Pike GB. Flow-based fiber tracking with diffusion tensor and q-ball data: Validation and comparison to principal diffusion direction techniques. Neuroimage 2005.

40. Burt P, Adelson E. The Laplacian Pyramid as a Compact Image Code. IEEE Trans on Communications 1983:532-540.

41. Li H, Manjunath B, Mitra S. Multisensor image fusion using the wavelet transform. Graphical Models and Image Processing 1995;57: 235-245.

42. Bülow T, Daniilidis K. Surface representations using spherical harmonics and gabor wavelets on the sphere. Technical Report MS-CIS-01-37: Dept. of Computer and Information Science, University of Pennslyvania; 2001.

43. Demanet L, Vandergheynst P. Gabor wavelets on the sphere. Proc SPIE Annual conference. San Diego, CA; 2003.

44. Hansen FK, Banday AJ, Gorski KM. Testing the cosmological principle of isotropy: local power-spectrum estimates of the WMAP data. Monthly Notices of the Royal Astronomical Society 2004;354(3):641-665.

45. Kullback S, Leibler RA. On information and sufficiency. Annals of Mathematical Statistics 1951;22(1):79-86.

46. Clark CA, Hedehus M, Moseley ME. Diffusion time dependence of the apparent diffusion tensor in healthy human brain and white matter disease. Magn Reson Med 2001;45(6):1126-1129.

47. Lomber SG, Payne BR, Horel JA. The cryoloop: an adaptable reversible cooling deactivation method for behavioral or electrophysiological assessment of neural function. J Neurosci Methods 1999;86(2):179-194.

48. Lomber SG. Virtual Lesions. Oxford: Oxford Press; 2002.

49. Lomber SG, Payne BR. Translaminar differentiation of visually guided behaviors revealed by restricted cerebral cooling deactivation. Cereb Cortex 2000;10(11):1066-1077.

50. Vanduffel W, Orban GA, Lomber SG, Payne BR. Functional impact of cerebral projection systems. Mol Psychiatry 1998;3(3):215-219.

51. Khachaturian M, Ekstrom L, Arsenault J, Tuch D, Vanduffel W. Reversible deactivation of cerebral glucose metabolism affects the diffusion MRI signal. Brain 2007;[In Review].

52. Okubo T, Aoki S, Abe O, et al. [Principles of diffusion-weighted MR imaging and application to clinical neurology]. Rinsho Shinkeigaku 2004;44(11):954-956.

53. Rosenbloom M, Sullivan EV, Pfefferbaum A. Using magnetic resonance imaging and diffusion tensor imaging to assess brain damage in alcoholics. Alcohol Res Health 2003;27(2):146-152.

54. Behrens TE, Johansen-Berg H, Woolrich MW, et al. Non-invasive mapping of connections between human thalamus and cortex using diffusion imaging. Nat Neurosci 2003;6(7):750-757.

55. Le Bihan D, Urayama S, Aso T, Hanakawa T, Fukuyama H. Direct and fast detection of neuronal activation in the human brain with diffusion MRI. Proc Natl Acad Sci U S A 2006;103(21):8263-8268.

56. Beaulieu C, Allen PS. Determinants of anisotropic water diffusion in nerves. Magn Reson Med 1994;31(4):394-400.

57. Partridge SC, Mukherjee P, Henry RG, et al. Diffusion tensor imaging: serial quantitation of white matter tract maturity in premature newborns. Neuroimage 2004;22(3):1302-1314.

58. Elshafiey I, Bilgen M, He R, Narayana PA. In vivo diffusion tensor imaging of rat spinal cord at 7 T. Magn Reson Imaging 2002;20(3):243-247.

59. Mukherjee P, Miller JH, Shimony JS, et al. Normal brain maturation during childhood: developmental trends characterized with diffusion-tensor MR imaging. Radiology 2001;221(2):349-358.

60. Pierpaoli C, Barnett A, Pajevic S, et al. Water diffusion changes in Wallerian degeneration and their dependence on white matter architecture. Neuroimage 2001;13(6 Pt 1):1174-1185.

61. Watanabe T, Honda Y, Fujii Y, Koyama M, Tanaka R. Serial evaluation of axonal function in patients with brain death by using anisotropic diffusion-weighted magnetic resonance imaging. J Neurosurg 2004;100(1):56-60.

62. De Poorter J, De Wagter C, De Deene Y, Thomsen C, Stahlberg F, Achten E. Noninvasive MRI thermometry with the proton resonance frequency (PRF) method: in vivo results in human muscle. Magn Reson Med 1995;33(1):74-81.

63. MacFall JR, Prescott DM, Charles HC, Samulski TV. 1H MRI phase thermometry in vivo in canine brain, muscle, and tumor tissue. Med Phys 1996;23(10):1775-1782.

64. Lomber SG. The advantages and limitations of permanent or reversible deactivation techniques in the assessment of neural function. J Neurosci Methods 1999;86(2):109-117.

65. Hong X. Measuring diffusion in inhomogeneous systems in imaging mode using antisymmetric sensitizing gradients. J Magn Reson A 1992;99:561-570.

66. Lian J. Magnetic resonance imaging of diffusion in the presence of background gradients and imaging of background gradients. J Magn Reson 1994;106:65-74.

67. Sotak CH. Nuclear magnetic resonance (NMR) measurement of the apparent diffusion coefficient (ADC) of tissue water and its relationship to cell volume changes in pathological states. Neurochem Int 2004;45(4):569-582.

68. Beaulieu C, Allen PS. Water diffusion in the giant axon of the squid: implications for diffusion-weighted MRI of the nervous system. Magn Reson Med 1994;32(5):579-583.

69. Beaulieu C, Allen PS. An in vitro evaluation of the effects of local magnetic-susceptibility-induced gradients on anisotropic water diffusion in nerve. Magn Reson Med 1996;36(1):39-44.

70. Trudeau JD, Dixon WT, Hawkins J. The effect of inhomogeneous sample susceptibility on measured diffusion anisotropy using NMR imaging. J Magn Reson B 1995;108(1):22-30.

71. Mascalchi M, Filippi M, Floris R, Fonda C, Gasparotti R, Villari N. Diffusion-weighted MR of the brain: methodology and clinical application. Radiol Med (Torino) 2005;109(3):155-197.

72. Wanka F, Van Zoelen EJ. Cellular organelle transport and positioning by plasma streaming. Cell Mol Biol Lett 2003;8(4):1035-1045.

73. Nichols TE, Holmes AP. Nonparametric permutation tests for functional neuroimaging: a primer with examples. Hum Brain Mapp 2002;15(1):1-25.

74. Thelwall PE, Shepherd TM, Stanisz GJ, Blackband SJ. Effects of temperature and aldehyde fixation on tissue water diffusion properties, studied in an erythrocyte ghost tissue model. Magn Reson Med 2006;56(2):282-289.

75. Vanduffel W, Payne BR, Lomber SG, Orban GA. Functional impact of cerebral connections. Proc Natl Acad Sci U S A 1997;94(14):7617-7620.

76. Sokoloff L. The deoxyglucose method for the measurement of local glucose utilization and the mapping of local functional activity in the central nervous system. Int Rev Neurobiol 1981;22:287-333.

77. Sokoloff L, Reivich M, Kennedy C, et al. The [14C]deoxyglucose method for the measurement of local cerebral glucose utilization: theory, procedure, and normal values in the conscious and anesthetized albino rat. J Neurochem 1977;28(5):897-916.

78. Hammerschlag R, Brady S. Axonal Transport and the neuronal cytoskeleton. In: Siegel G, Agranoff B, Albers W, Molinoff P, eds. Basic Neurochemistry. New York: Raven Press, 1989; 457-478.

79. Ochs S. Trophic functions of the neuron. 3. Mechanisms of neurotrophic interactions. Systems of material transport in nerve fibers (axoplasmic transport) related to nerve function and trophic control. Ann N Y Acad Sci 1974;228(0):202-223.

80. Ochs S. Local supply of energy to the fast axoplasmic transport mechanism. Proc Natl Acad Sci U S A 1971;68(6):1279-1282.

81. Ochs S. Fast transport of materials in mammalian nerve fibers. Science 1972;176(32):252-260.

82. Ochs S, Sabri MI, Johnson J. Fast transport system of materials in mammalian nerve fibers. Science 1969;163(868):686-687.

83. Smith RS, Snyder RE. Anterograde to retrograde reversal of fast axonal transport within cold blocked and rewarmed intact axons. Brain Res 1995;672(1-2):205-213.

84. Brimijoin S. Stop-flow: a new technique for measuring axonal transport, and its application to the transport of dopamine-beta-hydroxylase. J Neurobiol 1975;6(4):379-394.

85. Oaklander AL, Spencer PS. Cold blockade of axonal transport activates premitotic activity of Schwann cells and wallerian degeneration. J Neurochem 1988;50(2):490-496.

86. Koike H. The disturbance of the fast axonal transport of protein by passive stretching of an axon in Aplysia. J Physiol 1987;390:489-500.

87. Koike H, Matsumoto H. Fast axonal transport of membrane protein and intra-axonal diffusion of free leucine in a neuron of Aplysia. Neurosci Res 1985;2(4):281-285.

88. Nelissen K, Vanduffel W, Orban GA. Charting the lower superior temporal region, a new motion-sensitive region in monkey superior temporal sulcus. J Neurosci 2006;26(22):5929-5947.

89. Galuske RA, Schmidt KE, Goebel R, Lomber SG, Payne BR. The role of feedback in shaping neural representations in cat visual cortex. Proc Natl Acad Sci U S A 2002;99(26):17083-17088.

90. Malpeli JG. Reversible inactivation of subcortical sites by drug injection. J Neurosci Methods 1999;86(2):119-128.

91. Malpeli JG, Schiller PH. A method of reversible inactivation of small regions of brain tissue. J Neurosci Methods 1979;1(2):143-151.

92. Malpeli JG, Schiller PH, Colby CL. Response properties of single cells in monkey striate cortex during reversible inactivation of individual lateral geniculate laminae. J Neurophysiol 1981;46(5):1102-1119.

93. Hupe JM, Chouvet G, Bullier J. Spatial and temporal parameters of cortical inactivation by GABA. J Neurosci Methods 1999;86(2):129-143.

94. Bandettini PA, Wong EC, Hinks RS, Tikofsky RS, Hyde JS. Time course EPI of human brain function during task activation. Magn Reson Med 1992;25(2):390-397.

95. Kwong KK, Belliveau JW, Chesler DA, et al. Dynamic magnetic resonance imaging of human brain activity during primary sensory stimulation. Proc Natl Acad Sci U S A 1992;89(12):5675-5679.

96. Ogawa S, Tank DW, Menon R, et al. Intrinsic signal changes accompanying sensory stimulation: functional brain mapping with magnetic resonance imaging. Proc Natl Acad Sci U S A 1992;89(13):5951-5955.

97. Fox PT, Raichle ME. Stimulus rate dependence of regional cerebral blood flow in human striate cortex, demonstrated by positron emission tomography. J Neurophysiol 1984;51(5):1109-1120.

98. Plum F, Posner JB, Troy B. Cerebral metabolic and circulatory responses to induced convulsions in animals. Arch Neurol 1968;18(1):1-13.

99. Posner JB, Plum F, Van Poznak A. Cerebral metabolism during electrically induced seizures in man. Arch Neurol 1969;20(4):388-395.

100. Roy CS, Sherrington CS. On the Regulation of the Blood-supply of the Brain. J Physiol 1890;11(1-2):85-158 117.

101. Logothetis NK, Pauls J, Augath M, Trinath T, Oeltermann A. Neurophysiological investigation of the basis of the fMRI signal. Nature 2001;412(6843):150-157.

102. Logothetis NK, Wandell BA. Interpreting the BOLD signal. Annu Rev Physiol 2004;66:735-769.

103. Wernick M, Aarsvold J. Emission Tomography: The Fundamentals of PET and SPECT. San Diego, CA: Elsevier; 2004.

104. Aydin A, Hickeson M, Yu JQ, Zhuang H, Alavi A. Demonstration of excessive metabolic activity of thoracic and abdominal muscles on FDG-PET in patients with chronic obstructive pulmonary disease. Clin Nucl Med 2005;30(3):159-164.

105. Jeong Y, Cho SS, Park JM, et al. 18F-FDG PET findings in frontotemporal dementia: an SPM analysis of 29 patients. J Nucl Med 2005;46(2):233-239.

106. Oquendo MA, Krunic A, Parsey RV, et al. Positron Emission Tomography of Regional Brain Metabolic Responses to a Serotonergic Challenge in Major Depressive Disorder with and without Borderline Personality Disorder. Neuropsychopharmacology 2005.

107. Rosen BR, Belliveau JW, Chien D. Perfusion imaging by nuclear magnetic resonance. Magn Reson Q 1989;5(4):263-281.

108. Gerig G, Gouttard S, Corouge I. Analysis of brain white matter via fiber tract modeling. Conf Proc IEEE Eng Med Biol Soc 2004;6:4421-4424.

109. Price G, Cercignani M, Parker GJ, et al. Abnormal brain connectivity in first-episode psychosis: a diffusion MRI tractography study of the corpus callosum. Neuroimage 2007;35(2):458-466.

110. Yamamoto A, Miki Y, Urayama S, et al. Diffusion tensor fiber tractography of the optic radiation: analysis with 6-, 12-, 40-, and 81-directional motion-probing gradients, a preliminary study. AJNR Am J Neuroradiol 2007;28(1):92-96.

Appendix

A. Notation

Multiple definitions are separated by a slash.

α	thermal coefficient (0.01 ppm/°C) / angular distance between points on a sphere
b, *b*	b-value
°C	degrees Celsius
D	diffusion tensor
δ	pulse gradient duration
$E(\mathbf{q},\tau)$	diffusion MRI signal as function of wavevector, **q**, and time, τ
f_i	volume fraction between diffusion compartments
$\Delta\phi$	change in phase
$\Delta\phi_{drift}$	change in phase drift
g	pulsed gradient direction
G	spherical Gabor basis matrix
$G(\alpha,k)$	spherical Gabor wavelets
g_{max}	maximum gradient value
γ	gyromagnetic ratio
k	frequency of complex exponential in Gabor wavelets
$KL(\psi_R, \psi)$	Kullback-Leibler divergence between a reference ODF and a measured ODF
maxmod	choose-max selection rule
p	p-value
$\bar{P}_s(\mathbf{R},\tau)$	average self propagator, the prob. a particle travels **R** in a time τ
q	diffusion wavevector
Q_i	quality factor of resonance circuit
λ_i	i^{th} eigenvalue of the diffusion tensor, **D**, i = {1, 2, 3}
$\psi(\mathbf{u}), \psi(\theta,\varphi)$	ODF as a function of the unit vector, **u**, or the polar and azimuthal angles, θ,φ
R	relative spin displacement

$\mathbf{r}$	relative spin diffusion vector
Δr	q-space resolution according the Rayleigh criterion
S	magnitude of MRI signal
σ	standard deviation / width of Gaussian smoothing kernel
$\mathbf{\Sigma}$	noise correlation matrix
T_C	temperature of the voxel immediately under the cryoprobe
TE	echo time
ΔT	change in temperature
τ	diffusion time
$\mathbf{w}_l$	low wavevector basis coefficients
$\mathbf{w}_h$	high wavevector basis coefficients
ψ_h	high wavevector ODF
ψ_l	low wavevector ODF
ψ_R	reference ODF
$\mathbf{u}$	unit vector
Z	normalization constant
$\oplus$	fusion selection rule

B. Acronyms

ADC	apparent diffusion coefficient
ANOVA	analysis of variance
BOLD	blood oxygen level defect
cROI	control region of interest
CSF	cerebral spinal fluid
DSI	diffusion spectrum imaging
EPI	echo-planar imaging
FA	fractional anisotropy
FDG PET	fluorodeoxyglucose positron emission tomography
fMRI	functional magnetic resonance imaging
FOV	field-of-view

FRT	Funk-Radon Transform
GLM	general linear model
GM	gray matter
GRAPPA	generalized auto-calibrating partially parallel acquisitions
HARDI	high angular resolution diffusion imaging
IPCM	intra-voxel peak consistency metric
MION	microcrystalline iron oxide nanoparticles
MR	magnetic resonance
MRI	magnetic resonance imaging
MWF	multi-wavevector fusion
NMR	nuclear magnetic resonance
NPPT	nonparametric permutation testing
ODF	orientation distribution function
PDF	probability density function
PRFST	proton resonance frequency shift thermometry
QBI	Q-ball imaging
QSI	Q-space imaging
RD	reversible deactivation
RF	radio-frequency
ROI	region of interest
SEM	standard error metric
SNR	signal-to-noise ratio
SPM	statistical parametric maps
TE	excitation time
TR	relaxation time
WM	white matter